FLORIDA STATE UNIVERSITY

COLLEGE OF ARTS AND SCIENCES

CONTRIBUTION OF WIND AND LOOP CURRENT EDDIES

TO THE CIRCULATION IN THE WESTERN GULF OF MEXICO

By

ERICK RAUL OLVERA-PRADO

A Dissertation submitted to the
Department of Earth, Ocean, and Atmospheric Science
in partial fulfillment of the
requirements for the degree of
Doctor of Philosophy

2018

Erick Raul Olvera-Prado defended this dissertation on December 17, 2018.
The members of the supervisory committee were:

Eric Chassignet
Professor Directing Dissertation

Gordon Erlebacher
University Representative

William Dewar
Committee Member

Steven Morey
Committee Member

Mike Stukel
Committee Member

The Graduate School has verified and approved the above-named committee members, and certifies that the dissertation has been approved in accordance with university requirements.

A Lulu y Diego

ACKNOWLEDGMENTS

TABLE OF CONTENTS

LIST OF TABLES

LIST OF FIGURES

x

LIST OF ABBREVIATIONS

BOC   Bay of Campeche
CFSR   Climate Forecast System Reanalysis
CW   Central Western
CONACYT   Consejo Nacional de Ciencia y Tecnología
GOM   Gulf of Mexico
HYCOM   Hybrid Coordinate Ocean Model
IQR   Interquartile range
LC   Loop Curent
LCE   Loop Current Eddy
NRL   Naval Research Laboratory
NW   North Western
ONR   Office of Naval Research
SAG   Sigsbee Abysssal Gyre
SEP   Secretaría de Educación Pública
SSH   Sea Surface Height
SST   Sea Surface Temperature
SW   South Western

ABSTRACT

The role of the Loop Current (LC) and their associated eddies in driving the circulation of the Gulf of Mexico (GoM) has been investigated throughout several decades from different perspectives. The practical benefits of a better understanding of the mechanisms responsible for the circulation in the GoM are many, from ocean prediction to fisheries management. In the present study, the role of the wind and the Loop Current Eddies (LCEs) in sustaining the less well known western GoM circulation is investigated by isolating the various types of external forcing in a set of numerical experiments of increasing complexity using the HYbrid Coordinate Ocean Model (HYCOM). First, we examine the impact of the wind and open boundary conditions on LCE shedding seasonality and separation period. We then discuss the different factors that contribute to the wind-driven circulation in the western GoM. Finally, the relative importance of the wind, LCEs and another processes in sustaining the western GoM circulation is analyzed with a vorticity budget approach. It was found that the overall effect of the wind forcing increases the shedding of eddies, thereby reducing the mean LCE separation period by 20%, but tends to delay the shedding in certain months altering their "seasonality". Also, the circulation shows that the response of the flow in the Bay of Campeche (BOC) to the wind is mainly barotropic, while the eddy-induced circulation response is partially baroclinic. The vorticity balance performed in the western basin shows that planetary vorticity and stretching of the water column are primarily responsible for the balance in time scales longer than weeks, and their variability are good indicators of LCEs entering the central and northwestern regions. However the southwestern region is primarily driven by stretching. Also, our results show that mean advection of vorticity and planetary vorticity are responsible for the time-averaged vorticity field. Input of vorticity through wind stress is negligible in the regional vorticity balance.

CHAPTER 1

INTRODUCTION

The Loop Current (LC) and associated eddies are the dominant components of the circulation in the eastern Gulf of Mexico (GoM) and have been studied for nearly five decades now. These powerful oceanic features affect almost every aspect of the oceanography in the GoM, directly and indirectly, through a wide range of space and time scales. Having a better understanding of their complexity will serve as a basis for solving a host of practical problems like: ocean prediction, antisubmarine warfare and surveillance, tactical planning, design and operation of offshore platforms, deep water drilling rigs planning, optimum track ship routing, search and rescue, fisheries management, and so forth (Chassignet et al., 2005). In this study, we will investigate the relative importance of the wind and of the LC eddies (LCEs) in driving the circulation of the western Gulf of Mexico.

The Gulf of Mexico is a semi-enclosed sea located in the western Atlantic Ocean, it connects with the Caribbean Sea through the Yucatan Channel (YC) and with the North Atlantic Ocean through the Florida Straits. The circulation in the basin is forced at the surface by the wind stress (and to a lessen degree by heat and freshwater fluxes), and flow through the Yucatan Channel. The YC flow is driven by the western boundary current of the North Atlantic Subtropical Gyre, an anticyclonic circulation forced by the northward compensation of the Sverdrup transport due to the wind stress curl, and the surface component of the meridional overturning cell (MOC) (Schmitz and McCartney, 1993) yielding a mean transport of 27.0 +/- 0.5 Sv (Athie et al., 2015).

The Yucatan Current enters the GoM through the YC and forms an anticyclonic-looping circulation: the Loop Current (LC), which, in its extended phase, intrudes further North and episodically sheds large warm-core anticyclonic vortices called Loop Current Eddies (LCEs) with a time interval between separation events (referred to as LCE separation period) observed to range from a few weeks to 18-19 months (Sturges and Leben, 2000; Leben, 2005; Vukovich 2012). LCEs have diameters of about 300 km or more (Vukovich, 2012), an average westward propagation speed of 4.4 +/- 2.9 km/day (Leben, 2005; Vukovich, 2007) and lifetimes of months to approximately a

1

year (Elliot, 1982; Frolov, 2004). The LC exits the basin through the Florida Straits becoming the Florida Current and then the Gulf Stream.

1.1 Background

1.1.1 Mean circulation in the GoM

Dynamically, the western region of the Gulf can be divided in two subregions with different behavior: the northwestern region is dominated by an anticyclonic circulation and the presence of mesoscale eddies (LCEs) (Vidal et al., 1994) and the Bay of Campeche (BOC) on the southwest, characterized by a cyclonic circulation (Vazquez de la Cerda, 2005, Perez-Brunius et al., 2013). On the east, a large anticyclonic-looping circulation from $\sim 21^{o}$N to 27°N is depicted in the center and northeast of the Gulf (Fig. 1.1).

The mean circulation in the GoM has been studied by different authors with different approaches. Maul and Herman (1985), using a hydrographic data bank of STD (Salinity, Temperature and Depth), CTD (Conductivity, Temperature and Depth) and XBT (Bathythermographs), with information collected between 1969 and 1973, built a mean dynamic topography of the Gulf. They found that the mean topography is characterized by the LC in the east and a cyclone-anticyclone pair in the west. Unfortunately, most of the data are concentrated in the east of the Gulf and during the summer so their results for the west of the Gulf can not be considered conclusive. Evidence has been continuously provided for the existence of a semi-permanent cyclonic circulation in the BOC (Merrell and Morrison, 1981). Vazquez de la Cerda et al. (2005) presented strong evidence of a mean cyclonic gyre in the BOC likely forced by the positive wind stress curl that prevails in this region throughout the year (Blaha and Sturges, 1981), using oceanographic observations available at the time. However, some studies suggest that the LCEs collapsing against the western boundary influence the cyclonic circulation in the BOC. Vidal et al. (1992) concluded that the collision of a LCE with the southwestern continental shelf led to a transfer of mass and angular momentum to the south, thereby producing a cyclonic eddy in the BOC. Also, Romanou et al. (2004) mention that the generation of cyclonic eddies in the western BOC is correlated with the arrival of LCEs. In 2013, Perez-Brunius et al., using direct observations of surface drifters, current meter moorings and satellite altimetry provided further evidence that the cyclonic gyre is a vertically coherent and nearly unidirectional flow extending below 1000 m, and confined to the deep western basin. The
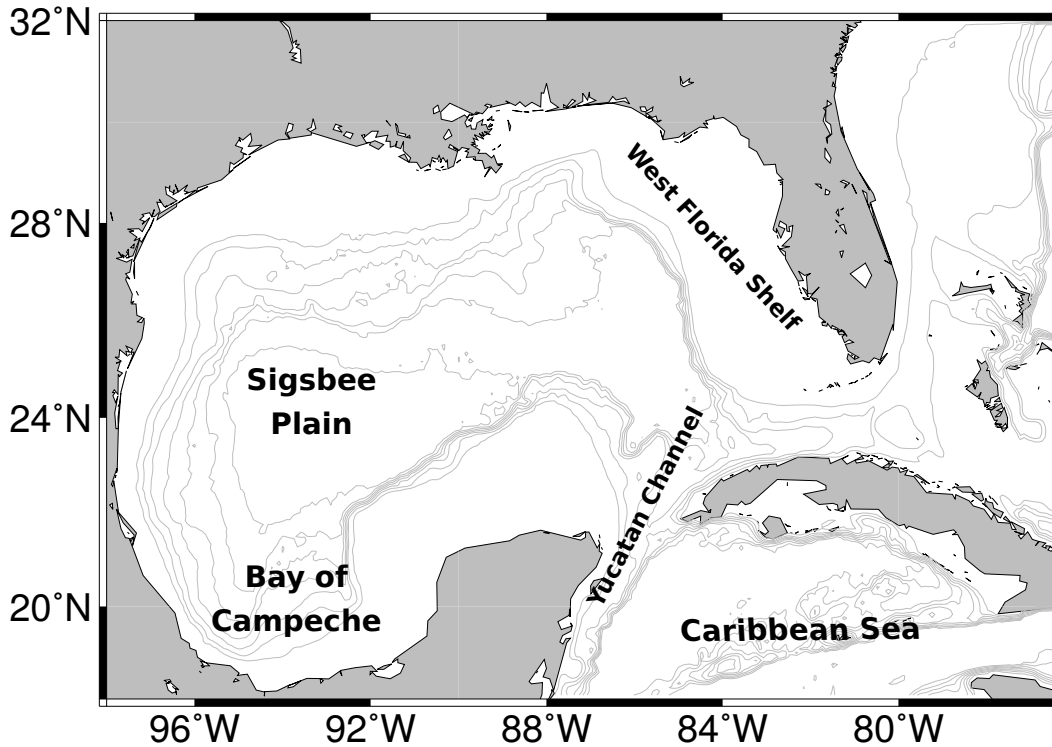
Figure 1.1: Gulf of Mexico domain and bathymetry covered by the ocean model, the location of the Bay of Campeche and the Yucatan Channel, among others, is also indicated. Isobaths are shown as grey contours from [500:500:3500] m.

authors concluded that the cyclonic gyre results from the contributions of wind stress curl and the conservation of potential vorticity in an equivalent barotropic flow, but suggest the need of an in-depth analysis to determine the role the winds play in the seasonal modulation of the cyclonic circulation. Their data also suggests that the intraseasonal variability of the surface currents are mainly due to changes in the position, size and intensity of the cyclonic gyre, which in turn are produced by the influence of energetic LCEs traveling to the south region of the Gulf and then impacting on the western boundary.

1.1.2 Role of the LC in driving the GoM circulation

The LC is recognized to be the dominant mechanism in driving the circulation in the eastern GOM. Hurlburt and Thompson (1980) conducted a series of numerical experiments to test whether the eddy-shedding was controlled by internal dynamics or external changes in boundary conditions

(BC) and were the first to find that a prescribed steady transport at the YC is able to reproduce the characteristic LC behavior and realistic features of the LCE shedding. However the LCE separation period exhibited an unrealistic quasi-annual frequency. In fact the LC cycle, and therefore the eddy shedding, is heavily variable with two primary peaks in the distribution of separation periods at 6 and 11 months (Sturges and Leben, 2000; Vukovich 2012).

The existing set of altimetric measurements of the LCEs (~ 20 years) is not long enough to make statistically significant conclusions about the behavior of the LC. This was firstly noted in 2005, when Schmitz et al. reconsidered the need to have a long observational record of eddy shedding to provide more adequate statistics, and promoted the realization of numerical studies of comparatively long duration changing model parameters like resolution and boundary conditions. A decade later, Dukhovskoy et al. (2015) analyzed the uncertainty of LC statistics derived from SSH observations using a multidecadal regional simulation configured for the GoM. They discussed that the LC state can be described in terms of well-defined metrics that are used to quantify the statistical characteristics of the LC and LCEs and provided a new insight into the behaviour of the LC system in the GoM at longer time scales than previously studied.

The LCEs are well-known to be the main source of heat, momentum, and salinity in the western GoM (Elliot, 1982) and to have a characteristic west-southwest trajectory, result of the combined effects of the β effect (defined as the effect on the fluid motion by the variation of the Coriolis parameter with latitude, Cushman-Roisin et al., 1990) and a southward component induced by a self-advective tendency associated with nonlinear effects over flat topography, such as the abyssal GoM plain (Smith and O'Brien, 1983). Despite this general tendency for west-southwest propagation, LCEs frequently interact nonlinearly with the energetic eddy field in the western GoM and arrive at the western continental margin along disparate paths (Hamilton et al., 1999; Vukovich, 2007). A recent characterization of LCEs paths made by Vukovich (2007), initially attempted using satellite imagery (Vukovich and Crissman, 1986), identified three paths: a northern path, a central path and a southern path, all three of them leading to a region in the western GoM informally referred to as the "Eddy graveyard" (Biggs et al., 1996). In another study of LCE propagation, Hamilton et al. (1999) concluded that there are no preferred eddy pathways through the deep basin. This result is based on the paths of eddy center positions determined using a kinematic analysis of the trajectories of satellite-tracked drifters orbiting within 10 LCEs. Systematic tracking of LCEs

throughout their lifespan from separation to dissipation was conducted by Donohue et al. (2008), using continuous sampling provided from satellite altimeters and gave the first comprehensive and detailed look at the lifespan and ultimate fate of LCEs in the western Gulf. They computed statistics from a set of 17 LCE separation events from the altimetric record: January 1993 through June 2006, and found a mean lifespan of 234 days (about 9.5 months), with LCEs dissipating throughout the western GoM west of 91^oW, usually with centers in ocean depths greater than 2000 m.

1.1.3   Wind-driven vs LC-driven circulation in the GoM

Comparatively, studies on the relative contribution of the wind and of the LC-induced circulation in the GoM are scarce. Early studies suggested that the winds (Fig. 1.2) and basin geometry of the GoM seemed suitable for the development of a Western Boundary Current (WBC) that was the result of the combined effects of LCEs and large-scale wind stress curl (Fig. 1.2) forcing (Sturges and Blaha, 1976), although the relative importance of such forcings was not fully understood. Fundamental work by Elliot (1982) of LC versus wind energy sources indicate that although the energy contribution of the wind stress and LC rings is about the same (2.8 x$10^4 Jm^{-2}$ and 5.1 x$10^4 Jm^{-2}$, respectively), the wind stress energy is a basin-wide value, whereas the ring's available potential energy (APE) is concentrated into a smaller length scale consistent with the north-south scale of the WBC. Contrary to Elliot's (1982) deductions, Sturges (1993) examined their relative contribution by focusing on the annual cycle of the estimated flow as deduced from a compilation of ship's drift data and concluded that the WBC is driven by the annual variation in wind stress curl augmented by Ekman Pumping, with the current's flow along the WBC strongest in July and weakest in October. He also found evidence that LCEs shed from the Loop Current with no annual periodicity so they make no significant contribution to the long-term annual signal. However he identified two effects that could lead to annual perturbation: when eddies drift across the western Gulf, they are acted upon both by wind and winter cooling. Vidal (1999), through an analysis of the geostrophic circulation in the western Gulf observed during summer in 1985, found that the WBC is formed by conservation of angular momentum produced by the collision of LCEs against the western Gulf boundary and concluded that when very strong local forcing such as the presence of a LCE, the wind-driven background circulation is overwhelmed by such eddy forcing. Lee and Mellor (2003) noted that, in addition to wind forcing, their results show that their

model-determined anticyclonic upper level circulation in the western Gulf is strongly influenced by the average contribution of LCEs propagating to the west while dispersing anticyclonic vorticity.

The general consensus in the 2000's was that seasonal flow in the western GoM is wind forced, but a detailed quantitative determination of the partitioning between the wind and eddy contributions to the mean flow was needed (Schmitz et al., 2005).

Sturges (1993) examined the question as to whether the monthly distribution of LCE separations could reliably be distinguished from random or uniform, and concluded that it could not, on the basis of the database in hand at that time. It was in the late 2000's when the seasonal preference in the timing of the LCE separation for Spring and Fall became more apparent due to the longer records of altimetric monitoring of the LC and LCEs (Chang and Oey, 2012; Vukovich, 2012; Garcia-Jove, 2016; Hall and Leben, 2016). However, some authors claim that the existing set of altimetric measurements (1993-present) could not be long enough to make such a conclusion, this has motivated a preliminary reanalysis of pre-altimetric and altimetric record of LC intrusion and eddy shedding (Leben and Hall, 2010; Hall and Leben, 2016). This shedding preference for Spring and Fall suggest that the system is, at least in part, forced. Numerical studies that were performed after the observational record from altimetric LC monitoring showed evidence of seasonality focused on the bimodal character of the seasonal LCE separation histogram mentioned above (Chang and Oey, 2012, 2013a). The proposed physical mechanisms forcing the observed "biannual" seasonality of LCE separation are the biannual (twice-per-year) variation in trade winds and the corresponding wind-forced biannual changes in Yucatan transport observed in the model simulations. However, Hall and Leben (2016) claim that a bimodal distribution is not necessarily equivalent to biannual events considering that they didn't happen with sufficient regularity over the 20 years spanned by the altimetric record they analyzed, and suggested caution and investigation in more detail in future studies. This present study attempts to demonstrate that actually having a longer record of LCE shedding events improves our confidence to conclude that this distribution shows seasonality.

This collection of previous studies indicates that a detailed quantitative determination of the partitioning between the wind and eddy contributions to the flow remains at least somewhat elusive. Despite much effort in trying to quantify the mean energy input of both factors on the WBC in the GoM (Elliot, 1982; Jaimes, 2005) and to attribute its variability to annual and biannual variation of known physical mechanisms (Sturges, 1993), a gap remains about over which space and time scales

6

Annual mean wind stress (1992-2010) CFSR

(): Min= 0.00, Max= 0.07, Int= 0.00
Vector norm (Pa): Min= 0.00, Max= 0.07

Wind Stress Curl (*1e6 N/m^3), CFSR Annual mean (1992-2009), Smth

(): Min= -0.58, Max= 0.51, Int= 0.06
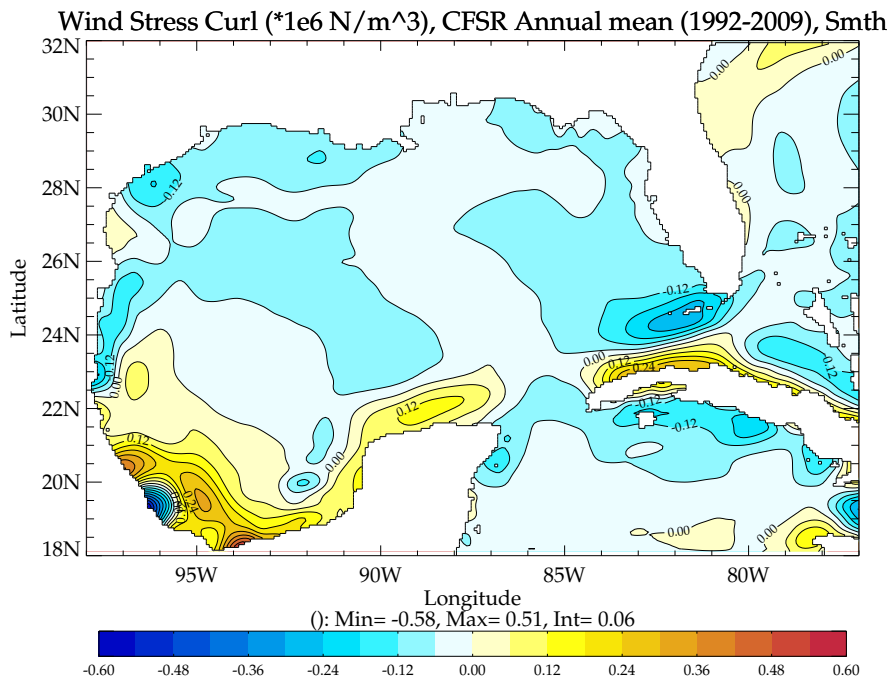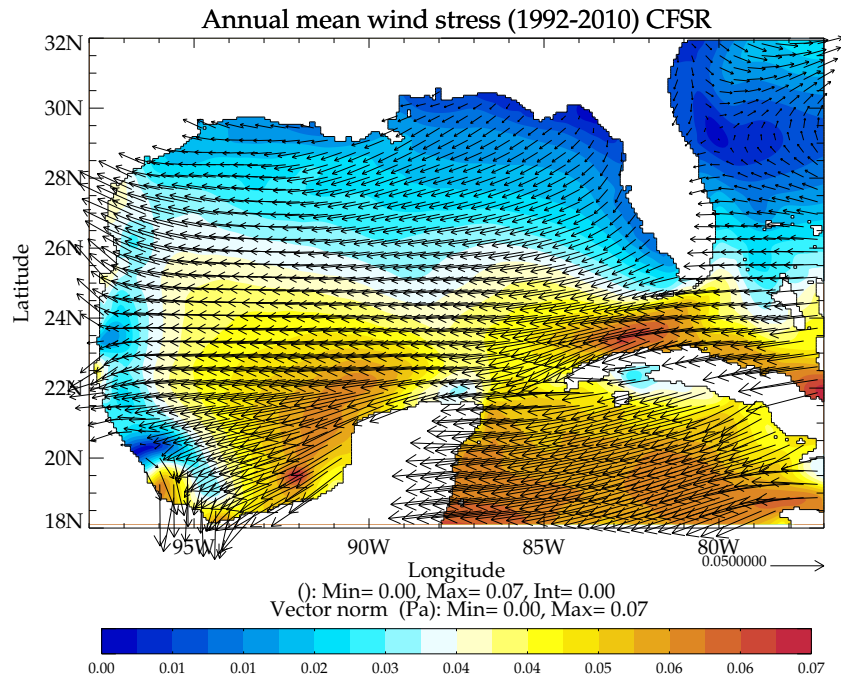
Figure 1.2: Annual mean wind stress (top) and curl (bottom).

these processes act with more or less extent as well as in which regions of the GoM a given process is relatively more important than the other. In terms of physical processes we look at different time scales from daily to seasonal and decadal variability.

1.2   Motivation and research objectives

This study focuses on addressing the following objectives:

1. Estimate the contribution of the wind and LCEs to the circulation of the western GoM at different time scales

2. Understand the physical mechanisms by which the wind and LCEs sustain the western GoM circulation

This study is part of a fundamental but bigger problem, the results are expected to contribute to the understanding of the role of wind and LCEs in driving the western GoM at longer time scales which, we believe, has not been previously reported. These results are also expected to be meaningful and of interest for the GoM research community in various disciplines.

1.3   Experimental design

Numerical simulations are important tools to study ocean processes where observational data coverage is scarce. We make use of an Ocean General Circulation Model (OGCM) to address the objective points presented above. This is accomplished by isolating the various types of external forcing in a set of multi-decadal numerical simulations. In particular, we perform a set of free-run, i.e. no data assimilation, experiments first beginning with the most realistic, complex simulation constrained with both surface and lateral forcings, this simulation is then compared to observations and is intended to provide the base results that lead to the achievement of our main scientific questions. Then, complexity is reduced by turning off each of these forcings. Turning off wind and thermal forcings results in a numerical experiment only forced by lateral boundary conditions, therefore capable of sustaining the LC and associated eddies, this simulation along with the most realistic one are used to asses the indirect role of the wind over the GOM in altering the LC and LCE variability. The third of our diabatic experiments is performed only using wind and thermal forcings so lateral boundary conditions are turned off. This simulations is intended to give us more insights in the wind-driven circulation.

The second part of this study, is intended to give us additional undersatnding of the wind-driven circulation, and from the perspective of two different model configurations that differ in the representation of some physical processes. This set of simulations are called *adiabatic* because there is no exchange of heat between the atmosphere and the ocean, also, lateral boundary conditions are turned off. Three simulations are performed for every model configuration, each one forced by an annual, monthly and daily climatologies of wind respectively. In addition, a linear configuration of the model is done by removing the non-linear terms in the momentum equations, to provide a sverdrup-like approximation of the circulation in the GOM. This simulation is used in conjunction with the computed Sverdrup transport streamfunction using the mean wind stress curl and the wind-driven experiments to assess the role of different processes to the mean wind-driven transport.

CHAPTER 2

DESCRIPTION OF THE OCEAN MODEL AND BOUNDARY CONDITIONS

The Hybrid Coordinate Ocean Model (HYCOM) is one of the most widely used OGCMs in the oceanographic community and offers a wide variety of numerical choices presently available, from different mixed layer models, to parameterizations of important physical processes currently not completely understood. As most of the ocean models, it solves the hydrostatic primitive equations but stands out with respect to its vertical coordinate system. This chapter is intended to describe the most salient aspects of the HYCOM model used in this study with emphasis on the BB86-mode and HYCOM-mode (hybrid mode with KPP) configurations and the difference between them that are reflected in the results. Also, a description of the surface and lateral boundary conditions is provided.

2.1 Ocean models

2.1.1 HYCOM

The HYCOM model (Bleck, 2002; Chassignet et al., 2003; Halliwell, 2004) is a hybrid (i.e., generalized vertical coordinates) ocean numerical model. The advantage of using a hybrid model resides in its ability to simplify the numerical implementation of several physical processes (e.g., mixed layer detrainment, convective adjustment, sea ice modeling) without harming the model basics. It also allows for an efficient vertical resolution throughout the water column. In one hand, z-layers, levels at constant fixed depth or pressure, work best to provide high vertical resolution near the surface within the mixed layer; meanwhile sigma coordinates or terrain-following levels are the best choice for modeling shallow coastal regions; the isopycnic coordinate works best for modeling the deep stratified ocean and is used to avoid spurious mixing arising from the Eulerian vertical coordinates i.e., the diapycnal mixing is explicitly prescribed or parameterized (see Chassignet et al. (2003, 2006)). To ensure the conservation of mass on model layers, the layer thickness responds to the divergence of the mass flux field, dilating each layer as necessary which is done using the

flux-corrected transport (FCT) scheme of Zalesak (1979). Also, a leap-frog, second-order centered scheme is used for momentum advection. A decomposition is made between the fast external mode and the slower internal mode by subtracting the depth-averaged velocity to create a "barotropic" velocity in each layer. The momentum equations for these "internal" and "external" modes are then solved separately, this is called time splitting.

The K-Profile Parameterization (KPP, Large et al., 1994; 1997) is the default non-slab mixed layer model in HYCOM, and the one used in most of the experiments in this study. The KPP model offers mixing from surface to bottom, efficiently matching the large surface boundary layer diffusivity/viscosity profiles to the weak diapycnal diffusivity/viscosity profiles of the interior ocean. This model functions on a relatively coarse and unevenly spaced vertical grid. It parameterizes the influence of a larger group of physical processes than other frequently used mixing schemes. In the ocean interior, the role of background internal wave breaking, shear instability mixing, and double diffusion (both salt fingering and diffusive instability) are parameterized. In the surface boundary layer, there is parameterization of wind-driven mixing influences, surface buoyancy fluxes, and convective instability. The KPP algorithm also parameterizes the influence of nonlocal mixing of S and T, which allows for the development of counter-gradient fluxes (Wallcraft et al., 2009).

As described in section 1.3, a linear version of the model is used to mimic the Sverdrup dynamics. To this end, the nonlinear terms of equation 5.2 were removed in the model source code (specifically, the second term, curl of kinetic energy, and the relative vorticity within the third term of equation 5.2). This ensures that we get a result as close as possible to what the Sverdrup relation gives.

2.1.2   BB86-HYCOM

The BB86-HYCOM model is based on the isopycnic coordinate model of Bleck and Boudra (1986). This model also takes advantage of the FCT method. Unlike HYCOM, BB86 does not have a hybrid nor a mixed layer model. The wind stress is assumed to decrease linearly over a depth that in these experiments is chosen to be 100 m, which is tantamount to distributing the wind forcing among coordinate layers found within the 100 m of the surface using a linear stress law.

2.1.3 Experimental setup

The present model configuration is equivalent to the one used by Dukhovskoy et al. (2015), except for the horizontal resolution, which is lower in the present setup. The model domain corresponding to the Gulf of Mexico is configured from 18^oN to 32^oN and 98^oW to 77^oW (Fig. 1.1), therefore covering the northwestern Caribbean Sea and part of the western North Atlantic Ocean, with a $1/12^o$ (~ 8 km) horizontal resolution and 20 hybrid vertical layers, which are mainly isopycnal layers in the open ocean below the mixed layer and z-layers above it (see complete description of the hybrid coordinate system in Chassignet et al. (2003, 2005)). The target densities (Table 2.3), which define the vertical grid in the model, represent the density range of water masses in the GoM and northwestern Caribbean. The vertical grid is configured such that the upper ocean gains most of the vertical resolution and is able to represent the major features of the vertical structure of the flow. The model bathymetry is derived from the Naval Research Laboratory (NRL DBDB2).

The above are the common setup characteristics for all the simulations performed. However, the configuration of the diabatic and adiabatic simulations differ in specific aspects. Regarding the adiabatic wind-driven experiments, all of them were prescribed with closed boundaries over the Caribbean and western Atlantic using flat isopycnals as initial conditions and integrated from rest during 10 years. A relaxation to SST using an e-folding time of 30 days was defined for the **HYCOM-GOM** experiments as well as the KPP mixed layer model and hybgen module were activated. The depth over which the wind is applied was set to 100 m in the **BB86-GOM** experiments and was integrated from rest for 10 years. Suffix A, M and D denote experiments forced by annual, monthly and daily climatology respectively. The linear experiment, done by removing the nonlinear terms in the momentum equations, is named HYCOM-lin. Table 2.1 summarizes the specifications of each experiment.

On the other hand, regarding the diabatic simulations, experiment **OBW-12** has open boundaries conditions and was prescribed with atmospheric forcing derived from hourly fields of the Climate Forecast System Reanalysis (CFSR 1992-2010, both described in detail in the following section), this is the most realistic experiment, meanwhile **OBNoW-12** only has open boundaries conditions and no wind forcing, both simulations were initialized from a 5-year spin-up run that started from rest with the Generalized Digital Environmental Model 4.0 (GDEM4) climatological fields with atmospheric fields from the Fleet Numerical Meteorology and Oceanography Center's

Table 2.1: Specifications of the diabatic experiments.

Experiment	Open boundaries	Atmospheric CFSR	Lenght (years)	Resolution	Initialization
OBW-12	Bi-weekly clim	Hourly	57	$1/12^o$	Hotstart, GDEM4
OBNoW-12	Bi-weekly clim	No	57	$1/12^o$	Hotstart, GDEM4
NoOBW-12	No	Hourly	57	$1/12^o$	Rest, flat isopycnals

Table 2.2: Specifications of the adiabatic (wind-driven) experiments.

Experiment	Wind (CFSR)	Length (yrs)	SST Relax	Initialization	KPP	Hybgen
BB86-GOM-A	Annual	10	No	Flat	No	No
BB86-GOM-M	Monthly	10	No	Flat	No	No
BB86-GOM-D	Daily	10	No	Flat	No	No
HYCOM-GOM-A	Annual	10	Yes	Flat	Yes	Yes
HYCOM-GOM-M	Monthly	10	Yes	Flat	Yes	Yes
HYCOM-GOM-D	Daily	10	Yes	Flat	Yes	Yes
HYCOM-lin	Annual	10	Yes	Flat	Yes	Yes

Navy Operational Global Atmospheric Prediction System (NOGAPS). Following spin-up, OBW-12 was forced by the 19-year record of CFSR surface forcing and repeated three times (three cycles) to produce the continuous 57-year model integration. The last of this set of experiments is **NoOBW-12** also forced by the same 57-year record of repeated CFSR surface forcing but has closed boundary conditions and was initialized from rest using flat isopycnals. Table 2.2 shows a summary of the diabatic experiments specifications.

2.2   Model forcing

2.2.1   Surface boundary conditions

For the present study the NCEP Climate Forecast System Reanalysis (CFSR) dataset is used. The CFSR is a third generation reanalysis product and is described in great detail in Saha et

Table 2.3: Layer thickness and target densities for all the experiments.

Layer number	Target density (sigma)	Depth (m)
1	22.2460	0
2	22.3235	1
3	22.4143	6
4	22.6081	11
5	22.9391	16
6	23.3182	26
7	23.8008	36
8	24.3954	56
9	25.1896	81
10	25.9331	131
11	26.5490	181
12	26.9027	281
13	27.1751	381
14	27.3880	581
15	27.5952	781
16	27.7198	1281
17	27.7723	1781
18	27.8031	2281
19	27.8190	2781
20	27.8200	3281

al. (2006). It is a global, high resolution, coupled atmosphere- ocean-land surface-sea ice system designed to provide the best estimate of the state of these coupled domains over this period. The CFSR includes (1) coupling of atmosphere and ocean during the generation of the 6 hour guess field, (2) an interactive sea-ice model, and (3) assimilation of satellite radiances which is noteworthy since it incorporates more data into its assimilation system. It currently covers a 19 year period 1992-2010, uses very high horizontal resolution (38km) with 64 vertical levels and high frequency output (1-hourly). The hourly output fields are provided in the form of analysis fields every six hours, with hourly forecast fields for the intermediate time steps. The dataset provides 10-m wind speed, vector wind stress, 2-m air temperature, 2-m atmospheric humidity, surface shortwave and longwave heat fluxes, and precipitation. HYCOM.org provides the access to this and several other global and regional datasets.

For the purpose of studying the role of the wind in driving the circulation of the GOM at

different time scales, three climatologies or long-term average were derived from the 19-year hourly CFSR wind forcing. The daily climatology (a mean value for each day over the 19 years) was made by producing 365-day record files for each year and then averaging over all the years. Similarly, the monthly climatology was made from 12-month record files for each year and averaging over the 19 years. Finally the annual climatology was made by averaging over the entire 19 years and producing a single-record file.

2.2.2 Lateral boundary conditions

Experiments OBW-12 and OBNoW-12 have open boundary conditions derived from a bi-weekly (every 14 days) climatology produced by four years (2000-2003) of a free-running simulation of the $1/12^o$ Atlantic HYCOM. The $1/12^o$ Atlantic, used as the outer model, covers a domain from 27.9^oS to 70^oN and from 98^oW to 36.2^oE. It is important to note that no interannual variability is imposed at the lateral open boundaries.

CHAPTER 3

THE DIABATIC EXPERIMENTS (WIND AND HEAT FLUX)

The relative role of the wind stress and the LC in driving the GoM circulation has been historically under continuous debate. The current consensus is that the upper layer dynamics of the GoM is dominated by the LC and the westward migration of associated energetic mesoscale eddies (e.g., Elliot, 1982; Hamilton et al., 1999; Oey et al., 2005; Schmitz et al., 2005) superimposed on a mean wind-driven anticyclonic gyre (e.g. Sturges and Blaha, 1976, DiMarco et al., 2005; Sturges, 1993). The aim of this chapter is to quantify the "indirect" effect of the surface forcing over the GoM on the LC and LCEs intrinsic variability using a comparatively long record of LCE separation events from a set of diabatic numerical simulations, in the sense that the ocean exchanges heat with the atmosphere as described in the previous chapter. We also use experiment **OBW-25**, a twin experiment of OBW-12 but run in a $1/25^o$ resolution (used and described in Dukhovskoy et al., 2015), with the purpose of comparing and validating LC metrics.

3.1   Introduction

Initial (80's and 90's) numerical studies in the GoM (Hurlburt and Thompson, 1980; Smith, 1986; Sturges et al., 1992; Oey, 1996, Zavala, 1997, and more) focused on reproducing the most important features identified by observational studies (the LC, LCEs, western anticyclone gyre, and BOC cyclonic circulation) at that time (Sturges and Blaha, 1976; Merrell and Morrison, 1981; Elliot, 1982; Sturges and Evans, 1983; Sturges, 1993, and more) with particular attention in providing the simplest model configuration possible capable of achieving this, in order to reduce the computational cost. These authors not only succeeded remarkably, but made enormous progress in the understanding of the Gulf of Mexico LC driving mechanisms and laid the foundations for future studies based on the open questions remaining. With the advent of a new satellite era, which facilitated the use of altimeter data to infer the large-scale surface circulation by means of the geostrophic balance and as an integration of the ocean interior, and the existence of more

sophisticated instrumentation, observational data with higher temporal and spatial coverage became more available. This, along with the exponential growth of computational capabilities, made previous challenges more achievable.

Examples of previous challenges in numerical models were the accurate representation of the intricate dynamics of the LC, the frequency of LCE separation (Sturges, 1993; Oey, 1996; Romanou et al., 2004, Zavala et al., 2006), and the reproduction of a representative YC transport variability (Sturges, 1992; Ezer et al., 2003; Romanou et al., 2004). These authors demonstrated the relationship among these particular aspects and pointed out the importance of prescribing open boundary conditions farther enough from the Yucatan Channel to obtain a better representation of them within the GoM. They claim that this habit allows for a free dynamical interaction between the Caribbean sea and the GoM through the YC and mesoscale variability other than that due to surface forcing, and in some cases the allowance of remote influences like the North Brazilian Current and the Gulf Stream on eddy shedding frequency. Finally, perhaps less consistent among studies is the precise solution of LCE characteristics derived from numerical simulations such as size, path, translational and swirl speed, etc (e.g., Leben, 2005; Vukovich, 2007, 2012; Hamilton et al., 2015, Dukhovskoy et al., 2015). These discrepancies may be caused by a number of factors. Differences in methodologies employed for constructing gridded SSH fields, LC tracking, defining the LC frontal position, and handling missing observations may lead to a different result using the same dataset, although published studies are also based on different sets of observations.

In the present chapter, we first verify the agreement of some diagnostics performed to compare experiment OBW-12 with observations. Then, we quantify the effect of wind forcing on standard LC metrics such as LCE separation period and seasonality, LC northernmost and westernmost position as reported in previous studies (Dukhovskoy et al., 2015), LCE paths and distribution, as well as on the LCE characteristics. We also demonstrate that the number of LCE shedding events is apparently related to the degree of seasonality, or more properly, non-uniformity on their distribution, however the investigation of what causes such seasonality goes beyond the scope of this study. In particular: a) the most realistic experiment (OBW-12) has accurately reproduced the LC metrics computed from previous numerical and observational studies and, b) LC metrics among experiments OBW-12 and OBNoW-12 show statistically significant differences. As noted
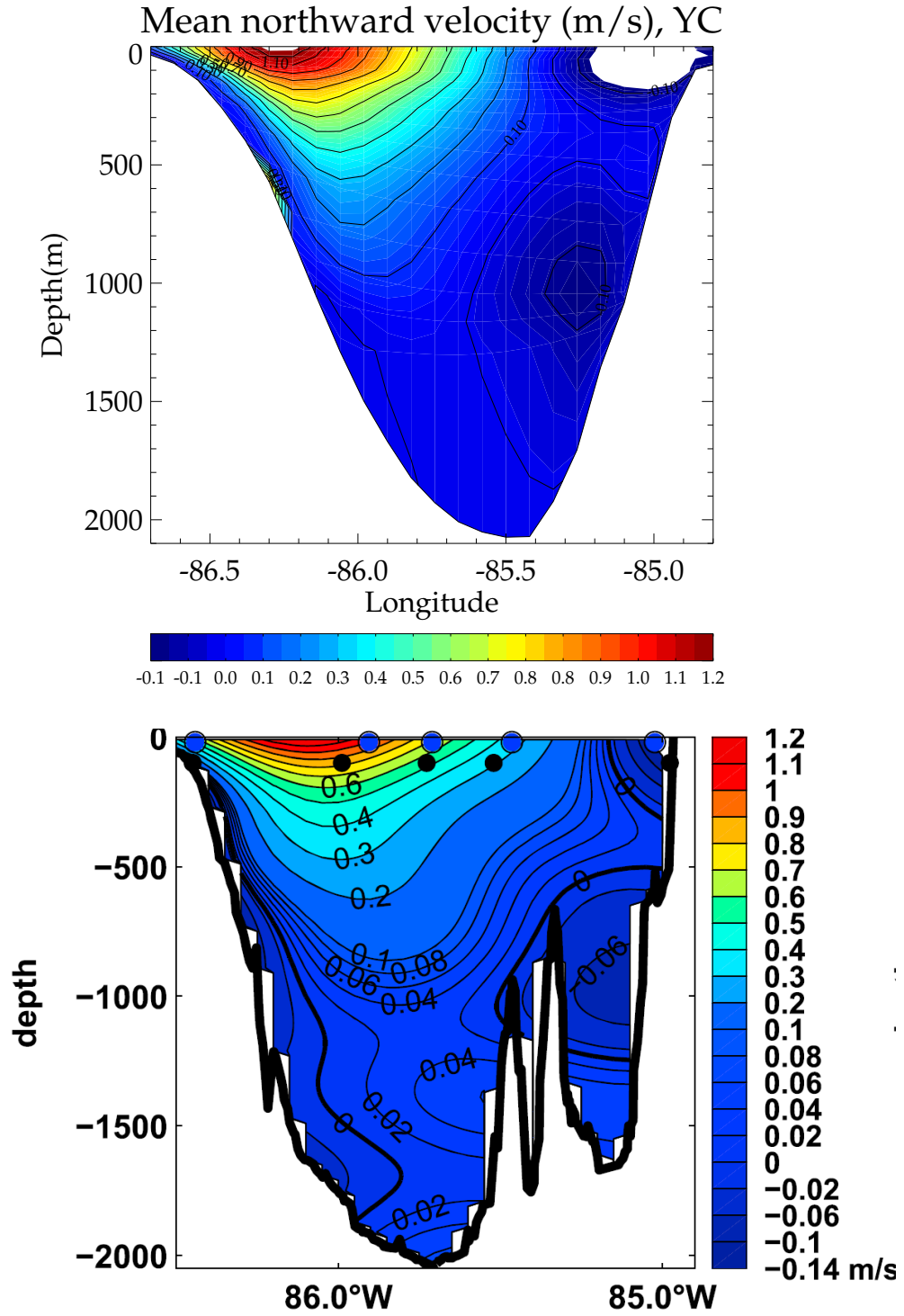
Figure 3.1: Northward velocity through the YC averaged over the entire 57 years of the simulation, exp OBW-12 (top) and from observations (bottom, Athie et al., 2015) .
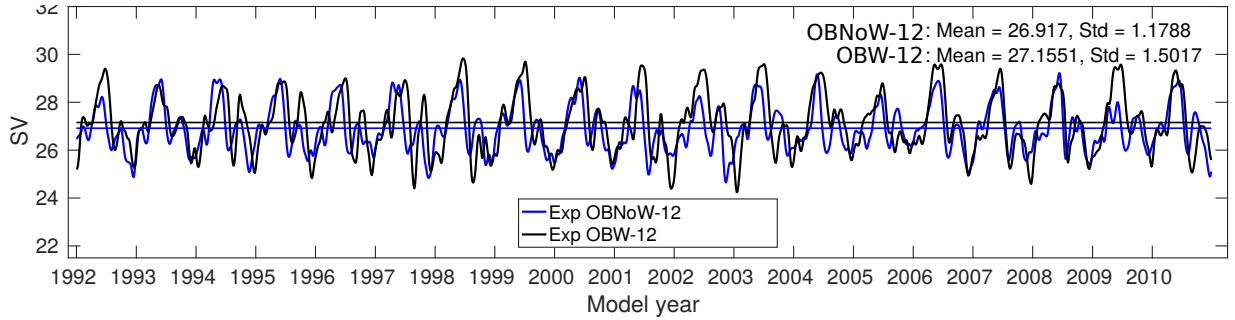
Figure 3.2: Mean transport through the YC for experiments OBW-12 (black line) and OBNoW-12 (blue line) for the first 19 years (1st cycle). Mean value for both experiments is ~ 27 Sv, and published estimates range from 23-30 Sv, (Sheinbaum, 2002; Rousset and Beal, 2010; Athie et al., 2015).

in the background section, these outcomes are important to consider when addressing the above objectives.

3.2   Comparison of model outputs with observations

Since numerical ocean models provide an approximate solution to the oceans state, it is necessary to verify the performance of the model. Such verification is performed to experiment OBW-12 as this represents the most realistic simulation. The results show that it resolves the most important features of the GoM circulation, namely, the LC northwesward extensions, LCE shedding and west-southwest trajectories, LCE detachments and reatachments, and the anticyclonic and semi-permanent cyclonic gyres in the western GoM and BOC respectively. In intermediate waters, more specifically about 1000 m depth which is the average depth of the 17th layer interface, the regime transitions from anticyclonic in the surface and subsurface to mean cyclonic circulation, consistent with observations and other numerical studies (Sturges, 2004; Hamilton. 2015).

Figure 3.1 shows the mean northward velocity structure through the YC at $\sim 22^o$N for the 57 years of the simulation, with a zoom on the upper 500 m, (top) and for a 2-year period of mooring observations during the CANEK program, from May 2010 to May 2011 and July 2012 to June 2013 (bottom, Athie et al., 2015). The distribution of inflows and outflows is consistent with observations. The main Yucatan current, Counter-current and Undercurrent are in overall well represented, with the core of the Yucatan main current placed at $\sim 86.28^o$W, somewhat west
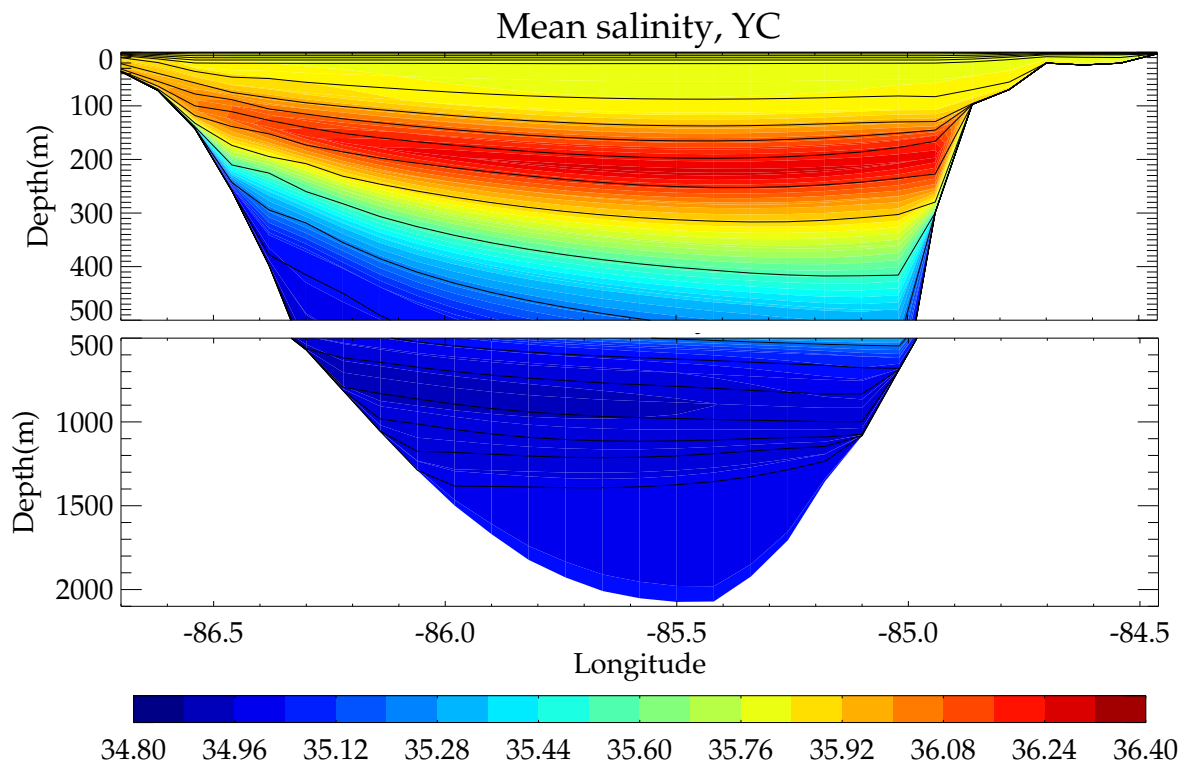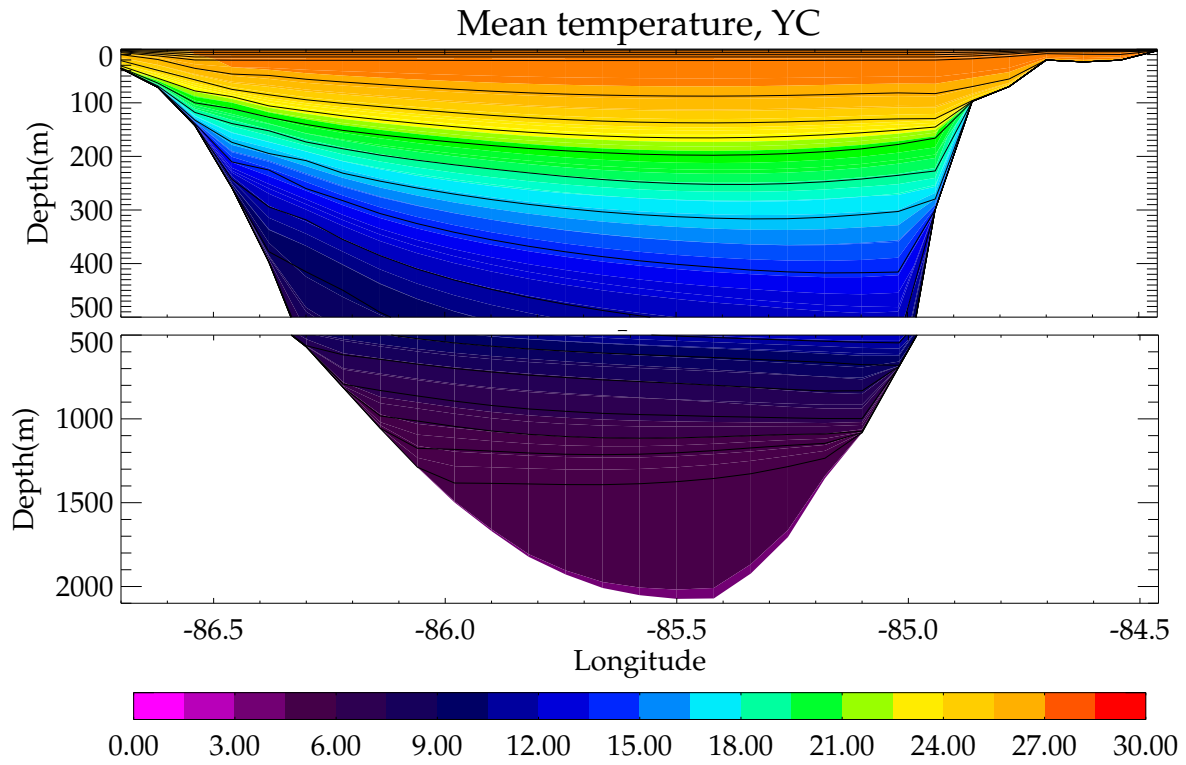
Figure 3.3: Mean vertical distribution of the model temperature (in ^{o} Celsius, top) and salinity (PSU, bottom) averaged over the entire 57 years of the simulation, exp OBW-12 and interfaces of the hybrid vertical layers.

compared to observations. However the strength of the current is remarkably in good-agreement, taking the 0.3 m/s contour as a reference, the model resolves the depth at which it's placed very well, which is about 500 m. Also the 0 m/s contours around the Counter-current and Undercurrent are well resolved, as well as the strength of the currents.

Early estimates of the mean transport across the Yucatan Channel obtained 23.8 +/−1 Sv (Sheinbaum et al. 2002) from a 10-month period of current meter moorings during the CANEK program; the transport values range from 13.5 to 31.7 Sv. Romanou et al. (2004) obtained a 27 Sv mean transport across the YC derived from a numerical simulation using MICOM and COADS forcing, with values ranging from 18 to 32 Sv over 5 years of analysis. Results from Athie et al. (2015), within the same CANEK program, yield a mean transport of 27 and 25 Sv for the two 1-year periods of measurements mentioned above respectively, with a subinertial standard deviation of 3.5 Sv. Through an analysis of low-frequency variations of transport proxy based on 20 years of altimetry data, the authors found that during 1999-2001, the flow through YC was anomalously low, explaining the comparatively low values reported by Sheinbaum et al. (2002). Figure 3.2 shows the time series of transport through the YC calculated using the section in Fig. 3.1 (top) from experiments OBW-12 and OBNoW-12 (black and blue lines respectively), both estimates yield a mean of ∼ 27 Sv and their respective standard deviations, 1.5 Sv for OBW-12 and 1.1 for OBNoW-12, are at least 2 Sv lower than reported by Athie et al., however OBW-12 shows a relatively higher standard deviation than OBNoW-12, indicating stronger variations of transport induced by the wind. Finally, Figure 3.3 shows the vertical structure of the temperature (top) and salinity (bottom) in the YC. It is noticeable that the salinity structure depicts the subsurface salinity maximum previously reported.

3.3   Mean circulation

The mean circulation is examined by averaging each of the diabatic experiments through the 57 years of 5-daily output. To this end, the mean velocity and SSH fields were obtained. As explained in Dukhovskoy et al. (2015), before averaging instantaneous SSH fields are demeaned by subtracting the spatial mean from each instantaneous SSH field, which is necessary to remove bias in the surface elevation fields associated with different reference surfaces and seasonal height variations due to upper-ocean warming and cooling (see Appendix A in Dukhovskoy et al. (2015),
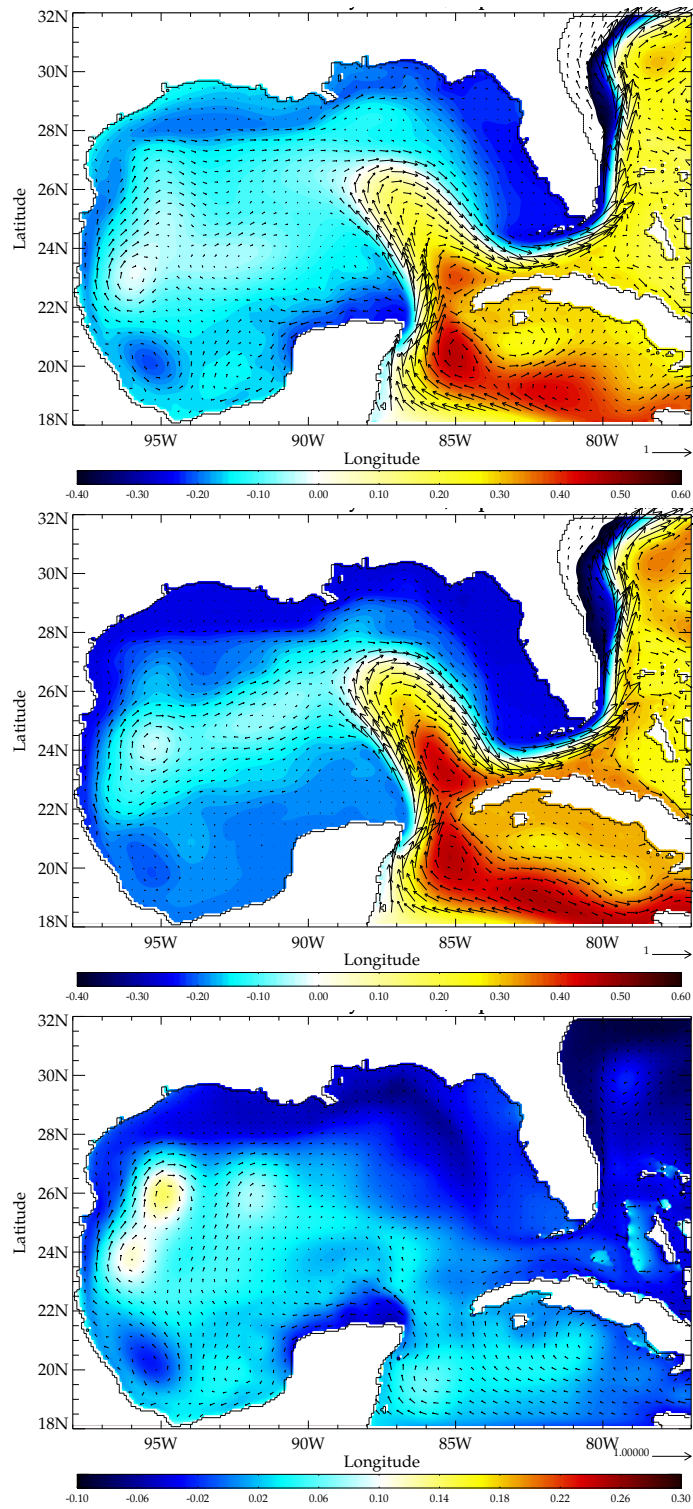
Figure 3.4: Time-averaged surface velocity and demeaned SSH through all the the simulations. Top panel: experiment OBW-12 which includes all the forcings; middle panel: experiment OBNoW-12 which is forced by lateral boundary conditions only; and bottom panel: experiment NoOBW-12 which is forced by hourly wind only.

for further clarification of mean and demeaned SSH fields). Figure 3.4, shows the maps of mean surface (~ 50 m depth) velocity and SSH for the three diabatic experiments. The following features can be observed: experiment OBW-12 (top left) shows the Loop Current on the eastern region of the GoM, a broad anti-cyclonic circulation over the central- and north-western regions located from 88°W to the western boundary of the domain and from 20°N to the northern boundary of the domain covering an area of 800 x 500 km approximately, represented by light blue color (negative anomalies after demeaning). On the BC, bound to the west, the semi-permanent cyclone previously mentioned is shown with center at 95.5^{o}W, 20°N and is represented by dark blue (a low in dynamic height).

Experiment OBNoW-12 (top right) depicts an area of high pressure which extends from the LC through the central-western region (in light blue color) which is related to the south-west trajectory of LCEs once they detach from the LC. Unlike experiment OBW-12, OBNoW-12 does not present a wide anticyclonic circulation. However, an interesting result is the presence of the low in dynamic height representing the cyclonic circulation on the BC in this experiment even without wind forcing. Perez-Brunius et al. (2013) stated that in the absence of forcing or dissipation, conservation of potential vorticity for large scale flows restricts the current to follow geostrophic contours, which are defined by f/H, where f is the coriolis parameter and H is the bottom depth, therefore fluid parcels are constrained to move along them. In the BOC, the topography of the western basin is such that it results in closed geostrophic contours, hence, flow can only exists across blocked contours in the presence of wind-stress curl or dissipation. The above could in part explain the permanent cyclonic circulation shown in the BOC of Figure 3.4 (top right), however we would need to do additional analysis to have a more solid conclusion. On the other hand, experiment NoOBW-12 (middle bottom) shows the anticyclonic circulation in the north-western region but also the cyclonic gyre in the western basin of the BOC. Vazquez de la Cerda et al. (2005) suggest the cyclonic gyre is driven by the positive wind-stress curl (Fig. 1.2 bottom), via Sverdrup dynamics applied to a flat seafloor. In addition, the calculations resulted consistent between the orders of magnitude of the Sverdrup transport estimated from the wind-stress curl, and the flow in either seasons. However, Perez-Brunius et al. (2013) suggest the need of an in-depth analysis to determine the role the winds play in the seasonal modulation of the cyclonic circulation. A discussion about

the type of flow being set by either the wind or another process like eddy-topography interaction or topographic confinement is done in section 4.5.

3.4   Impact of wind forcing on the LC and LCE variability

The influence of wind on LC variability derived from the 57-year simulations is presented by comparing results of experiments OBW-12 and OBNoW-12. To begin the examination, the distribution of LC northernmost and westernmost positions are obtained similarly as in Dukhovskoy et al. (2015). The LC and LCE fronts used to compute the metrics were produced with an objective tracking technique using the 0.17-m contour in demeaned SSH fields, for a more detailed explanation of this method see Dukhovskoy et al. (2015). The histograms of the northernmost latitude are shown in Figure 3.5 a and c, along with a probability density estimate (black curves). Both figures show a non-unimodal distribution. In fact, the distribution reveals bimodality with one mode centered on the 27-27.25 ^{o}N bin in both cases (Fig. 3.5 a and c) and another mode centered on the 24.75-25 ^{o}N bin for OBW-12 and 25-25.25^{o}N bin for OBNoW-12. This bimodality of the distribution of the LC northern extent indicates that there are two most common positions of the LC: the extended and retracted phases. Estimated parameters for each mode in the bimodal distributions are also listed in the figure. The difference of the histograms OBW-12 - OBNoW-12 (Fig. 3.5e) reveals that the LC tends to spend more time in the retracted phase below 25°N compared with the experiment without wind forcing. One reason for this behaviour can be suggested. If we remember, after an eddy detachment the LC tends to return to a retracted phase, therefore the fact that experiment OBW-12 sheds more LCEs could explain this behaviour.

Results from the objective tracking of detached LCEs for the 57-year period, identified a total of 65 separation events. The mean LCE separation period, which is the time between two consecutive separation events, is 10.5 months and the median is 9.5 months for experiment OBW-12. Meanwhile for experiment OBNoW-12 there were 53 separation events identified with a mean separation period of 12.9 months and a median of 11 months. Figure 3.6 shows the distribution of LCE separation events for experiments OBW-12 (a), OBNoW-12 (c), and OBW-25 (e) a higher-resolution twin experiment used and described in Dukhovskoy et al. (2015). In general there is good-agreement in the distribution of the LCE separation period derived from experiment OBW-12 and OBW-25. Moreover, OBW-25 is in turn in good-agreement with the distribution of LCE separation period

(a) LC northernmost pos, OBW-12
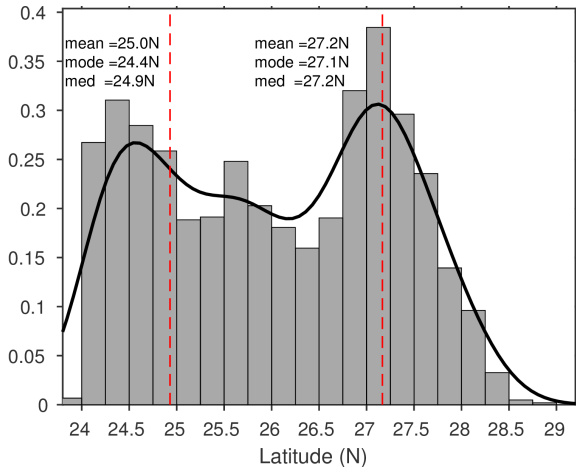
(b) LC westernmost pos, OBNoW-12
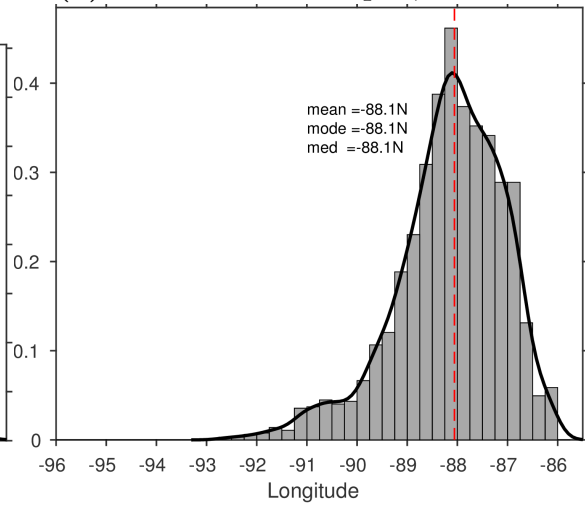
(c) LC northernmost pos, OBW-12
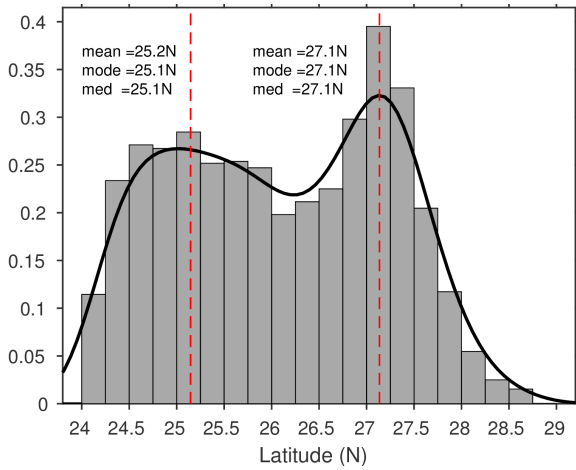
(d) LC westernmost pos, OBNoW-12
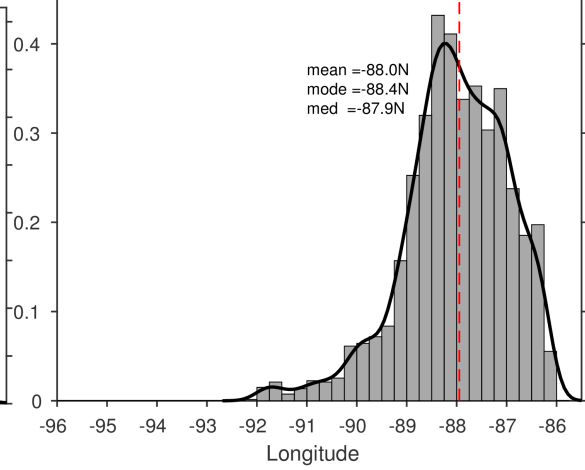
(e) OBW-12 - OBNoW-12
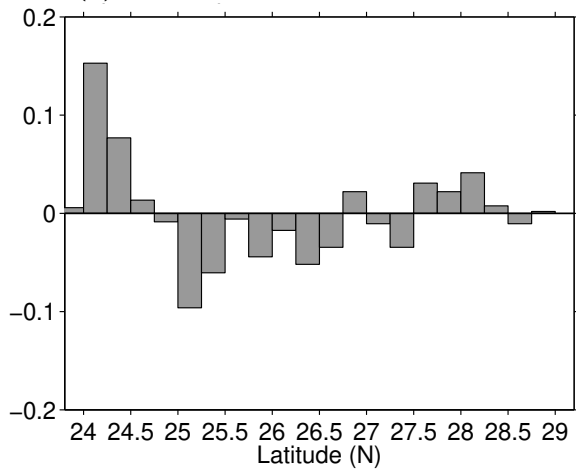
(f) OBW-12 - OBNoW-12
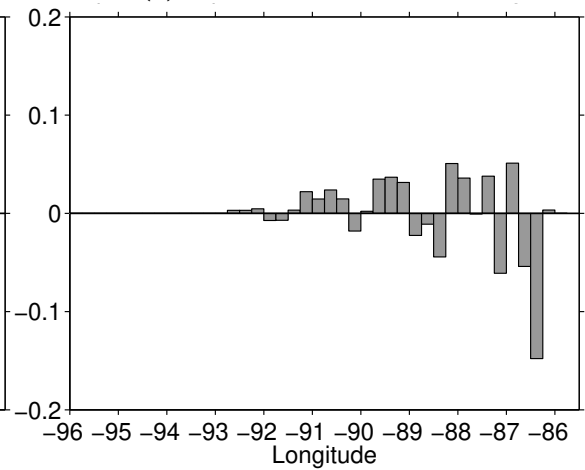
Figure 3.5: Histograms of the LC northernmost position (left) and westernmost position (right) for experiments OBW-12 (a,b) and OBNoW-12 (c,d). The difference OBW-12 - OBNoW-12 is shown in (e) and (f).

25
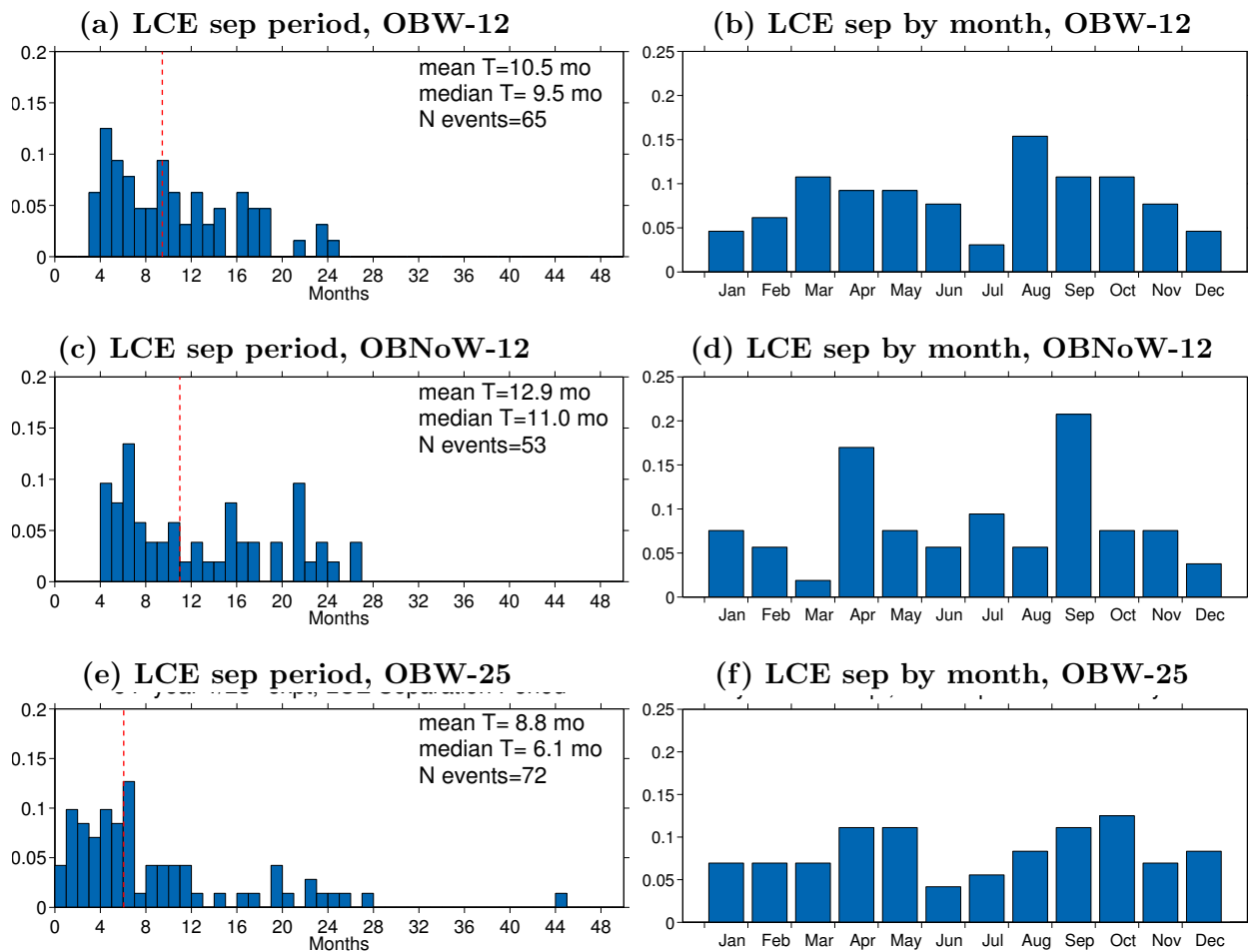
Figure 3.6: LCE separation period (left) and seasonal normalized histograms (right) for experiments OBW-12 (a-b), OBNoW-12 (c-d) and OBW-25 (e-f).

26

derived from CCAR SSH data. Perhaps the most evident difference between both distributions is the lack of consecutive LCEs whith separation period less than 4 months in the lower-resolution experiment OBW-12 (and also in exp. OBNoW-12), this behavior could be attributed for now to the model's inability to solve "small" LCEs which detach from the LC more frequently. Hypothesis testing applied to the mean LCE separation periods derived from the three experiments shows that the difference of means for experiments OBW-12 and OBW-25 is not significantly different from zero. Meanwhile the difference of means for OBW-12 and OBNoW-12 is significantly different from zero. In general, our results suggest that wind tends to increase the LCE shedding thereby reducing the separation period by $\sim 20\%$, this outcome is central to comprehending the role of wind on LC variability, although some attempts have been done in the past, we still need to understand the physical mechanisms by which wind over the GoM and Northwestern Caribbean Sea (CS) are affecting the system.

A consequence of having such a wide range of LCE separation periods (Fig. 3.6 a) is that LCE shedding can occur in virtually any month. Thus, there is interest in determining if the distribution of LCE separation events by month shows seasonality. The record of eddy shedding dates derived from the simulations was used to create such distribution of LCE separation events by month, also known as seasonal histogram, (Figs. 3.6 b,d and f). Focusing on the one corresponding to experiment OBW-12 (Fig. 3.6 b), it shows the biannual variability reported previously with a small peak in spring and a large peak in Fall. In order to test if this apparent seasonality is significant, the chi-squared (χ^2) statistical test was performed to test the hypothesis that LCE separation dates come from a uniform distribution. The chi-squared test is defined as:

$$\chi^2 = \sum_{i=1}^{N} \frac{(O_i - E_i)^2}{E_i} \tag{3.1}$$

where the observed values (O_i) are the values of the binned histograms and the expected values (E_i) come from a uniform monthly distribution consistent with the number of LCE separation events. To this end, data is binned quarterly to increase the number of counts per bin and have a better approximation of the statistic: Feb-Apr, May-Jul, Aug-Oct and Nov-Jan (Fig. 3.7 bottom). The computation shows that for experiment OBW-12, we obtain a Chi-squared value of 7, which means it improves our confidence to conclude that the seasonal distribution of separation events is not uniform at the 95% confidence level. On the other hand, in order to demonstrate the
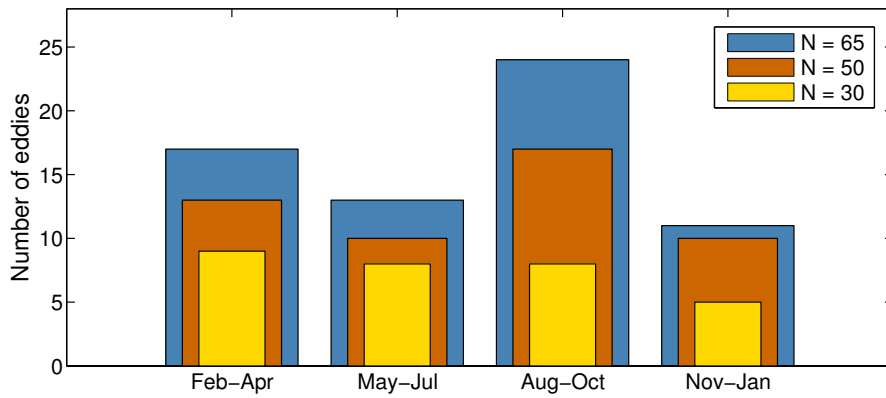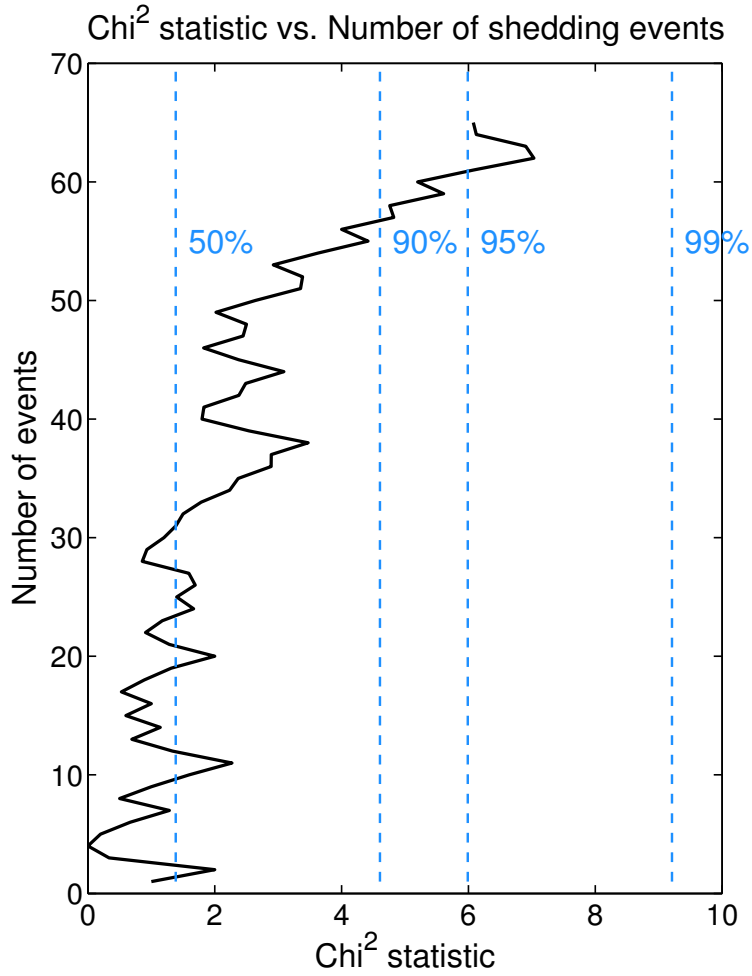
Figure 3.7: χ^2 statistic as a function of shedding events (top) and seasonal histogram for n = 30, 50 and 65 shedding events (bottom, yellow, orange and blue respectively). Experiment OBW-12.

Table 3.1: Mean LCE properties OBW-12 and OBNoW-12 experiments.

Experiment	No events	Area (x10^4 km^2)	Lifespan (days)	Transl speed (km/day)	Distance (km)
OBW-12	65	3.56 (1.82)	272 (138)	3.4 (1.4)	1340 (621)
OBNoW-12	53	2.88 (1.6)	271 (110)	2.99 (0.9)	1216 (374)

importance of the length of the record of shedding events on seasonality, the chi-squared statistic was computed as a function of the number of LCE separation events as shown in Figure 3.7 (top). The binned histograms for n = 30, 50 and 65 is also shown in Figure 3.7 (yellow, orange and blue bars, respectively), it can be seen that if the number of shedding events increase, then chi-squared value is high and the distribution becomes to show more seasonality, or more properly, becomes less uniform. In other words, the results show that after $\sim$ 50 events, the chi-squared statistic start to increase, improving the confidence level at which we can reject the hypothesis that the data come from a uniform distribution. Additionally, a t-test was performed to the peak in Aug-Oct for n = 65, and showed that the difference in the means between it and the rest of the peaks is statistically significant. The above results suggest that the record of LCE separation events derived from altimetry data may not be large enough to conclude that the distribution of LCE events by month shows seasonality.

3.5 Comparison of LCE characteristics between experiments OBW-12 and OBNoW-12

In order to continue the evaluation of the influence of wind forcing on the mesoscale activity in the GoM, some LCE characteristics are computed and compared between experiments OBW-12 and OBNoW-12. The objective tracking technique mentioned in the previous section is used to derive the study LCE properties, namely, LCE size, LCE central paths, spatial distribution, lifespan, and rotational and translational speed. The procedure to determine these properties is as follows: first, the tracking algorithm detects the 0.17 m closed contour of the LCE after detaching, then the area and center of the associated polygon are computed and recorded. The LCEs are tracked by comparing their centers at successive time frames (5-daily here) and this is done until the LCE is merged with another eddy or the area of the 0.17 m contour is less than 3000 km^2, at which time
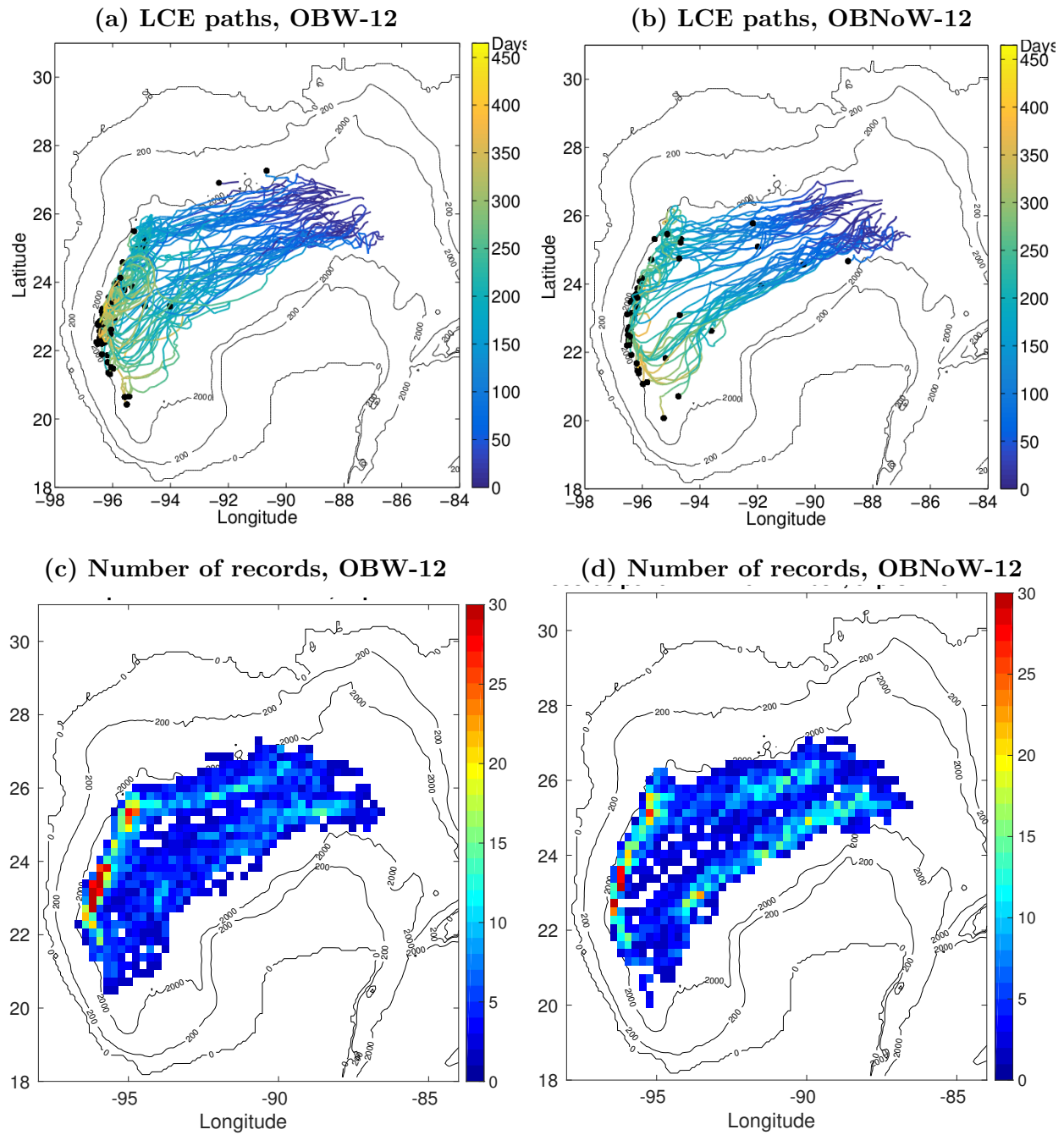
Figure 3.8: LCE central paths for experiment OBW-12 (a) and OBNoW-12 (b), and number of central paths records per 0.24^o x 0.24^o box for experiment OBW-12 (c) and OBNoW-12 (d).

it's considered to have dissipated and therefore the record of this particular path ends. A total of 65 and 53 LCEs were tracked in the 57-year record for experiments OBW-12 and OBNoW-12 respectively. Figures 3.8 a and b shows the individual LCE center paths through the western GoM colored by number of days after detachment for experiments OBW-12 and OBNoW-12 respectively. Some conclusions concerning the LCE paths are in agreement with previous studies (Hamilton et al. 1999; Donohue et al., 2008): in general, all paths depict a west-southwest trajectory, result of the combined effects of the β effect and a self-advective tendency. Most of LCEs dissipate through the western GoM west of 92^oW with centers in depths greater than 2000 m, and there is no apparent preferred direction in the trajectories along the western boundary. Also, it is clear in experiment OBNo-W12 that there are two preferred locations for LCEs to detach, one around 89^oW, 26^oN and another to the SouthEast around 88^oW, 25^oN. On the other hand, the occurrence density of modeled LCEs center paths in 0.24^o x 0.24^o boxes is illustrated in Figures 3.8 c and d. Both experiments results show the LCE paths covering the central GoM region and experiment OBW-12 shows that most frequently, LCEs are found over the shelf region in the western GoM.

Although the shape and size of a mesoscale eddy generally evolve during its life cycle, since its shape is not necessarily a regular circle, in the present study only the area of the LCE is computed as an overall measure of size. Nevertheless, our results give some insight on the role of wind forcing. Figure 3.10 (top) shows the distribution of LCE area after detachment for experiments OBW-12 and OBNoW-12. The mean value of each distribution indicates that OBW-12 LCEs are slightly bigger under the influence of the wind compared to OBNoW-12 on average right after detachment, 50874 km^2 against 50218 km^2. Perhaps more interesting is to examine the temporal evolution of LCEs. Figure 3.10 (bottom) shows the mean temporal evolution of LCE area for experiments OBW-12 (red) and OBNoW-12 (blue), vertical bars represent 1.5 standard deviations. For OBW-12 LCEs, area remains almost unchanged after $\sim$ 150 days, time when the LCEs undergo a growth in size before starting to decay in a quasi-linear fashion. Note that the standard deviation of LCE area becomes smaller due to smaller sample size. This secondary growth effect and sudden decay of LCE area was initially thought to be caused by the merging of two LCEs, however such assumption is discarded since merging is present in both experiments and OBNoW-12 does not present any second growth. Here we can assume that the bigger LCEs are the result of additional and continuing input of vorticity from the wind forcing and that the "quicker" decrease in mean area after this growth

31
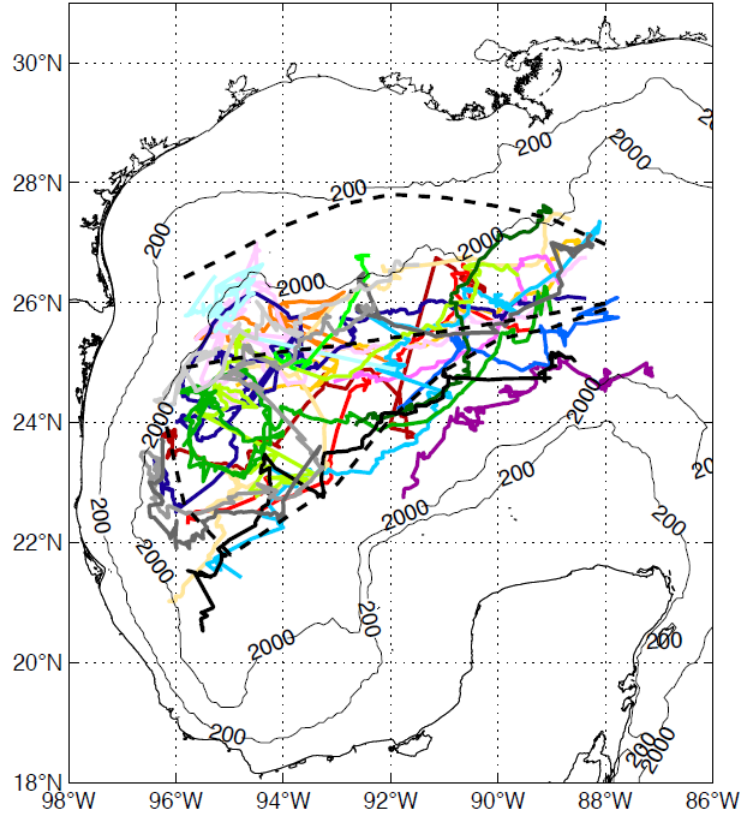
Figure 3.9: Altimeter-derived LCE center paths overlaid with the three prescribed from Vukovich, 2007. Taken from Donohue et al., 2008)

indicates dissipation of the eddies when they reach the western boundary. In fact, if we look at Figure 3.8 a, the color-coded LCE paths indicate that around 150-170 days some of the eddies reach the western boundary, specially those who separate from the LC at a latitude higher than $\sim 26^oN$. Moreover, if we add the mean translational speed plus one standard deviation, $\sim 3.4+1.4$ (km/day) (Table 3.1) times 150 days, we obtain 720 km, which is roughly the distance traveled to the west until they reach the western boundary $\sim 25.5^oN$ and $\sim 95^oW$, by an LCE separated above $\sim 26^oN$. On the other hand, OBNoW-12 LCEs (blue bars Fig. 3.10) do not present any increase in mean area but rather, a quasi-linear decay.

Our results also show that the mean lifetime for LCEs are roughly 272 and 271 days with standard deviations of 138 and 110 days for experiments OBW-12 and OBNoW-12 respectively (Table 3.1). These values fall within published estimates of ~ 6 months to one year (Elliot, 1982; Frolov,
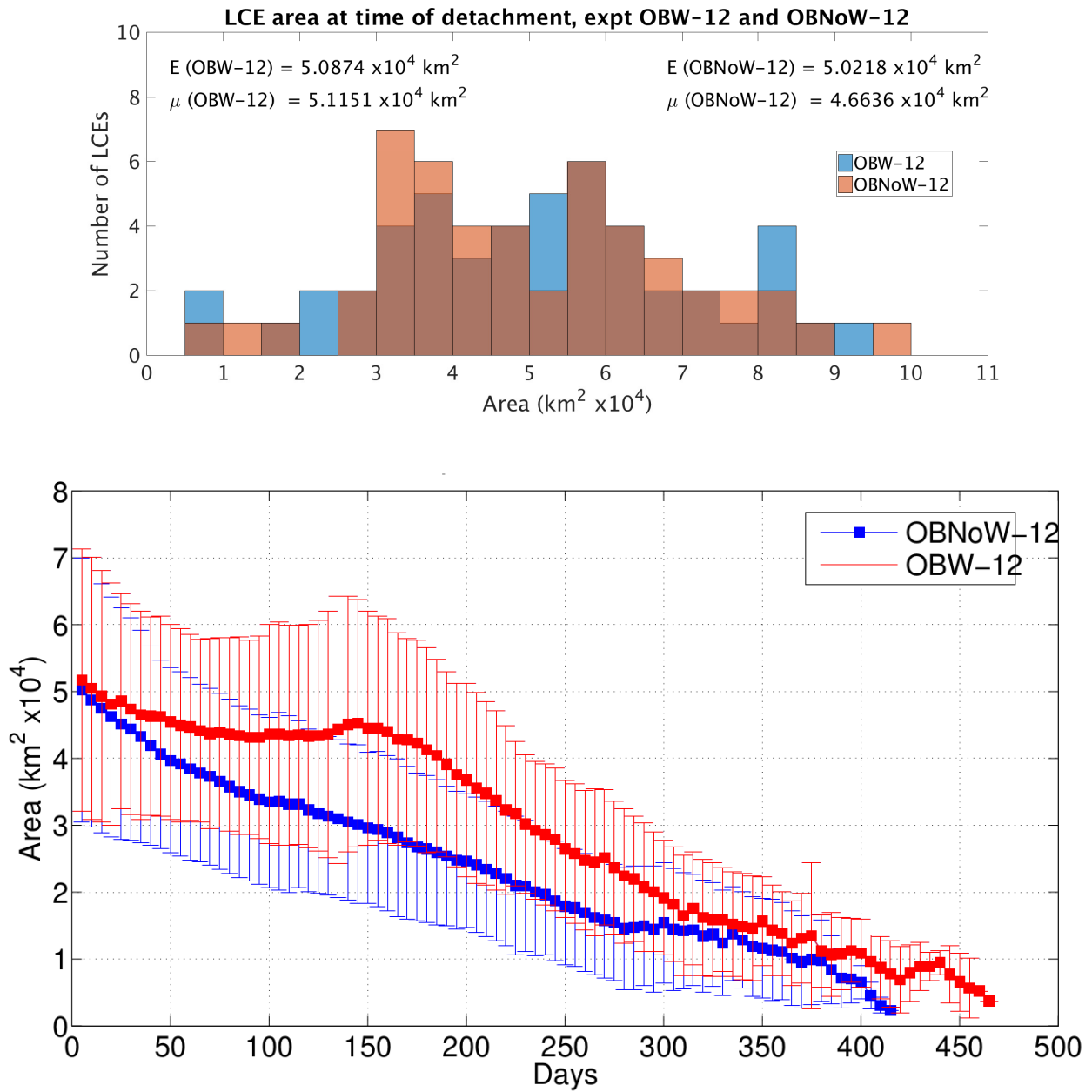
Figure 3.10: LCE area at time of detachment (top) for OBW-12 (blue bars) and OBNoW-12 (red bars); and time evolution of mean LCE area (bottom), vertical bars represent 1.5 std.

2004). Mean westward propagation speeds are 3.4 and 2.99 km/day with standard deviations of 1.4 and 0.9 km/day for OBW-12 and OBNoW-12 respectively. These results are comparable to several previous observational and numerical studies (Leben, 2005; Vukovich, 2007 and more) based on the westward long Rossby wave speed around these latitudes.

3.6   Summary and discussion

The LC is the most important circulation feature of the GoM because it is the feature with the highest energy (Elliot, 1982; Jaimes, 2005). Our numerical results show that in the western GoM, the mean circulation is characterized by two main features, a wide, intense, anticyclonic gyre in the north, and a small cyclonic, less-intense gyre in the BOC. The anticyclonic gyre can be induced by the LCEs in the absence of wind, however, with different pattern and intensity; the wind produces the most intense version of it. The results also support the idea that the cyclonic circulation in the BOC is the result of the wind stress curl and conservation of potential vorticity due to topographic control. However, we will show in the next chapter that other processes also play a role. We will make use of the numerical simulations to infer what we call the "indirect" effect of wind forcing on mean circulation, and LC and LCE variability through the comparison of standard LC metrics. Although covering all the physical arguments underlying the evident differences goes beyond the scope of this study, we mention the reasonable physical mechanisms speculated in published studies that may be controlling them.

We have performed a statistical study of the mesoscale LC and LCE activity in the GoM based on a set of free-running, multidecadal simulations configured for the GoM. We used an automatic LC and LCE frontal detection method to derive metrics used in the comparison and to track the LCEs, based in both physical properties and geometric characteristics of the SSH field. This method was applied to the 57-year OBW-12 and OBNoW-12 model simulations and then analyzed the detection results to investigate the kinematic properties and temporal variations of the LCEs. The studied metrics are the LC northern and western extents, LCE shedding separation period and seasonality, LCE propagation paths and spatial distribution, LCE size and lifetime, among others. For instance, no physical argument has been put forward as to why preferred LCE pathways depict the bimodal pattern shown in Figure 3.8. However it should be noted that some numerical model simulations have shown distinct eddy pathways (see, for example, Donohue et al. (2008)).
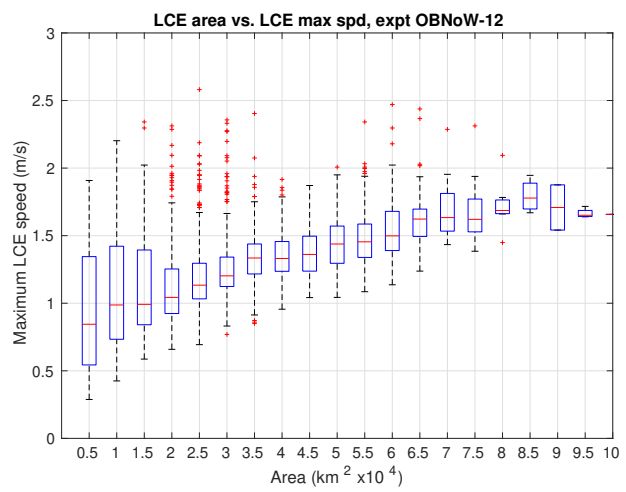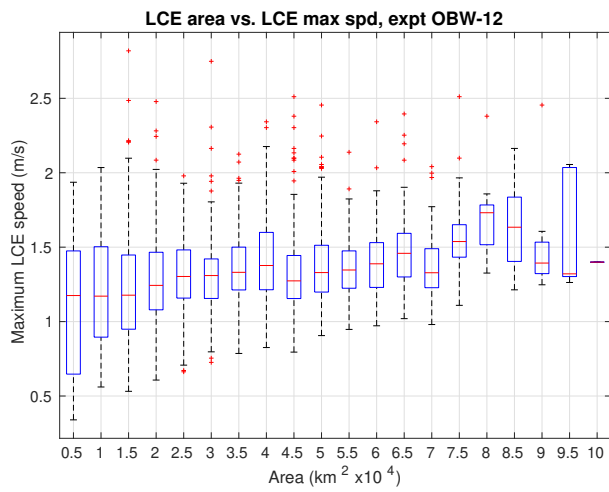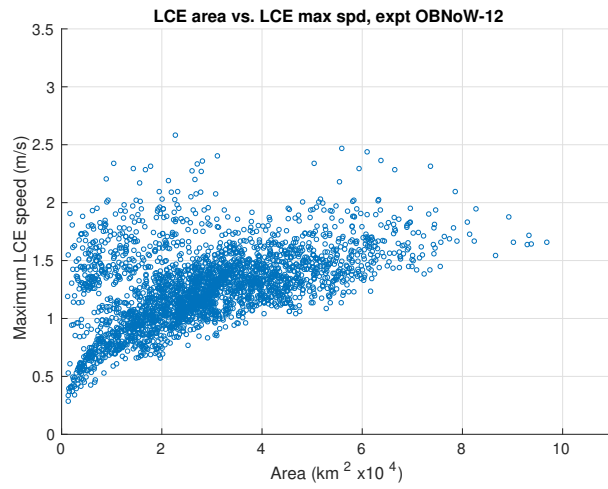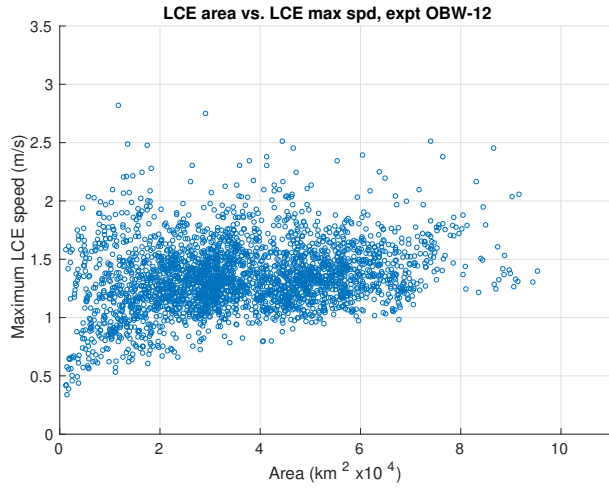
Figure 3.11: LCE area as a function of maximum rotational speed.

35

The distribution of LC northernmost position is strongly bimodal, with the LC tending to spend more time in the retracted phase in the presence of wind forcing. Since there is a reduction of LC area after an eddy separation (Leben, 2005; Hamilton et al., 2014), the LC changes to its retracted phase. Therefore, the fact that there are more shedding events in experiment OBW-12 than in OBNoW-12, may explain this behaviour in the histogram (Fig. 3.5). The mean LCE separation period varies from 10.5 months in OBW-12 to 12.9 months in OBNoW-12, hypotheses testing shows that their difference is significantly different from zero. It was found that the overall effect of the wind forcing increase the shedding of eddies, thereby reducing the mean LCE separation period by almost 20%, but tend to delay the shedding in certain months altering their seasonality.

In fact, the distribution of shedding events by month was demonstrated to depict some degree of seasonality. This fact suggest that the system must be, at least in part, forced by the wind although the mechanism by which this is done remains to be investigated. The chi-squared (χ^2) and t-test tests complement each other. On one hand χ^2 indicates whether a distribution of LCE separation dates exhibits statistically significant seasonality, meanwhile the t-test shows any months or seasons LCE separation is more significant or not. The χ^2 test on numerical-simulated LCE shedding dates show that the seasonal distribution of separation events is not uniform at the 95% confidence level. The t-test further show that the seasonal peak in LCE separation events in Aug-Oct is statistically significant. This suggests that the seasonal peak in Feb-March may become significant with a longer time series of separation events and longer altimeter-derived observations of separation events could improve significant seasonality. Finally we believe that a more focused set of numerical experiments could give more insight about factors/processes influencing seasonality in LCE shedding.

CHAPTER 4

THE ADIABATIC EXPERIMENTS (NO HEAT FLUX, WIND ONLY)

4.1 Introduction

The problem of whether the western anti-cyclonic circulation and the BOC quasi-permanent cyclonic circulation in the GoM are driven by the wind stress or by incoming LCEs has been a subject of historical debate and studied by several authors from different points of view. In this chapter, the wind-driven circulation in the GoM is first investigated using a set of closed-boundaries purely wind-driven experiments in which the time scale of the wind variability was increased from steady annual mean, to monthly and daily mean, through the use of two different model configurations that differ in the representation of their physics. In addition, a linear configuration of HYCOM and an estimate of the Sverdrup circulation derived from the wind stress are used to partition the wind-driven circulation into different factors. Also, with the aid of the mean barotropic velocity field, we infer the type of circulation being set by the wind and the LCEs in the BOC. Finally, the contribution of the wind and eddies to the mean circulation is quantified within three sub-regions in the western GoM using an estimate of the circulation.

4.2 Winds in the Gulf of Mexico

We begin our discussion of the wind-driven circulation in the GoM by describing some seasonal aspects of the surface winds over the gulf. Several studies have analyzed specific aspects of the winds over the GoM that are related with particular ocean processes (e.g. Oey, 1995; Zavala-Hidalgo et al., 2003; Morey et al., 2005; Nowlin et al., 2005; Vzquez de la Cerda et al., 2005 and more). The winds in the GoM present strong variability over different time and space scales, with very marked seasonality. They are important for processes like upwelling, mixed layer depth, surface fluxes, circulation and development of wind waves. Also important, are intense winds produced by tropical cyclones passing between June and November and cold fronts between September and May.

The winds over the GoM are part of the bi-annual trade winds which have a big influence on the North American continent. Figures 4.1 and 4.2 show the long-term monthly means computed from the CFSR data (19-year period, 1992-2010). It is observed that, during Summer (May-August), the wind blows toward the north in the northwestern GoM due to the influence of the North Atlantic semi-permanent atmospheric high-pressure system over the northeastern region. This pattern is probably reinforced by the high temperature over land driving a monsoonal effect (Zavala et al.,2014). Between May and August, winds are more intense in the western Gulf and are weaker in the northeast, with this pattern more evident in May (colored contours Fig. 4.1 e). In September, this wind pattern changes because the cold fronts associated with atmospheric high-pressure systems coming from the northwestern United States begin to reach the GoM and the semi-permanent high-pressure system over the Atlantic Ocean shifts northeastward. During Fall (September-November), the long-term monthly mean wind direction in the northern Gulf is mainly westward, with a small southward component. In the BOC an intense southward wind component develops, mainly in the western side of the bay, favored by a mountain blocking effect caused by the Sierra Madre Oriental in Mexico that directs the wind through the Isthmus of Tehuantepec where the mountain chain has a low altitude passage. In addition, the lower pressure in the Gulf of Tehuantepec also favors southward winds (Romero-Centeno et al., 2003). This pattern remains until February and it is more pronounced in December.

On the other hand, the time-averaged wind stress curl (Fig. 1.2 bottom) derived from the dataset shows negative (anticyclonic) values north of 23° N and positive (cyclonic) to the south, mainly in the western BOC. The zero wind stress curl contour line has a southeast-northwest orientation (Gutirrez de Velasco and Winant, 1996). According to monthly horizontal maps (not shown), the annual cycle of the wind stress curl is characterized by the displacement of the zero contour line, moving southward during spring and summer and northward in fall and winter. The largest negative values of the wind stress curl are observed in the northeastern GoM in summer and they became smaller in winter. During fall and winter, positive values are larger in the western Bay of Campeche (Gutirrez de Velasco and Winant, 1996).
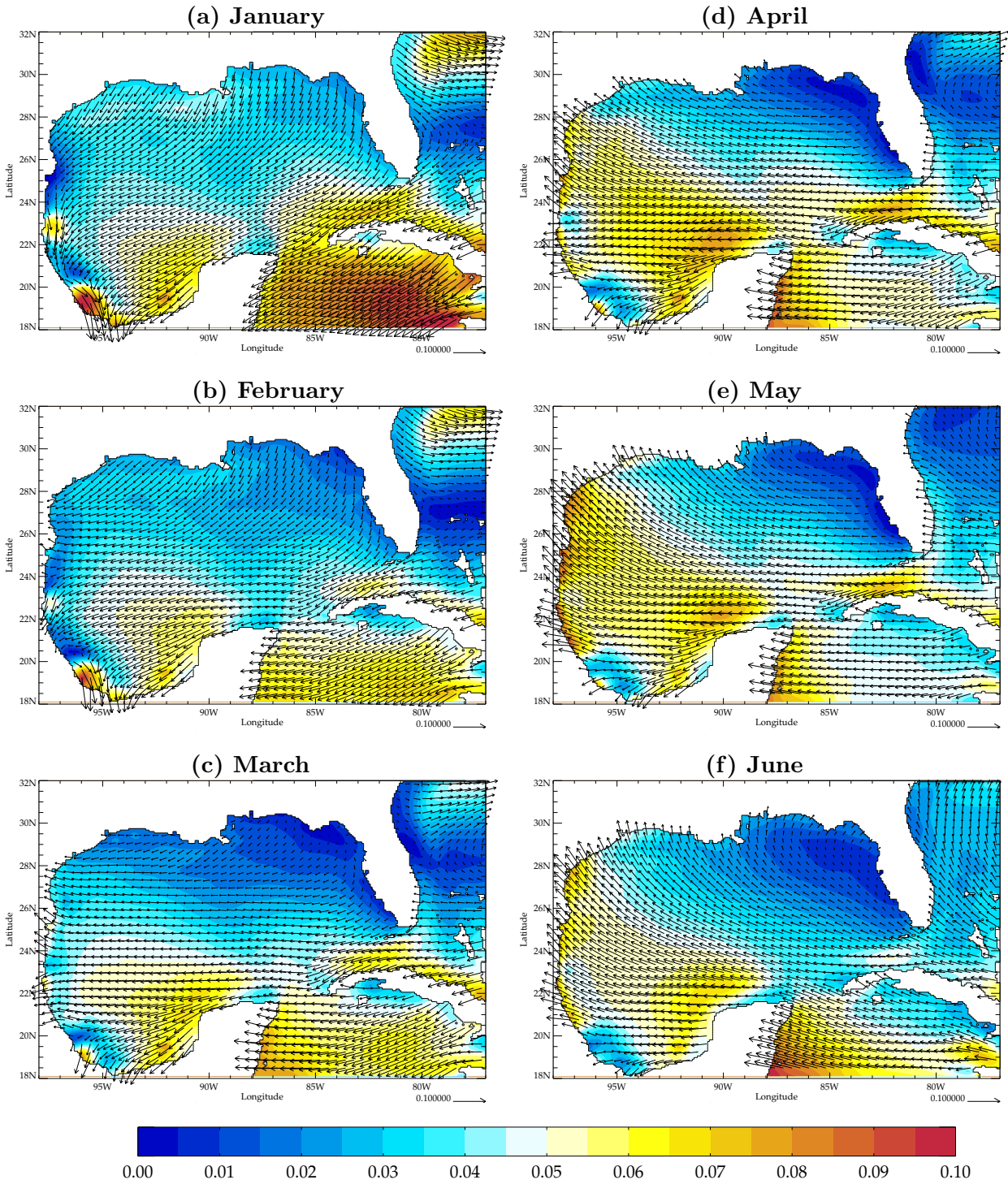
Figure 4.1: Long term monthly means of wind stress in the Gulf of Mexico based on the 19-year period of CFSR. Contours indicate wind stress magnitude (Pa) according to the color bar and arrows indicate wind stress.
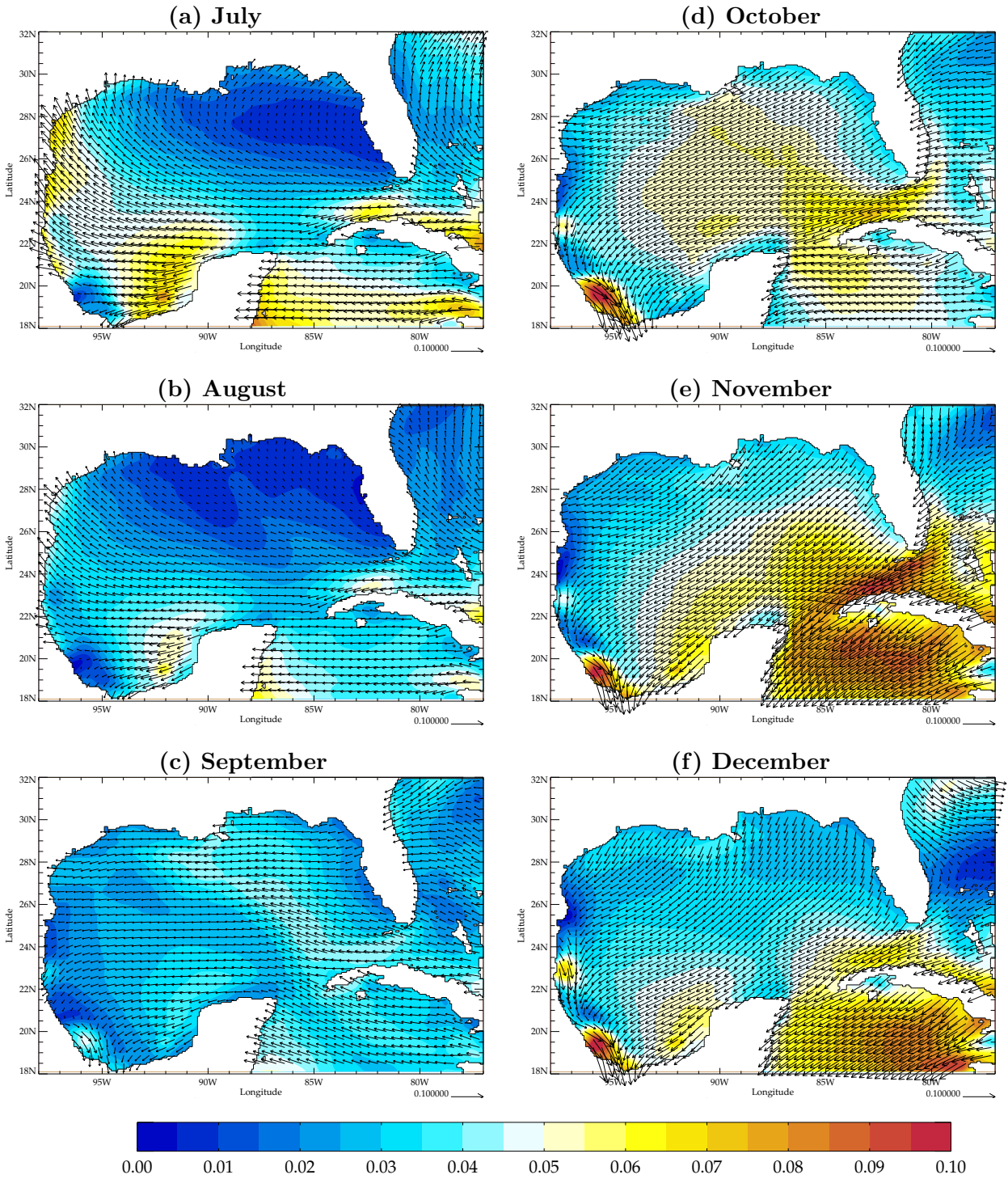
Figure 4.2: Long term monthly means of wind stress in the Gulf of Mexico based on the 19-year period of CFSR. Contours indicate wind stress magnitude (Pa) according to the colorbar and arrows indicate wind stress.

4.3   Wind-driven circulation features in the GoM

This section describes the dominant flow features over the last six years of the model simulations. To this end, three numerical experiments were set up for each model configuration (Sec. 2.1) with emphasis on the time scale of the variability of the wind forcing: experiments **BB86-GOM-A** and **HYCOM-GOM-A** are forced by a steady, annual mean wind (Fig. 1.2 top); experiments **BB86-GOM-M** and **HYCOM-GOM-M** are forced by a monthly mean wind; and experiments **BB86-GOM-D** and **HYCOM-GOM-D** are forced by a daily mean wind, all of these climatologies were computed using the CFSR dataset described in 2.2. Table 2.2 in section 2.1 summarizes the specifications of each experiment. On average, all six simulations reproduce several distinct features. The purpose of running these simulations is to quantify, in conjunction with the Sverdrup-like experiment described in the next section, the contribution of different factors to the wind-driven circulation.

Figure 4.3 shows the time evolution of region-wide mean kinetic energy (MKE), a diagnostic variable output from the model simulations, which is produced first by computing the global kinetic energy of the whole 3D domain and then dividing by the surface area, for the BB86-GOM (left panel) and HYCOM-GOM (right panel) configurations. According to its time evolution, MKE for the annual wind-forced experiment (black line) show a grow in the order of months, due to geostrophic adjustment, and an initial peak after $\sim$ 2 years, equilibrium is reached after this spin-up time. Although they don't possess any kind of seasonal variability, both MKEs behave differently after this time, experiment BB86-GOM-A does not really achieved a true steady state and continues increasing meanwhile the HYCOM-GOM-A experiment decays within about 2 years after the peak to reach a steady state. Now, the question is what could be producing this difference in behavior? Since energy input through wind stress is the same in both experiments, this could only be caused by a less effective dissipation mechanism in the BB86-GOM configuration, therefore this can be attributed to the fact that HYCOM-GOM has a mixed layer model (KPP).

On the other hand, circulation shows similar recurrent patterns between the two configurations. Inspection of the surface circulation with the aid of a movie showing the evolution of the velocity field and SSH, for each experiment, gives us more insight on the behavior of the flow. The movie shows that throughout years 3-10 of most of the simulations (after spin up time), the surface flow pattern is dominated by a slightly strong meandering Western Boundary Current (WBC) in the
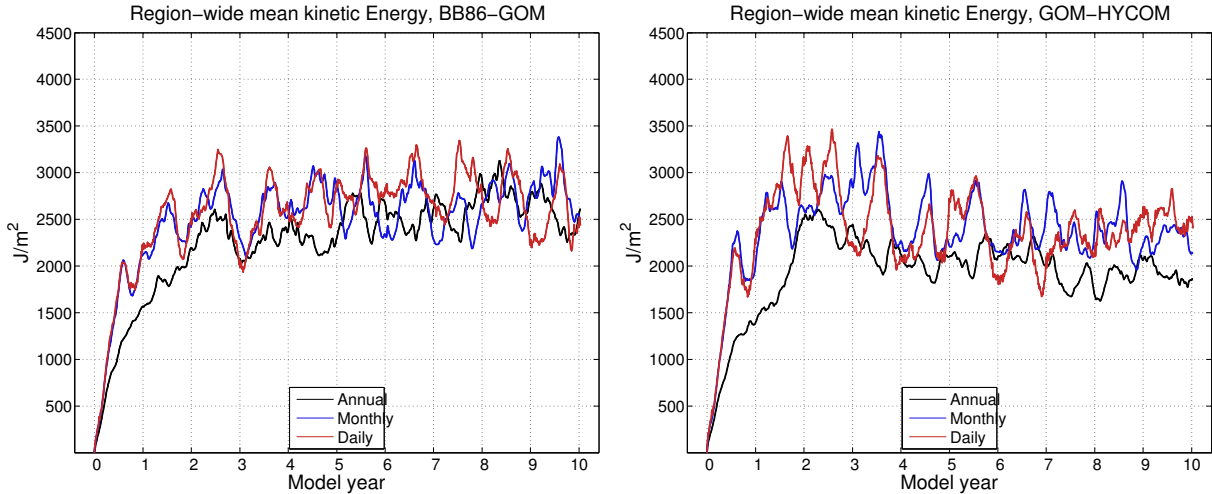
Figure 4.3: Global kinetic energy for BB86-GOM (left) and HYCOM-GOM (right) experiments.

northwestern part of the GoM. Every now and then, with no particular frequency, anticyclonic eddies form in the returning flow of the WBC and over the central region of the basin, some of which are intense enough to last $\sim 4 - 6$ months before they merge again with the WBC or with other eddies. It is also noticeable that these wind-induced eddies and the related circulation act solely over waters with depths greater than ~ 200 m and currents are weak over the continental shelf, therefore suggesting that these features extend several hundred of meters below. As mentioned above, these recurrent patterns are present in each wind-driven experiment, and the widths, directions, structure, and locations of these features all closely match. Therefore, we can conclude that the mean circulation in the GOM responds primarily to the large-scale, subinertial wind stress, and does not vary considerably with shorter temporal scale variability in the wind stress.

Another noticeable feature on the pattern apparent in the movie, is the presence of a cyclonic gyre on the Bay of Campeche (BOC) confined to the western basin (Vazquez De la Cerda, 2005; Perez-Brunius et al., 2013) which sometimes interacts with the WBC or with the anticyclonic eddies. This interaction is given by means of anticyclonic eddies' southern rims penetrating into the northern BOC and perturbing the cyclonic gyre's circulation. However, unlike what has been reported, the cyclonic gyre does not depict a stationary state but a semi-stationary state since approximately every few months, the cyclonic gyre moves northward over the western boundary and eventually dissipates, then a new cyclonic eddy forms on the BOC. This behavior is also
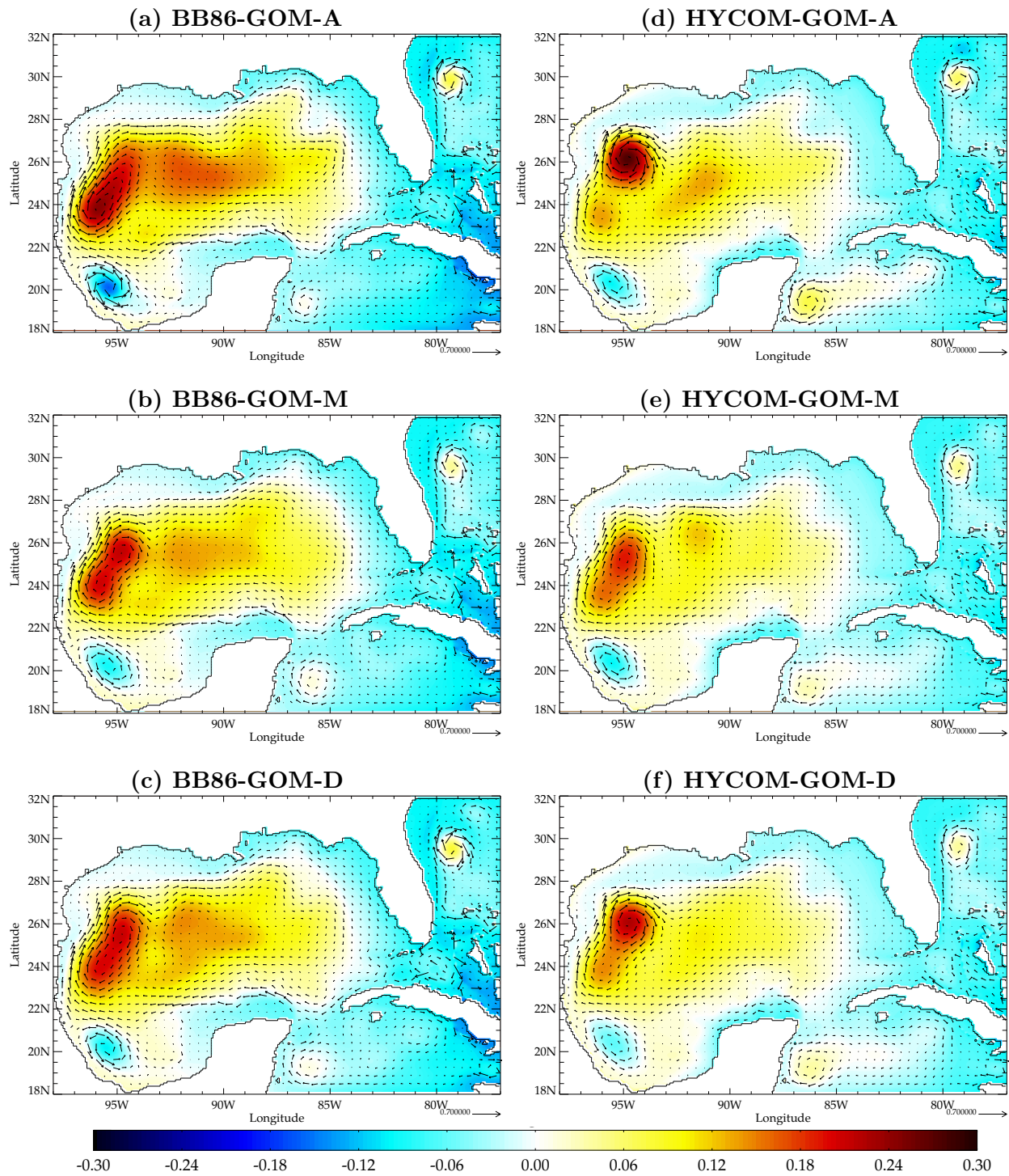
Figure 4.4: Time-averaged surface velocity and SSH over the last 6 years of the simulations for experiments BB86-GOM a-c and HYCOM-GOM d-f. Units of the colorbar are meters.
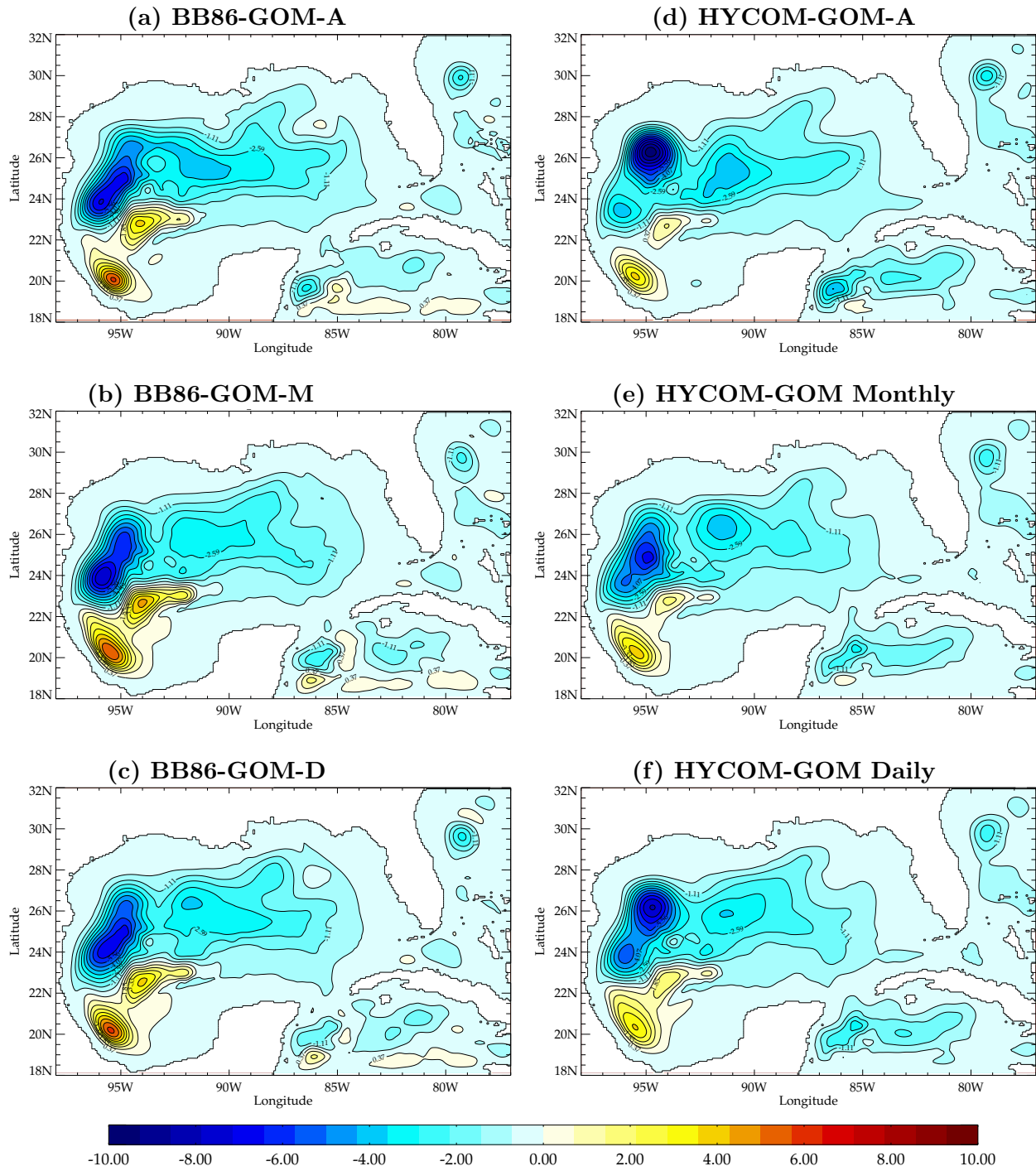
Figure 4.5: Mean barotropic streamfunction averaged over the last 6 years of the simulations for experiments BB86-GOM a-c and HYCOM-GOM d-f. Units of colorbar are Sv.

44

apparent in the monthly and daily wind-forced HYCOM-GOM experiments.

Figure 4.4 a-f shows the mean surface circulation and SSH for the six experiments, computed using the 5-daily output of the last 6 years of the simulations. All the mean circulation figures depict the features mentioned above: including a wide anticyclonic circulation represented by a high in dynamic height (yellow-red colors) and a comparably smaller cyclonic circulation at the BOC represented by a low in dynamic height (cyan-blue colors). However the relative magnitudes of these features may vary. The anticyclonic eddies formed at the southern boundary of the domain (between 87-77°W and 18-22°N), south of Cuba and the YC, and the stationary eddy at the northeast part of the domain, next to the Florida peninsula don't affect the circulation within the GOM in a significant manner according to some tests performed turning off the wind forcing over such areas and comparing.

The barotropic streamfunction averaged over the last six years of the simulation is shown in Figure 4.5 for all the experiments. All the mean maps show the wide anticyclonic circulation in the northern region of the gulf although the location of the maximum transport varies among them. The annual wind-driven experiments depict a quasi-permanent anticyclonic gyre in the northwestern gulf, specially in the HYCOM-GOM configuration. Meanwhile in the monthly and daily wind-driven simulations the gyre seems to have a more north-south trajectory along the western boundary, probably related to the seasonal variability of the wind over that region. According to Figure 1.2, the annual mean wind blows to the west northwest in this region and the curl is negative, favoring the permanence of the anticyclonic gyre. Therefore, the variation of the winds over the western boundary from April-July towards the north to October-January towards the south allows the gyre to shift north to south.

On the other hand, according to the MKE, equilibrium is reached after 1-2 years of spin-up time for the monthly and daily wind-forced experiments, showing an annual signal with spikes every year and a more rapid increase within the first year unlike the annual wind-diven experiment which exhibited behaviour that was more random and less energetic.
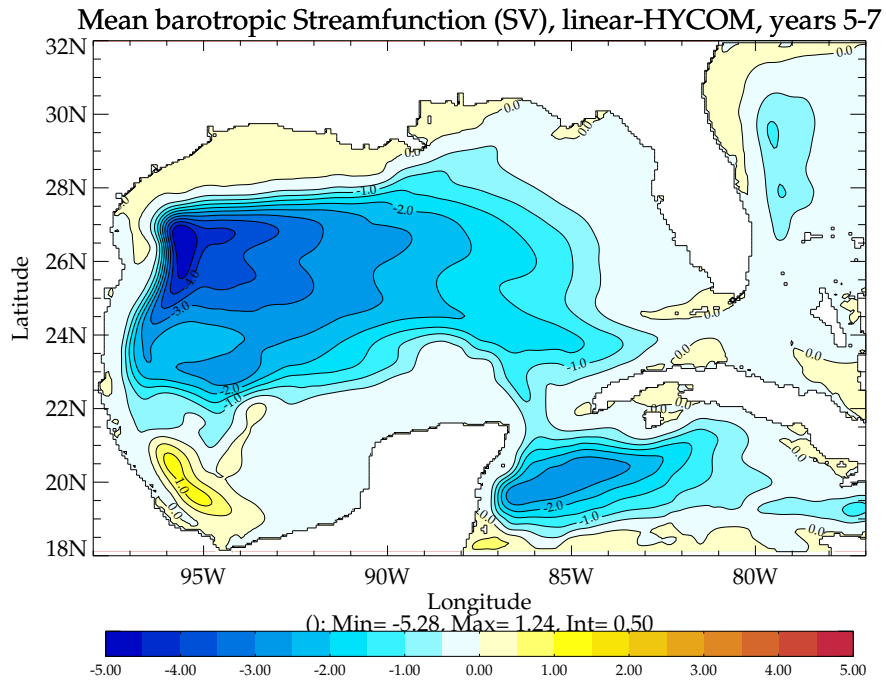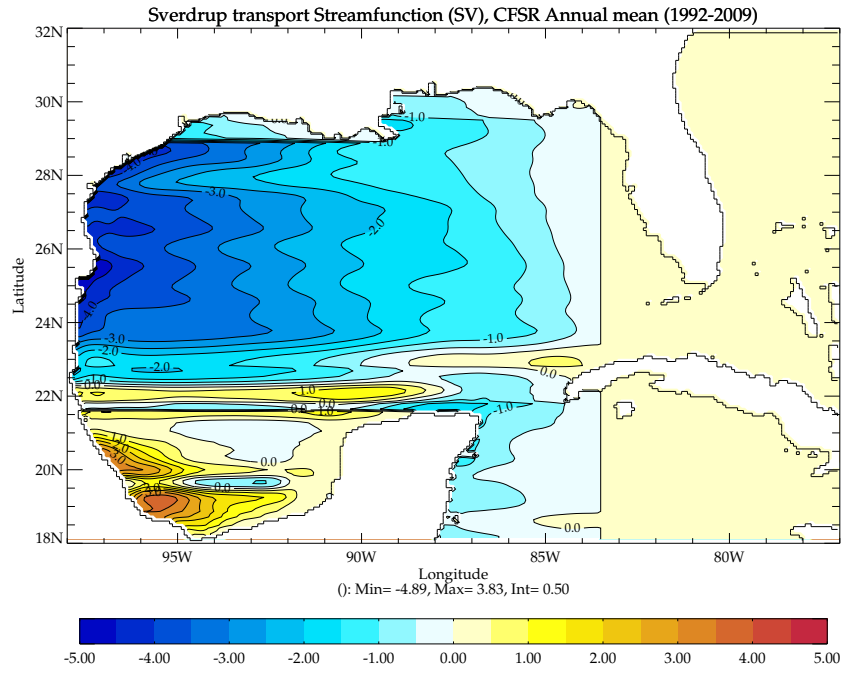
Figure 4.6: Sverdrup transport streamfunction (top) computed from annual wind stress curl (Fig. 1.2) and barotropic streamfunction (bottom) from the linear-HYCOM experiment averaged over the last 3 years of the simulation.

4.4 Contribution of different processes to the wind-driven circulation

In this section, the Sverdrup-like and wind-driven circulation in the absence of eddies is studied in order to infer the contribution of non-linearity in the momentum equations and variability in the wind forcing to the mean transport through the western boundary current in the GoM. First, following work done by Jaimes (2005), the hypothesis of Sturges and Blaha (1976) is investigated by computing the Sverdrup transport streamfunction in the GOM using the wind stress used to force the model, then the meridional transport across 26^oN is calculated to infer the return transport across the GOM-WBC. Then, this transport is compared with the transport in the model's WBC. To this end, a linear configuration of the model is made to run a linear version of the wind-driven experiment forced with the annual mean wind used to compute the Sverdrup transport (**HYCOM-lin** Table 2.2). The purpose is to provide a barotropic-equivalent response to wind stress forcing. Moreover, this linear experiment should be in good-agreement with the Sverdrup-like circulation obtained from previous studies (Sturges and Blaha, 1976; Sturges, 1993; Jaimes 2005). If we consider the Sverdrup theory alone, the WBC should represent the return flow for the meridional interior transport along a zonal distance to be determined (Sturges and Blaha, 1976). The Sverdrup balance is

$$\beta V = \frac{1}{\rho_0} (\nabla \times \tau) \tag{4.1}$$

where V is the meridional mass transport at any point in the ocean and $\beta = \frac{\partial f}{\partial y}$. So there is a function $\psi(x, y)$ such that

$$U = \frac{\partial \psi}{\partial y}, \qquad V = -\frac{\partial \psi}{\partial x}, \tag{4.2}$$

Then, if we integrate equation 4.1 in the x direction using 4.2, we get the total meridional transport at point x

$$\psi = \psi_0 - \frac{1}{\beta \rho_0} \int_{x=W}^{x} \left(\frac{\partial \tau^y}{\partial x} - \frac{\partial \tau^x}{\partial y} \right) \tag{4.3}$$

47
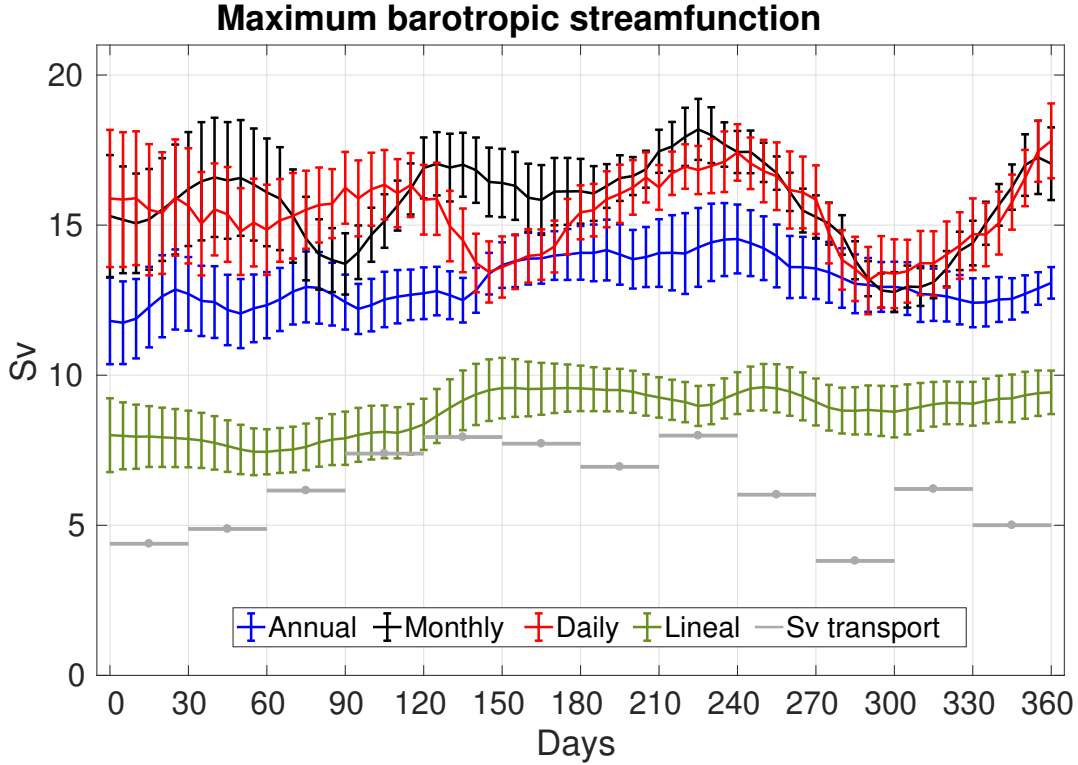
Figure 4.7: Time series of mean maximum barotropic streamfunction for the HYCOM-GOM-A (blue), HYCOM-GOM-M (black), HYCOM-GOM-D (red) and HYCOM-Lin (green) experiments. Also, monthly estimates of the Sverdrup transport streamfunction derived from the monthly climatology of wind stress is shown (gray horizontal lines). Vertical lines represent the standard error.

where $\psi_0 = 0$ and $x = W$ is the east boundary. So the Sverdrup transport streamfunction is:

$$\psi = -\frac{1}{\beta \rho_0} \left(\frac{\partial \tau^y}{\partial x} - \frac{\partial \tau^x}{\partial y} \right) (x - W) \tag{4.4}$$

Figure 4.6 (top) shows the Sverdrup transport streamfunction computed using the above equation. The wind used to compute the wind stress curl (Fig. 1.2 bottom) is the same used to force the model. This is how a purely wind-driven barotropic circulation may look like if the model is run with a steady wind, in the absence of dissipation, nonlinear interactions, and other forcing. Therefore, it is natural to compare with the WBC return transport of the mean barotropic streamfunction (Fig. 4.6 bottom) of experiment HYCOM-lin described in section 2.1. Two integrations

of the Sverdrup transport streamfunction were conducted, one starting at the east boundary of the domain (77^oW) and the other at 83^oW, but the resulting difference in transport is not significant so we present only the results from the latter since starting at this longitude is more realistic because it takes into account only the wind acting within the gulf; in both cases the integration stopped at the western boundary of the basin. The figure shows two main wind-driven gyres, one anticyclonic in the north and the other cyclonic in the south. The mean maximum transport found in the anticyclone is ~ 5 Sv. Since 4.4 is only valid in the interior away from the WBC, we compute the meridional transport at 26^oN and across $\sim 96 - 83^o$N.

Figure 4.6 (bottom) shows the mean barotropic streamfunction from the HYCOM-lin experiment. As expected, the main difference between Figures 4.6 top and bottom is the returning flow along the WBC before rejoining the interior in the mean barotropic flow in the model. Since the model is configured to be linear and also the boundaries are closed (no LC) in order to mimic the Sverdrup circulation, we expect the difference between the figures to be as minimal as possible except for this region. The Sverdrup circulation in the model produces a mean maximum transport of ~ 5.3 Sv. Both results are very close to the mean transport of 5 Sv reported by Sturges (1993), using a compilation of ship drift wind data and integrating from 98-90°W at 24°.

Another way to examine the variability of the wind-driven circulation in the western Gulf is using time series of mean maximum negative transport of the barotropic streamfunction along the western boundary current. From Figure 4.5, it is observed that the maximum anticyclonic flow (in dark blue) is always located along the western boundary specifically between 24° and 26^oN. It is therefore a reasonable indicator of variability. In Figure 4.7, the time series of mean maximum barotropic streamfunction for experiments HYCOM-lin (green line), HYCOM-GOM-D (red line), HYCOM-GOM-M (black line) and HYCOM-GOM-A (blue line), along with monthly estimates of the Sverdrup transport streamfunction computed using the monthly climatology of wind stress (gray horizontals line) is shown. The vertical bars represent the standard error, which is defined as the Standard Deviation (s) divided by the root square of the total number of data (n). It is observed a marked seasonality with a mean peak in August and a secondary peak in late December for the monthly and daily wind-driven experiments. On the other hand, as expected, the annual wind-driven experiment does not show any sign of seasonality.

Figure 4.8: Circulation index of the OBW-12 (red), OBNoW-12 (blue) and HYCOM-GOM-D (black) experiments for the NW (top panel), CW (middle panel) and SW (bottom panel) regions. For visualization purposes, the period of time shown is for three years, 1996-1999.

Our approach to estimate the contribution of non-linearity and variability in the wind to total mean transport is done by computing the average of the mean maximum negative transport in the western boundary current for each time series. The mean HYCOM-lin maximum transport is 8.5 Sv while the mean for the Sverdrup streamfunction is 7.5 Sv. A t-test performed to the means yielded that the difference in means is not significantly different from zero. Therefore, this result gives us confidence to conclude that the linear configuration of HYCOM-GOM is able to mimic, to some extent, the strength of the flow field imposed by the wind stress forcing over the deep GOM. From the same figure it can be seen that the BB86-GOM-A experiment can cause a mean maximum transport of ~ 15.5 Sv, about ~ 7 Sv larger on average than the HYCOM-lin (lines green and blue Fig. 4.7 bottom). The mean transport from experiments BB86-GOM-M and BB86-GOM-D is ~ 17.5 Sv for each one, so about ~ 2 Sv larger on average than the the HYCOM-GOM-A experiment. These results of the differences in mean transports help us to infer that the Sverdrup/linear contribution accounts for $\sim 40\%$ of total transport, around $\sim 40\%$ can be attributed to nonlinear effects, and variability imposed in the wind forcing can accounts for $\sim 20\%$. On the other hand, one noticeable difference in the pattern between the Sverdrup streamfunction and the barotropic streamfunction in Figure 4.6 is the slight asymmetry in the HYCOM-lin experiment that causes a shift of the strongest western boundary flow to the north-west (26.5^oN), meanwhile the Sverdrup streamfunction's strongest flow is around 25.5^oN. According to theory, asymmetry is mainly caused by non-linearity, therefore this behaviour could only be caused by nonlinear terms present in the continuity/thickness equation.

4.5   Eddy versus wind-driven circulation in the western GoM

Although the dominant synoptic-scale flow features described in section 4.3 persist from year to year, the monthly and daily wind-forced simulations show some seasonal and interannual variability on their circulation. We use a measure of circulation to evaluate this variability and the relative importance of the wind and the eddy-driven circulation in different regions of the western GoM. If it is assumed that the GoM is a two-layer system with the upper layer within the upper 1000 m (Perez-Brunius et al., 2013) we can compute the depth-averaged area-integrated relative vorticity of this upper layer, since it is know that eddies and Sverdrup-like circulation commonly extend over this depth, we call this measure the Circulation Index (CI).
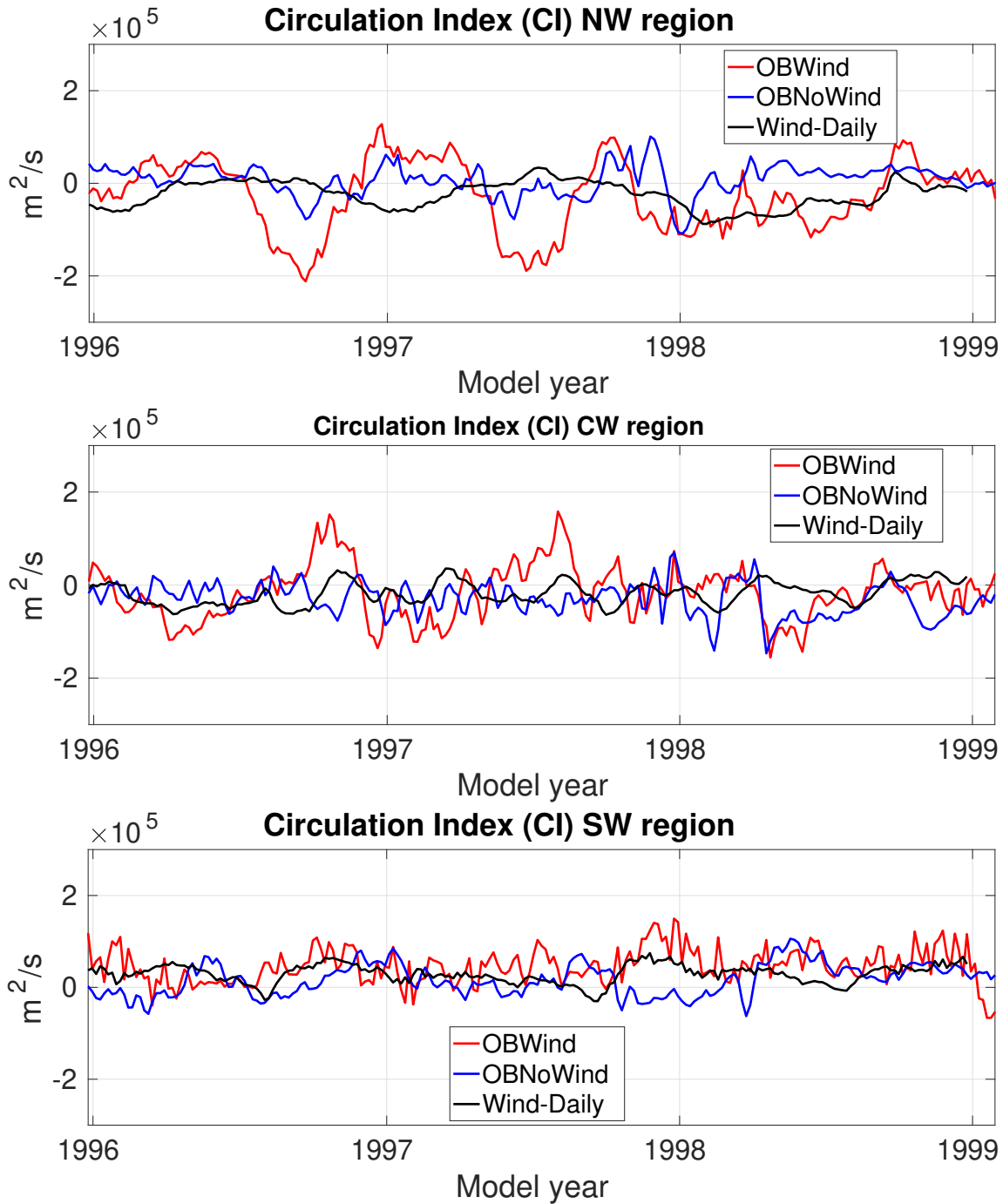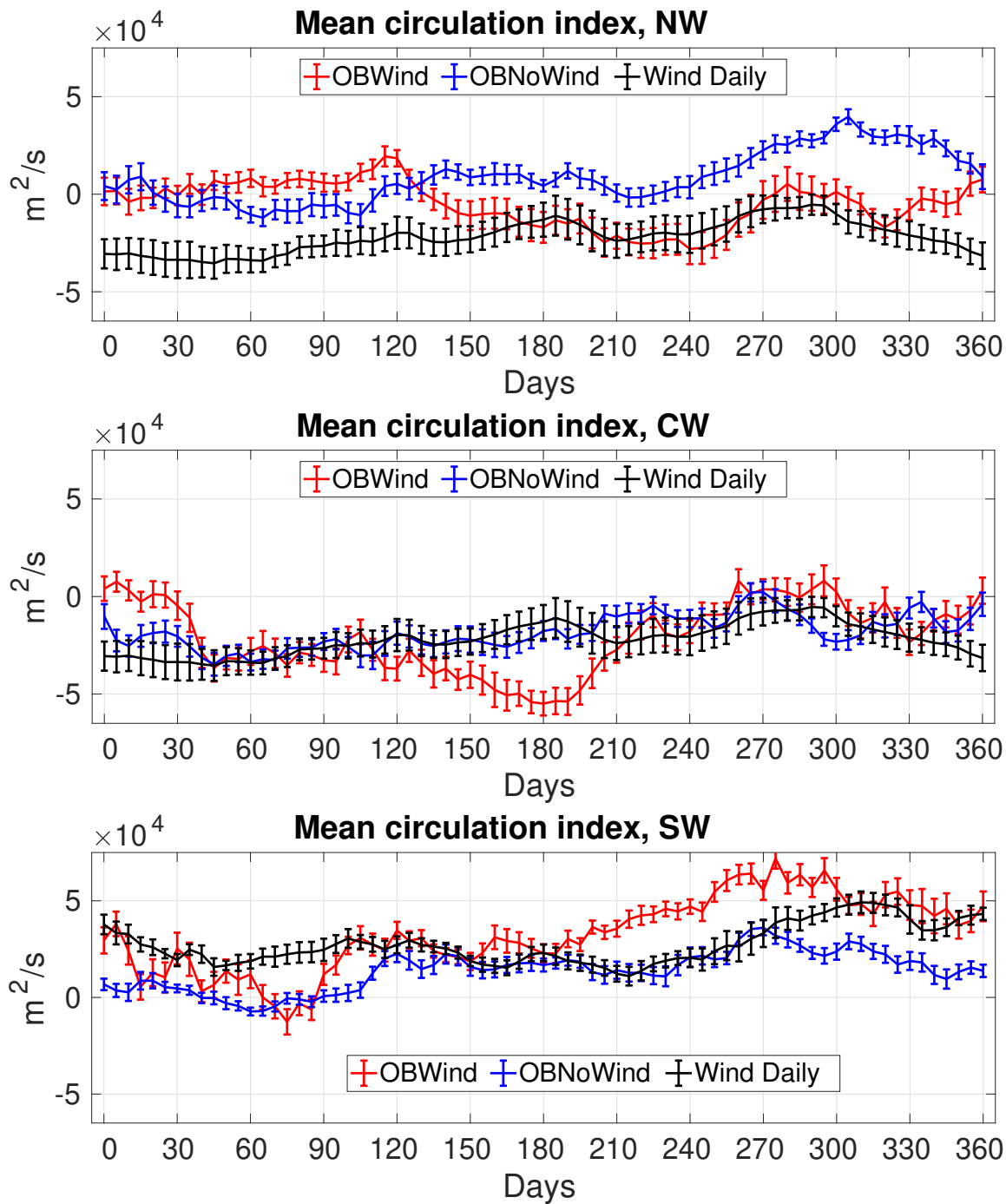
Figure 4.9: Mean circulation index of the OBW-12 (red), OBNoW-12 (blue) and HYCOM-GOM-D (black) experiments experiments for the NW (top panel), CW (middle panel) and SW (bottom panel) regions. Vertical bars represent the standard error.

According to the Stokes' theorem, the circulation, Γ, defined by the line integral of the velocity field around a closed curve C, can be computed from the area integral of the vorticity over the area enclosed by the curve as:

$$\Gamma \equiv \int_C \mathbf{u} \cdot ds = \int_A (\triangledown \times \mathbf{u}) \cdot dA \tag{4.5}$$

As mentioned above, for the purpose of studying the relative contribution of the wind and eddy-driven circulation, the western basin is divided in three sub-regions: north-western (NW), central-western (CW) and south-western (SW) (dashed lines Fig. 4.10 top). Figure 4.8 shows the time series of CI of the HYCOM-GOM configuration for the OBW-12, OBNoW-12 and HYCOM-GOM-D experiments in red, blue and black lines respectively, and the three regions, for only three years of the entire simulations (1996-1998). The time series show no obvious seasonal cycle. The mean and standard deviation of each time series are shown in Table 4.1. Focusing first on the NW region, it is observed that both experiments OBW-12 and HYCOM-GOM-D produce an anticyclonic circulation on average, however HYCOM-GOM-D generates a stronger anticyclonic circulation with means CI $= -0.5 \times 10^4$ m^2/s and $= -2.1 \times 10^4$ m^2/s respectively, while for experiment OBNoW-12, the mean CI is $= 0.8 \times 10^4$ m^2/s meaning that the average circulation is cyclonic. Secondly, on the CW region, all the three experiments produce an anticyclonic circulation (negative CI mean), something which is expected since it is observed on the horizontal maps of time-averaged velocity and SSH, however, the CI also switch to positive values several times throughout the simulation. Finally, in the SW region, all experiments produce a cyclonic circulation on average (positive CI mean) verifying the presence of the quasi-permanent gyre in the western BOC, a result also expected, however the region depicts smaller amplitude in the CI compared to the CW and NW regions in both configurations, which is reflected in the standard deviation values (table 4.1).

Figure 4.9 shows the long-term mean CI of the same experiments shown in Figure 4.8 with standard error vertical lines. It is observed that in the NW region, the eddy-driven circulation (experiment OBNoW-12) is able to produce a cyclonic (positive CI) circulation the second half of the year. One possible mechanism to explain this could be that when LCEs collapse against the western boundary of the CW sub-region, they would be able to produce a cyclonic circulation in the NW sub-region by means of a northward transference of angular momentum, the same argument
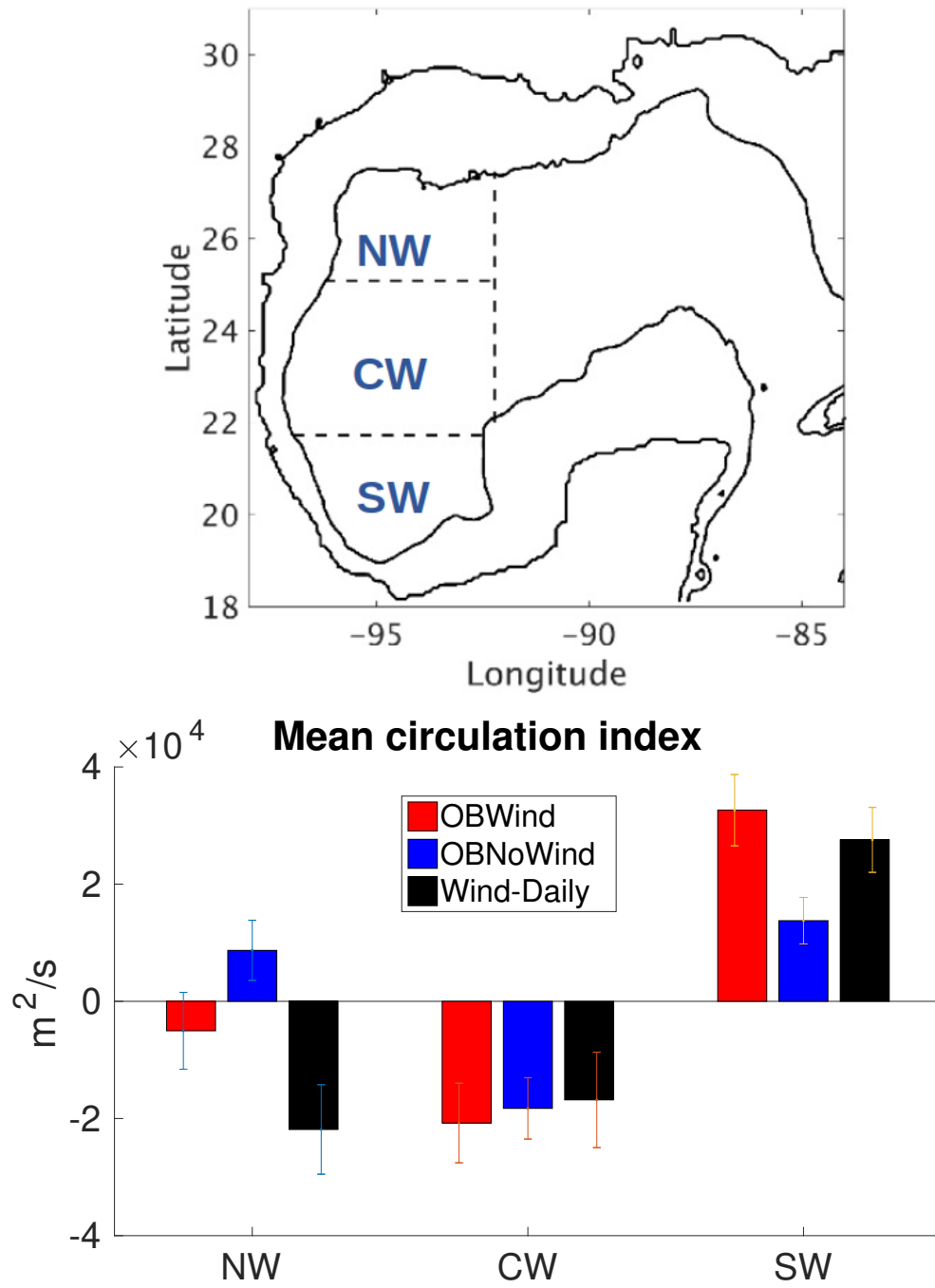
Figure 4.10: The three western subregions NW, CW and SW enclosed by the 1000 m isobath (inner contour) and the dashed lines (top). Mean circulation index bar chart for the three subregions.

used by Romanou et al. (2004) to explained the strengthen of the cyclonic circulation in the BOC, which in our study falls within the SW region.

A more illustrative way to explain the average contribution of wind and eddy-driven circulation in the western GoM is using a bar chart of the mean CI values for each western sub-region (Fig. 4.10 bottom), where a positive value means cyclonic flow and a negative value represent anticyclonic flow. From Figure 4.10 (bottom) it can be seen that in the NW sub-region the win-driven flow (exp. HYCOM-GOM-D, black bar) is anticyclonic on average, but in contrast, as explained above, the eddy-driven flow (exp. OBNoW-12, blue bar) is cyclonic. On the other hand, both forcings (experiment OBW-12, red bar) are able to produce a comparatively weaker mean anticyclonic vorticity in the NW region. Now, if the western GoM circulation can be seen as an eddy-induced flow superimposed over the wind driven circulation, it could be said that in the NW region wind-driven flow is anticyclonic on average, but eddies tend reduce this anticyclonic flow. Regarding the CW sub-region, both wind (exp. HYCOM-GOM-D, black bar) and eddy-induced (exp. OBNoW-12, blue bar) flows are anticyclonic on average in this region, and using the same analogy as above, it could be said that eddies tend to strengthen the anticyclonic circulation as seen in the more negative value of the mean CI of experiment OBW-12 (red bar). Finally, in the SW sub-region, both average wind (exp. HYCOM-GOM-D, black bar) and eddy-driven (exp. OBNoW-12, blue bar) circulations induce a cyclonic flow, but eddies enhance it as seen in the more positive value of the mean CI of experiment OBW-12 (red bar).

Examination of the mean barotropic flow can also give us some insight on the type of flow being set by either the wind or another process like eddy-topography interaction or topographic confinement. Figure 4.11 shows the mean barotropic streamfunction for experiments OBW-12 (top) and OBNoW-12 (bottom) averaged over the first 19 years of each simulation. The dark blue area enclosing the LC, representing anticyclonic flow, has transports higher than 10 Sv, however since the focus is on the western Gulf, color limits are chosen such that it highlights the western region. Results suggest that the intensification of the wind-driven flow producing the wide anticyclonic signature in the northwestern gulf is mainly barotropic. The deep cyclonic gyre on the Sigsbee Plain, named the Sigsbee Abysssal Gyre (SAG), recently suggested to be driven by eddy-topography interaction via bottom form stresses (Perez-Brunius et al., 2018) shows stronger barotropic flow in the experiment OBW-12. On the other hand, the cyclonic circulation in the BOC centered at
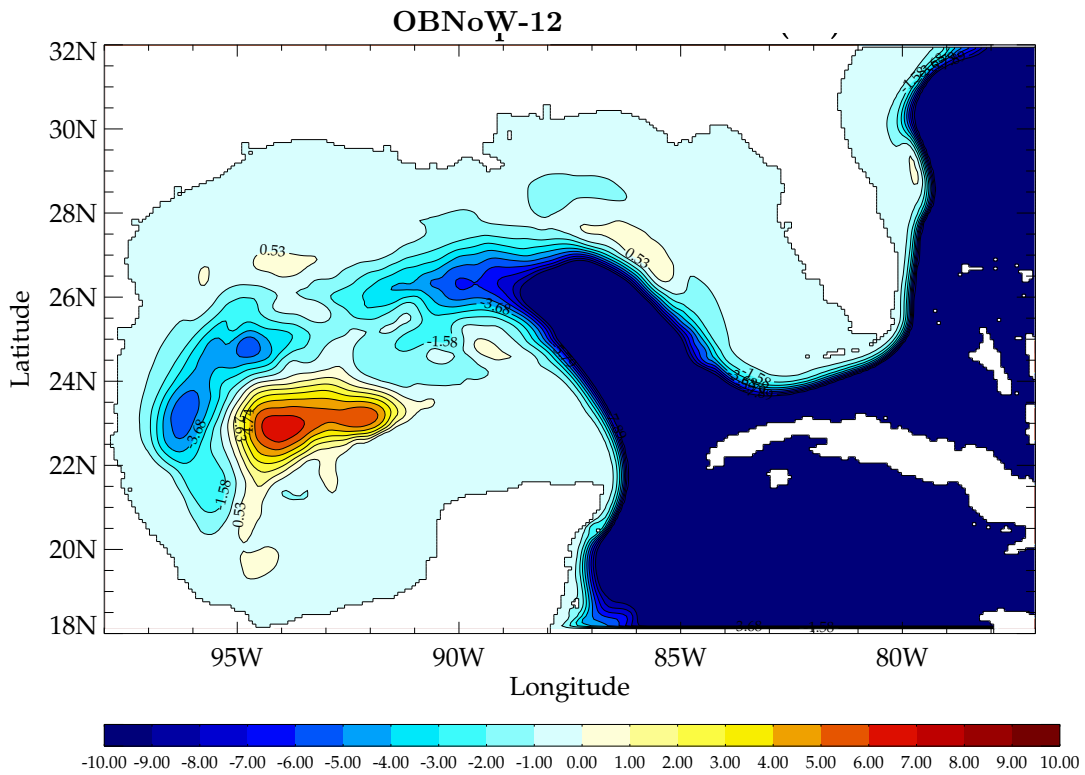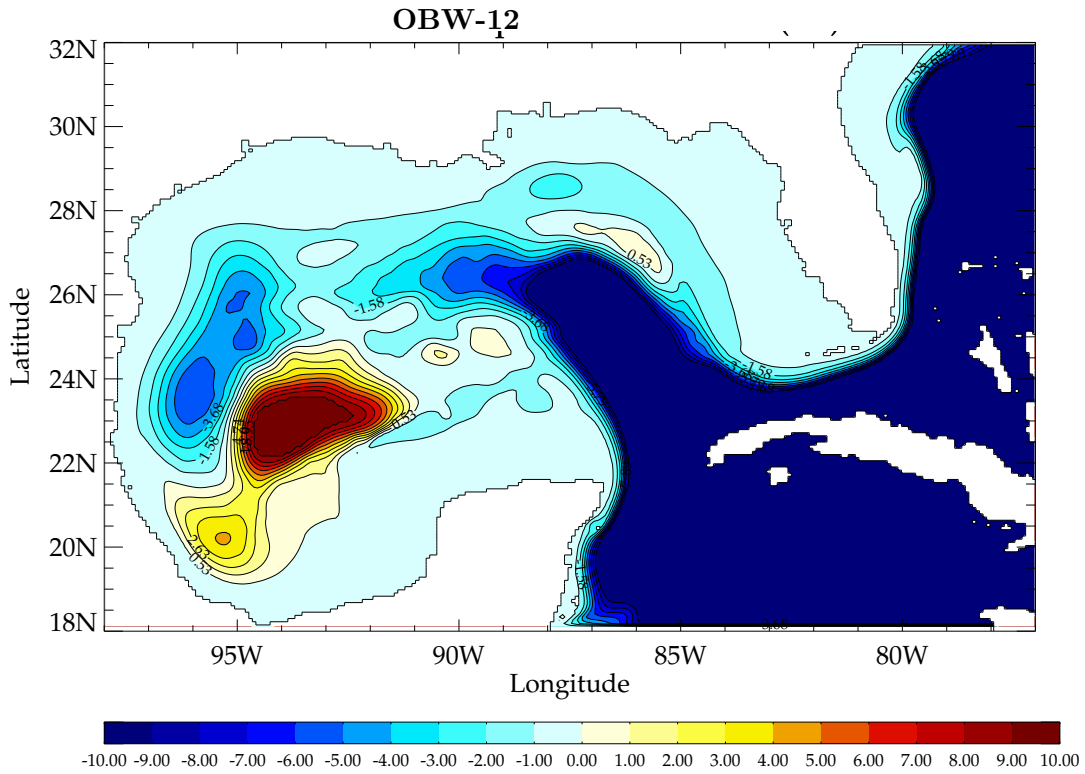
Figure 4.11: Mean barotropic streamfunction averaged over the first 19 years of experiments OBW-12 (top) and OBNoW-12 (bottom). Colorbar limits (Sv) are set so circulation in the western Gulf is highlighted.

56

Table 4.1: Mean and standard deviation (in parentheses) of the circulation index per region ($\times 10^4$ m^2/s) for the OBW-12, OBNoW-12 and HYCOM-GOM-D experiments.

	OBW-12	OBNoW-12	HYCOM-GOM-D
NW	-0.5(5.6)	0.8(4.4)	-2.2(2.4)
CW	-2.0(5.8)	-1.8(4.5)	-1.7(2.6)
SW	3.2(52)	1.3(3.4)	2.8(1.7)

around 95.3^{o}W, 20°N, is depicted in Figure 4.11 top, with a maximum barotropic transport of ~ 4 Sv, while in experiment OBNoW-12 there is no signal of such cyclone. The above suggests that the response of the flow to the wind is mainly barotropic. Now, the fact that the mean barotropic streamfunction does not show a clear signature of a cyclonic flow in the BOC for the OBNoW-12 experiment while in the time-averaged SSH horizontal map (Fig. 3.4 b) is clearly seen, suggests that the type of circulation set by the processes other than wind, like eddy-topography interaction or topographic confinement, could be mainly baroclinic.

4.6   Summary and discussion

The set of closed-boundaries wind-driven experiments in the GoM using the BB86 and the HYCOM configurations prescribed with different wind forcing variability including an experiment using a linear configuration of the model, as well as an estimate of the Sverdrup transport were intended firstly to provide a way to understand the wind-driven circulation by partitioning it in different factors that contribute to the total mean transport. We used the time series of maximum barotropic streamfunction from the experiments described above and monthly estimates of the Sverdrup transport to address this question. Results show that the Sverdrup/lineal mean transport accounts for $\sim 40\%$ of the total flow on average, non-linearity present in the momentum equations account for $\sim 40\%$ of the mean transport, and finally, the transport induced by the variability imposed in the wind forcing contributes to the remaining $\sim 20\%$.

The time-averaged surface velocity and SSH depicts similar features among the experiments, a broad anticyclonic gyre in the northwestern Gulf which is western intensified, and a cyclonic gyre in the western BOC. It was found that the absence of a mixed layer model in the BB86-GOM configuration makes it more energetic, compared to the HYCOM-GOM configuration, due

to the lack of a more effective dissipation mechanism. The Sverdrup transport streamfunction computed from the annual wind stress curl and the barotropic streamfunction computed from a linear configuration of HYCOM-GOM show similar results as far as maximum transport, in the order of 5 Sv, which is also in good agreement with previous published results like Sturges (1993).

The Circulation Index computed using the diabatic experiments from the previous chapter, was used to infer mean contributions of the wind and eddies in the western GoM circulation. It was found that if the western GoM circulation can be thought as an eddy-induced flow superimposed over a wind-driven circulation, the former tends to modify the circulation differently according to each sub-region: in the NW region, the eddy and wind contributions are nearly additive, i.e., the mean cyclonic flow produced by the LCEs, presumably by means of a mechanism similar to which the LCEs strengthen the quasi-permanent cyclonic circulation in the BOC (Romanou et al., 2004), tends to reduce the strong mean anticyclonic flow induced by the wind, therefore producing a relatively weaker anticyclonic nonlinear circulation; in the CW region the mean anticyclonic circulation induced by the LCEs colliding against the western boundary tends to enhance the relatively weaker anticyclonic flow generated by the wind forcing, producing a stronger circulation; finally in the SW region, the relatively weaker cyclonic flow induced by the LCEs enhance the stronger cyclonic flow generated by the wind, producing a stronger cyclonic circulation.

Examination of the mean barotropic circulation allowed us to conclude that the quasi-permanent cyclonic circulation in the Bay of Campeche is the result of the mean contributions of a barotropic response to the wind and of a baroclinic eddy-induced circulation. This result is in good-agreement with the findings made by Perez-Brunius et al. (2013) about the partial contributions of the wind and LCEs in the BOC cyclonic flow, however, we consider that future numerical work is needed to confirm the role of topography in the circulation, the relationship of the LCEs traveling to the SW region and the intraseasonal variability of baroclinic currents in the BOC region, and the role the wind plays in the seasonality modulation of the cyclonic circulation.

CHAPTER 5

CONTRIBUTION OF WIND AND LCES TO THE CIRCULATION OF THE WESTERN GOM

5.1 Introduction

Our aim in this chapter is to provide new elements for a better understanding of the contribution of the LCEs and wind to the Gulf of Mexico circulation. As mentioned in section 1, it is still not completely clear over which time scales what mechanisms are more important than others in driving the circulation in the western GoM. To answer this, we examine the upper ocean dynamics over the western gulf to quantify the contribution from ocean processes and the atmosphere to the ocean vorticity budget. The focus is primarily on the upper thousand meters of the ocean, therefore the methodology is applied to the first 17 layers of the model (Table 2.1), with the average depth of the 17th layer interface being ~ 1000 m on the western GoM. The area of interest is divided in three subregions: north-western (NW), central-western (CW) and south-western (SW) regions, which are delimited by the dashed lines in Figure 4.10 (top) and the contour of the 1000 m isobath. This is done to obviate difficulties arising from isopycnal layers intersecting bottom topography. The choice of these three regions was made such that the eastern limit of the NW and CW regions was at least a LCE diameter (~ 300km) away from the average threshold for the LC to force the basin interior (see the western edge of the LC in Figure 3.4 a) and covered most of the center paths of LCEs described above as well as the paths described by Vukovich (2007), and the SW region enclosed most of the BoC and the cyclonic circulation described by Vazquez de la Cerda (2005).

Several authors have studied the surface vorticity balance in different water bodies. In particular, the balance used in this study is based upon the one presented in Boudra and Chassignet (1988) to study the dynamics of the Agulhas retroflection. The authors used a set of different models to determine the mechanisms governing the retroflection. Since the experiment using the quasi-isopycnic 2-layer model with the more realistic coastal geometry was the one that gave more insight, they concluded that planetary vorticity and viscosity are responsible for the change in vorticity next to Africa's east coast and planetary vorticity and advection of relative vorticity on the seaward side

of the current core. Murray et al. (2001) used a high-resolution six-layer numerical ocean model to examine the interannual variability of the upper ocean vorticity budget in the Gulf of Alaska. The authors show that the advection of vorticity in and out of the domain can be important for its balance in large time scales and relate the interannual variability of vorticity to the variability in the atmosphere and the advection due to coastal Kelvin waves entering the Gulf of Alaska. Souza et al. (2015) created a detailed description of the ocean surface vorticity around the Hawaiian Islands using model reanalysis generated using all the available observations. They found that the wind stress curl has a direct influence on the surface vorticity balance in the immediate lee of the islands while advection is the dominant term transporting the vorticity westward. Schoonover et al. (2016) examined the North Atlantic barotropic vorticity balance using numerical simulations conducted across different model platforms and resolutions. Their results on the barotropic component of the vorticity balance confirm that the subtropical gyre is characterized by a balance primarily between the applied wind stress curl and bottom pressure torque, meanwhile the area-integrated budget over the Gulf Stream showing that the northward return flow is balance by bottom pressure torque is robust across different models and resolutions. Regarding vorticity studies in the GoM, Candela et al. (2002) examined the potential vorticity flux between the GoM and the Caribbean Sea using time series of current and density measurements across the Yucatan Channel section. They found that LCE shedding is preceded by periods of positive vorticity influx into the GoM that causes a retraction of the current.

5.2   Vorticity balance of the upper ocean

Vorticity plays a central role in geophysical fluid dynamics, many ocean processes can be expressed through their contribution to the overall vorticity field and the interaction between the ocean and the atmosphere through the flux of vorticity in the interface. Therefore understanding the upper ocean vorticity balance in the GoM may gives us more insight on under which conditions the circulation is driven by a given process.

For the present study, the upper ocean vorticity balance equation is derived from the HYCOM general momentum equation (Wallcraft and Metzger, 2009), in a similar fashion to how Boudra and Chassignet (1988) did it with the Bleck and Boudra (1981) model (or simply the BB model), except that their term related to the vertical motion of the layer relative to the surface is not present in
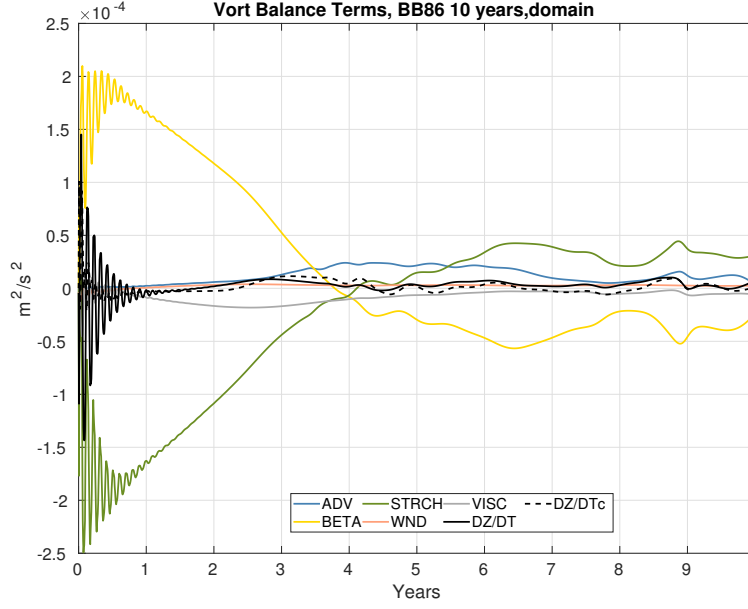
Figure 5.1: Area-integrated terms for BB86 experiment

the HYCOM formulation (see Appendix A for details on the the derivation of this equation). The momentum equation is then given by:

$$\frac{\partial \mathbf{v}}{\partial t} + \bigtriangledown \frac{\mathbf{v}^2}{2} + (\zeta + f)\mathbf{k} \times \mathbf{v} = - \bigtriangledown M + \alpha \frac{\partial \tau}{\partial p} + (\triangle p)^{-1} \bigtriangledown \cdot (\nu \triangle p \bigtriangledown \mathbf{v}) \qquad (5.1)$$

(See appendix A for description of variables and parameters.)

Taking the vertical component from the curl of 5.2 yields the differential form of the relative vorticity equation:

$$\frac{\partial \zeta}{\partial t} = - \underbrace{(u,v) \cdot \bigtriangledown \zeta}_{\text{Vorticity advection}} - \underbrace{v\beta}_{\text{Plan vort advection}} - \underbrace{(\zeta + f) \cdot \bigtriangledown \cdot \mathbf{v}}_{\text{Stretching}} +$$

$$\underbrace{\alpha \bigtriangledown \times \tau_z}_{\text{Wind stress curl}} + \underbrace{\bigtriangledown \times \{(\triangle p)^{-1} \bigtriangledown \cdot (\nu \triangle p \bigtriangledown \cdot \mathbf{v})\}}_{\text{Viscous stress curl}}$$

$$(5.2)$$

Where the left-hand side of the equation is the change of relative vorticity with time. The first

61

through fifth terms on the right-hand side are the contributions to the change in vorticity from advection of vorticity, advection of planetary vorticity, stretching of the water column, wind stress curl and viscous stress curl respectively. The Boudra and Chassignet (1988) solenoidal and tilting terms are neglected in our study because the Montgomery potential terms cancel when taking the curl of 5.2 and there is no vertical motion term as mentioned above. The methodology consists of three major steps. First, the analytical vorticity balance equation is discretized in space and time; second, gridded velocity, layer thickness and turbulent viscosity data are averaged over the upper 17 layers (average depth of 1000 m) and are used to calculate each term and construct horizontal maps and time series for each of the three western sub-regions showed in Figure 4.10 (top); finally, the vorticity balance terms are analyzed and visually inspected in ways conducive to revealing the relative importance of the different processes in the western Gulf. We expect that the results from the methodology described above will also give us some insight in the understanding of the physical mechanisms by which the wind and migrated LCEs sustain the western GoM. For simplification, the area-averaged (divided by total area) terms are defined as:

$$ADV = -\int_A (\mathbf{v} \cdot \bigtriangledown \zeta) dA \tag{5.3}$$

$$BETA = -\int_A (v\beta) dA \tag{5.4}$$

$$STRCH = -\int_A (\zeta + f) \cdot \bigtriangledown \cdot \mathbf{v} dA \tag{5.5}$$

$$WIND = \int_A (\alpha \bigtriangledown \times \tau_z) dA \tag{5.6}$$

$$VISC = \int_A \bigtriangledown \times \{(\triangle p)^{-1} \bigtriangledown \cdot (\nu \triangle p \bigtriangledown \mathbf{v})\} dA \tag{5.7}$$

$$DZETA = ADV + BETA + STRCH + WIND + VISC \tag{5.8}$$

$$DZETAc = \int_A (\frac{\partial \zeta}{\partial t}) dA \tag{5.9}$$

It is important to mention that the DZETAc term is the rate of change in vorticity calculated using the velocity field directly from the model output. The respective time series for DZETAc is then
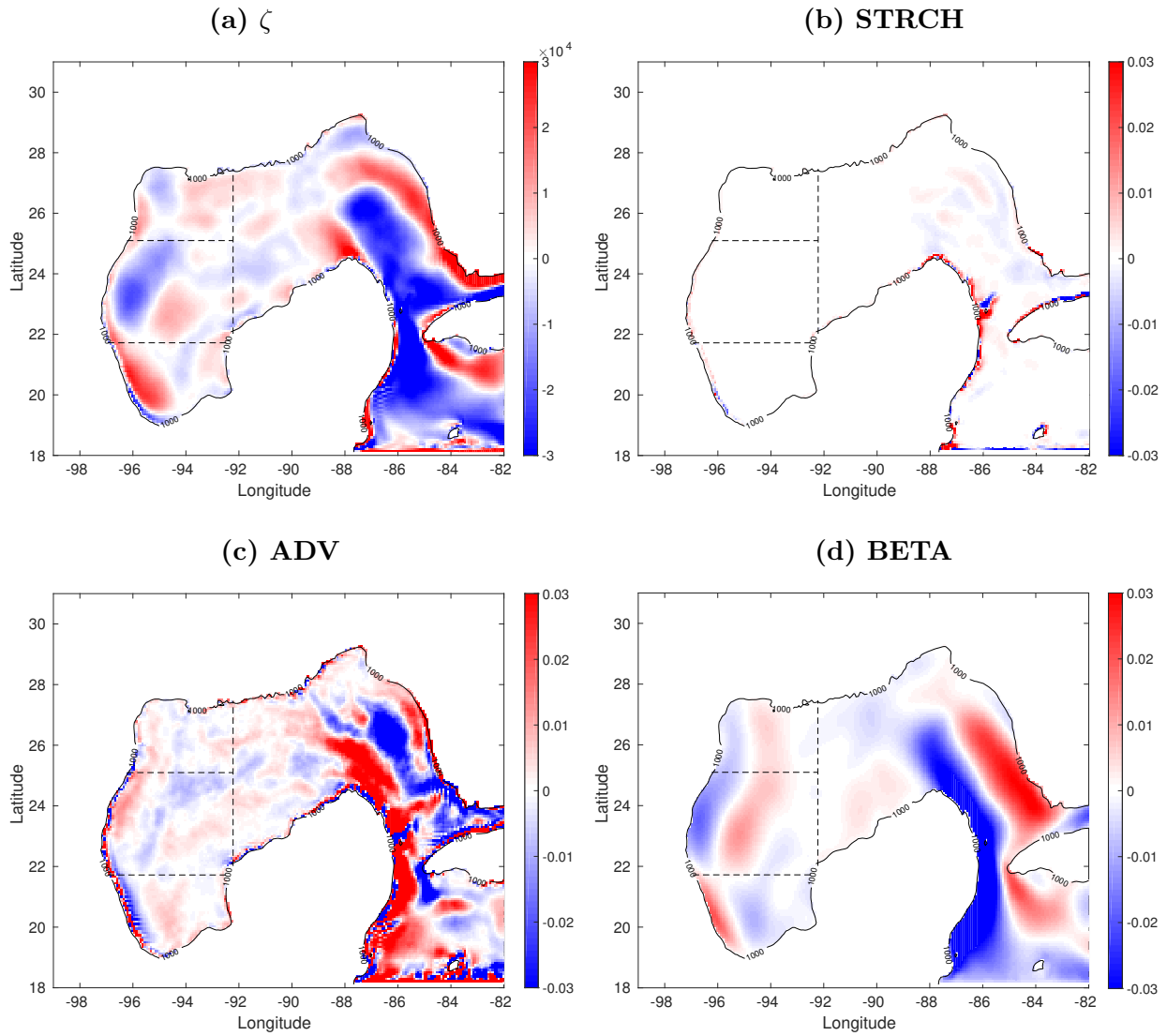
Figure 5.2: Mean maps of (a) upper thousand meters ocean vorticity (x 10^{10} s^{-1}) derived from model results; (b) change in vorticity (x 10^{10} s^{-2}); (c) advection of vorticity and (d) planetary vorticity advection. Black contour represent the 1000 m isobath and dashed lines the division of the NW, CW and SW regions.

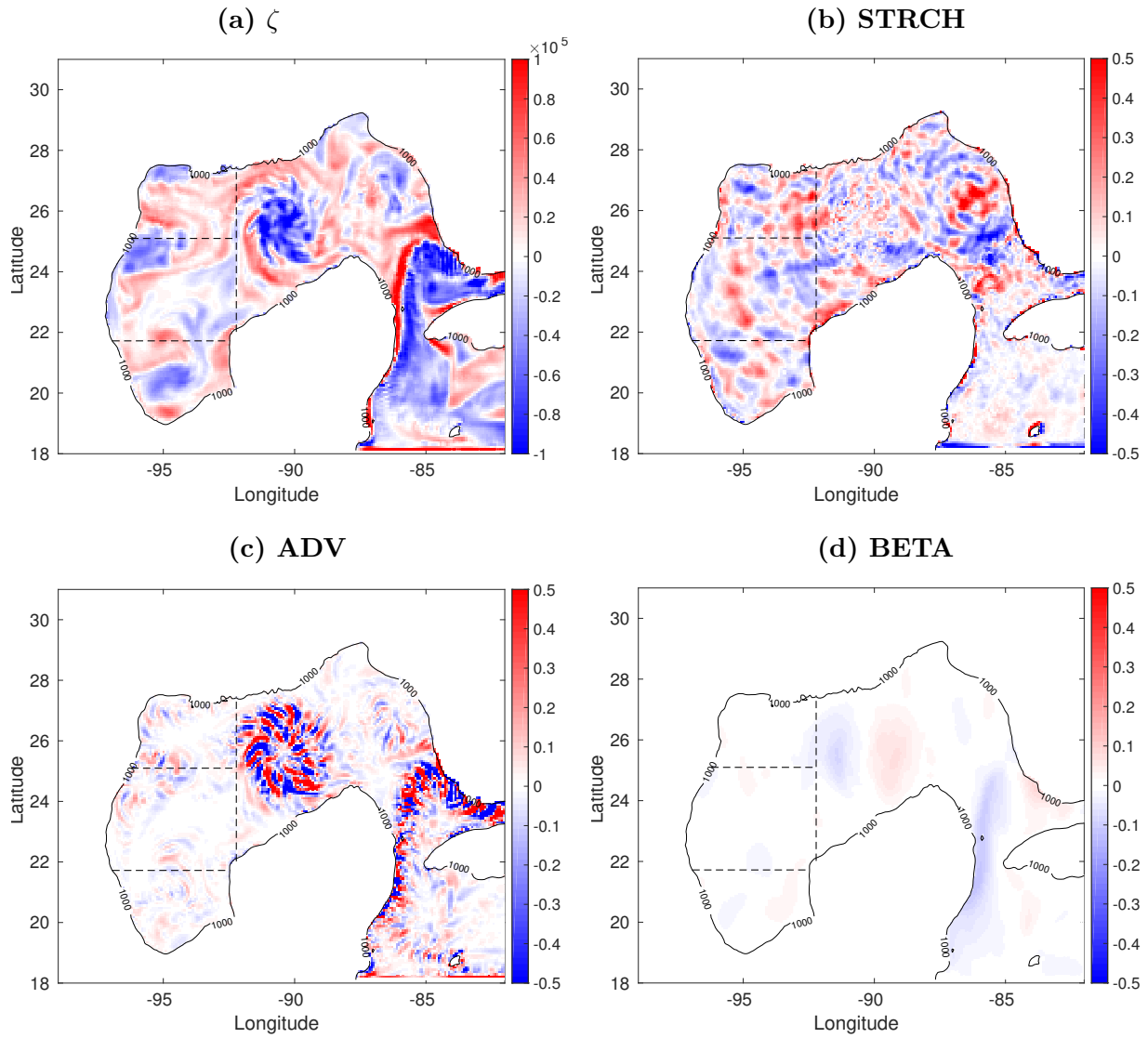Figure 5.3: Maps of instantaneous (a) upper thousand meters ocean vorticity (x 10^{10} s^{-1}) derived from model results; (b) stretching; (c) advection of vorticity and (d) planetary vorticity advection for the 10th of July 1992. Black contour represent the 1000 m isobath and dashed lines the division of the NW, CW and SW regions.

compared with DZETA, the sum of all the terms, in order to verify that the computation of the vorticity balance is accurate. The finite difference form of 5.2 is:

$$\frac{\partial \zeta}{\partial t} = -\overline{\overline{u}^{xy}\delta_x\zeta}^x - \overline{\overline{v}^{xy}\delta_y\zeta}^y - \overline{\overline{u}^{xy}\delta_xf}^x - \overline{\overline{v}^{xy}\delta_yf}^y - (\zeta + f)\overline{\delta_xu + \delta_yv}^{xy}$$

(5.10)

$$+ \alpha(\delta_x\{(\overline{\delta p}^y)^{-1}\tau_y\} - \delta_y\{(\overline{\delta p}^x)^{-1}\tau_x\}) + \nu(\delta x\{\delta_x^2v + \delta_y^2v\} - \delta y\{\delta_x^2u + \delta_y^2u\})$$

where the $\delta_\Delta($ $)$ operator is the difference between ( ) at neighboring grid points divided by the Δ-direction grid distance. Similarly, $\overline{()}$ is an average of ( ) over consecutive grid points.

5.3 Vorticity balance in the western GoM

To examine the vorticity balance in the GoM, the first cycle (first 19 years) of experiment OBW-12 (chapter 2) is used since it is the simulation which includes the wind and lateral forcings and therefore the most realistic of all the experiments. The time-averaged ocean vorticity of the upper ~1000 m derived from the respective simulation is shown in Figure 5.2(a). Focusing on the western Gulf, a region of strong anticyclonic (negative values in blue) vorticity centered at 96^oW and 23^oN dominates, being consistent with the mean circulation on the western boundary of Figure 3.4 (a) and with the region where most of the LCEs dissipated (figure of LCs paths). The cyclonic vorticity maximum in the western BOC is also consistent with the quasi-permanent cyclonic circulation mentioned formerly. A secondary maximum of cyclonic vorticity is observed next to the anticyclonic maximum. Our results suggest that this secondary maximum may be the result of two processes, one is the barotropic signature of the SAG (Perez-Brunius et al., 2018), seen in the barotropic streamfunctions (Fig. 4.11), and the other process is the interaction of LCE with cyclones formed directly to its north, which eventually travel clockwise surrounding the LCE and with a final fate around this region (Frolov et al., 2004).

The horizontal maps of the vorticity balance STRCH, ADV and BETA terms averaged over the 19-year period are shown in Figures 5.2 b-d. The average contribution of advection (Fig. 5.2 c) reveals paths of advected anticyclonic and cyclonic vorticity (blue and red respectively) through the CW and NW regions, presumably responsible for the anticyclonic maximum and part of the secondary cyclonic maximum shown in Figure 5.2 a. Also, the SW region shows an area of advection

of cyclonic vorticity that could be responsible in part for the cyclonic maximum over that region. Similarly, the advection of planetary vorticity (Fig. 5.2 d) seems to be responsible for conveying part of the anticyclonic vorticity carried by LCEs once they reach the western boundary (around 96.5^{o}W and confined mainly within the CW and NW regions) northwards and part of the cyclonic vorticity carried by the cyclones formed to the north of LCEs once they reach the western boundary (around 95°W within the CW and NW regions) southwards. Being a second-order derivative, the vorticity gradient field present in the ADV term is highly sensitive to noise, producing a noisier ADV field, which can be seen in Figure 5.2 c while the planetary vorticity advection term, a first order derivative, presents a smoother pattern (Fig. 5.2 d). However, it is somewhat noticeable that this meridionally-oriented bands of positive and negative BETA on the western gulf are balanced partially by ADV, which is reasonable given the fact that these two terms are also highly balanced over the LC region. The mean map of STRCH is also shown (b), although it can be seen that the mean contribution of this term to the mean vorticity field is negligible compared with ADV and BETA, we will later show that the instantaneous contribution is significantly higher. Our results indicate that the contribution from the wind stress curl and viscous stress curl to the mean vorticity field is negligible, therefore we don't present such maps. The presence of a well-organized (mean) circulation indicates that the dominant contribution to mean vorticity is the advection of vorticity and planetary vorticity advection.

On the other hand, since the GOM also presents strong short-term structures, the mean circulation may not describe the highly variable vorticity balance of the upper ocean. While the contribution of the advection of vorticity and planetary vorticity advection remain permanently over regions of strong currents like the LC or LCEs, inspection of instantaneous maps shows that the stretching term is also highly variable and probably associated to inertial currents produced by wind and small-scale eddies. Consequently, in Figures 5.3 a-d, we show the instantaneous maps of vorticity, STRCH, ADV and BETA respectively for the 10th of July 1992, when a LCE was approaching the western gulf. It is clear that ADV and BETA have high values in the LCE area, but it is not so clear for STRCH. Instead, the instantaneous STRCH field depicts a highly variable pattern, which is noisier in the LCE region. Figure 5.4 shows terms in eqs. 5.3-5.8 of a given month for the three sub-regions. The presence of high-frequency (possibly inertial) oscillations on the change of vorticity term DZETA (continuous black line) indicates that the dominant contri-
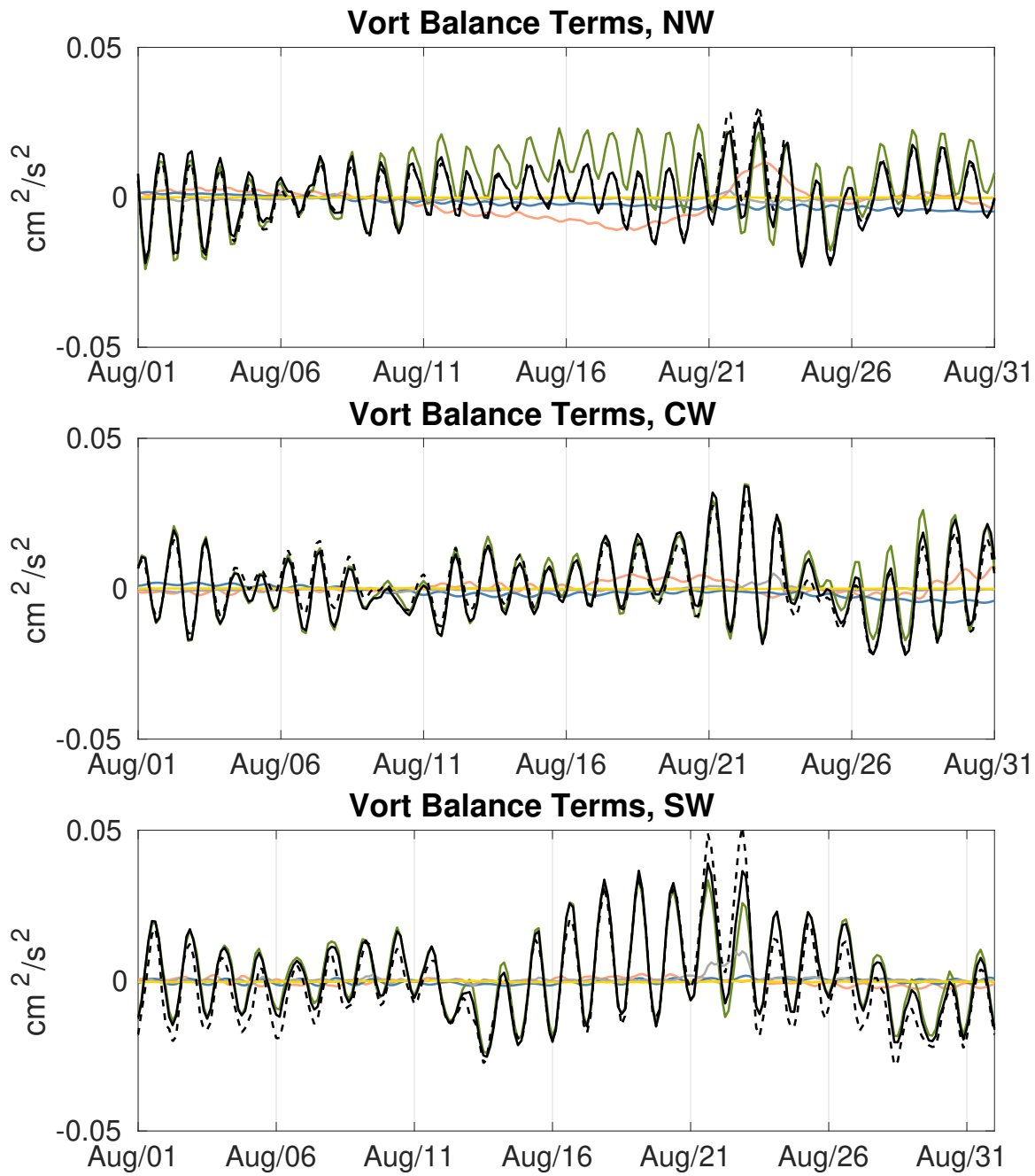
66

Figure 5.4: Area-averaged terms for August 1996, expt OBW-12.

bution to vorticity is stretching (green line) in short time-scales. Figure 5.5 shows the time series for the same period of time but with a 1-day low pass filter applied. The figure indicates that at subinertial time scales, the contribution of another terms becomes more evident. Such is the case of ADV, which seems to compensate STRCH in the NW region (top) for a period of approximately 2 weeks. Another case is when the importance of the WIND term (gray line) becomes clearer in apparently atmospheric events, presumably cold fronts or hurricanes, like in the 22nd of August in the SW region. From the figure it can be seen that at the time of the "event", a bump in the gray line, the difference between DZ/DT and DZ/DTc becomes larger, suggesting that the wind input of vorticity is the responsible of this difference.

In order to look into longer time scales, a 30-day running mean filter was applied to the whole record of time series in the three sub-regions (Fig. 5.6). The figure shows that in the three sub-regions, the contribution of the STRCH (green line) is important, since is the term that depicts more amplitude and variability, specially in the SW. However, in the NW and CW regions BETA (blue line) also becomes important in some time periods, in fact it can be seen that for periods of ∼2-3 months length, BETA balances STRCH. Now the question arises as to what ocean process is responsible for such behaviour, specially because these events happen with apparently no periodicity. Our first hypotheses is that these events could be related to mesoscale features like LCEs. Therefore, if we focus on a single event in this case the one happening in late 1993, we should be able to infer more. Figure 5.7 shows the instantaneous horizontal maps of vorticity (ζ), BETA and STRCH terms for October 1993, when a LCE is entering the NW region, along with the time series of BETA and STRCH in which the vertical red line indicates the time in which the snapshots are shown. Also, the black thick contours show the 0.17 m contour representing the LCE and LC edge. It can be observed that when the eddy is entering the region, BETA becomes more negative and STRCH more positve, balancing each other, this is because the northward velocity in the region becomes stronger and the water column stretches produced by the convergence of the flow in the eddy.

To assess the importance of the different terms in the vorticity balance in short and long time-scales, a scale analysis was performed for the 3-hr (Fig. 5.4) and the low-pass filtered data (Fig. 5.5) for the whole 19-year simulation. The scale analysis consists of dividing each term by the sum of them i.e., DZETA (ζ_t) in order to obtain how much of the variation is explained by each term.
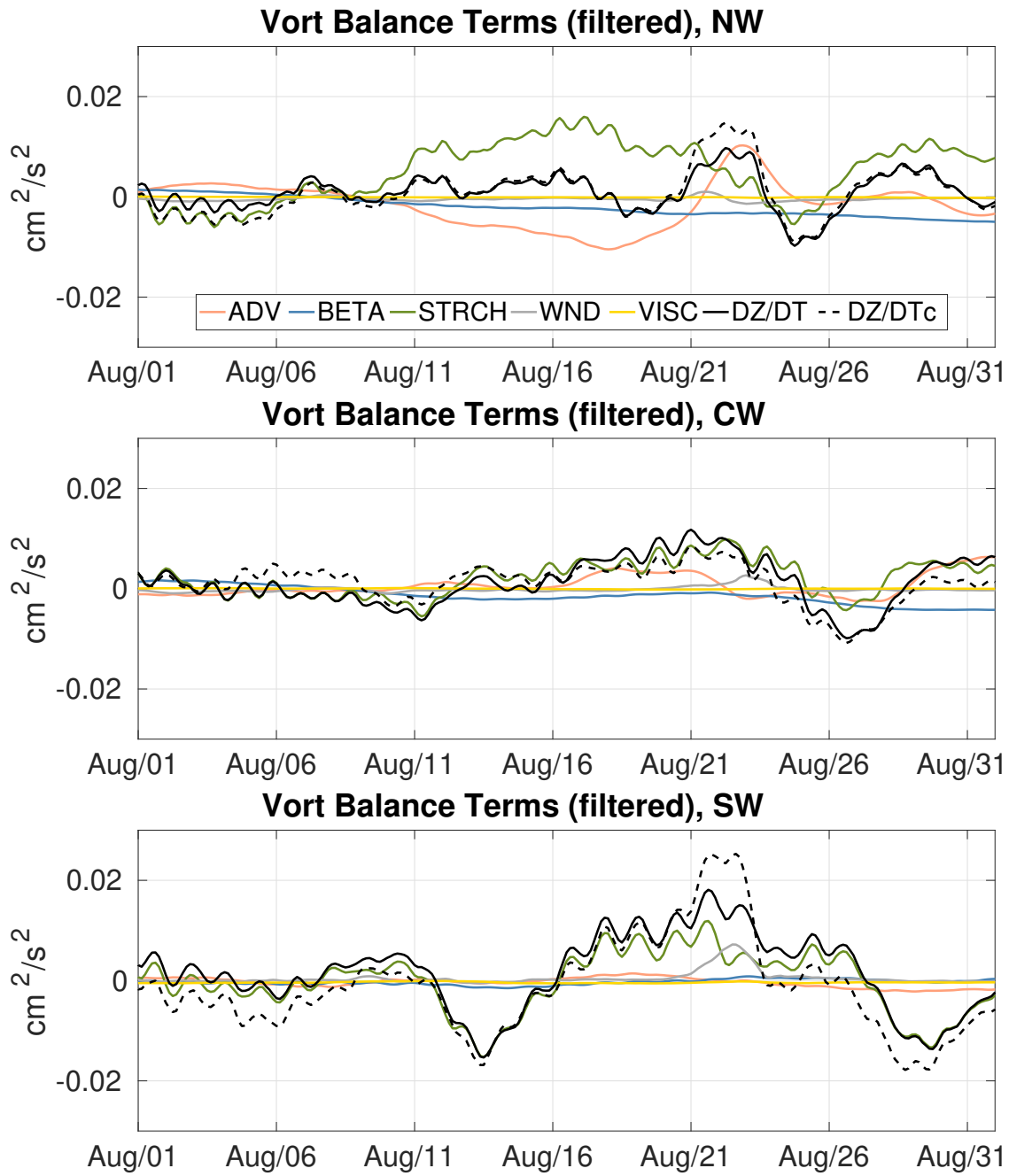
Figure 5.5: 1-day low-pass filtered area-averaged terms for August 1996, expt OBW-12.

Table 5.1: Correlation coefficients between DZ/DT and each of the balance terms.

Term	**ADV**	**BETA**	**STRCH**	**WIND**	**VISC**	**dz/dtc**
dz/dt NW	0.0398	0.0218	0.9614	-0.0384	-0.0042	0.9731
dz/dt CW	0.0025	-0.0037	0.9772	0.0740	-0.0379	0.9682
dz/dt SW	0.0380	0.3870	0.9853	0.1681	0.0525	0.9460

Table 5.2: dz/dt and dz/dtc mean.

Term	**NW**	**CW**	**SW**
dz/dt	3.19e-4	9.66e-4	6.8e-3
dz/dtc	1.16e-06	-5.73e-6	-4.97e-9

Figure 5.8 shows the Box Plots of the distribution of scaled terms for each sub-region for the 3-hr (left panels) and filtered time series (right panels) respectively. According to it, STRCH dominates the three sub-regions in short time scales since the mean value (red horizontal line in boxplot) is close to 1, ADV and BETA show secondary importance and WIND and VISC contributions to the vorticity balance are negligible. For longer time scales the behaviour is similar except for the NW region where BETA becomes more important than STRCH. This means that advection of potential vorticity is stronger in this area, suggesting that LCEs migrating to the NW region or colliding against the western boundary are responsible for influencing this region. On the other hand, in the SW region the importance of each term remains virtually unchanged in short and long time scales, this fact suggests that circulation in the SW remains persistent through the year.

5.4   Summary and discussion

We performed a vorticity balance to the upper 1000 meters of the ocean in the GoM using our more realistic numerical experiment (OBW-12). The focus was on the western region of the basin and in deep waters (> 1000 m), since the regimes over the shelf and deep waters are different and respond distinct processes. The western region was in turn divided in a north (NW), a central (CW) and a south-western (SW) sub-regions in order to examine if some processes have more influence in some regions than others. Our results show that advection of relative vorticity tends to balance
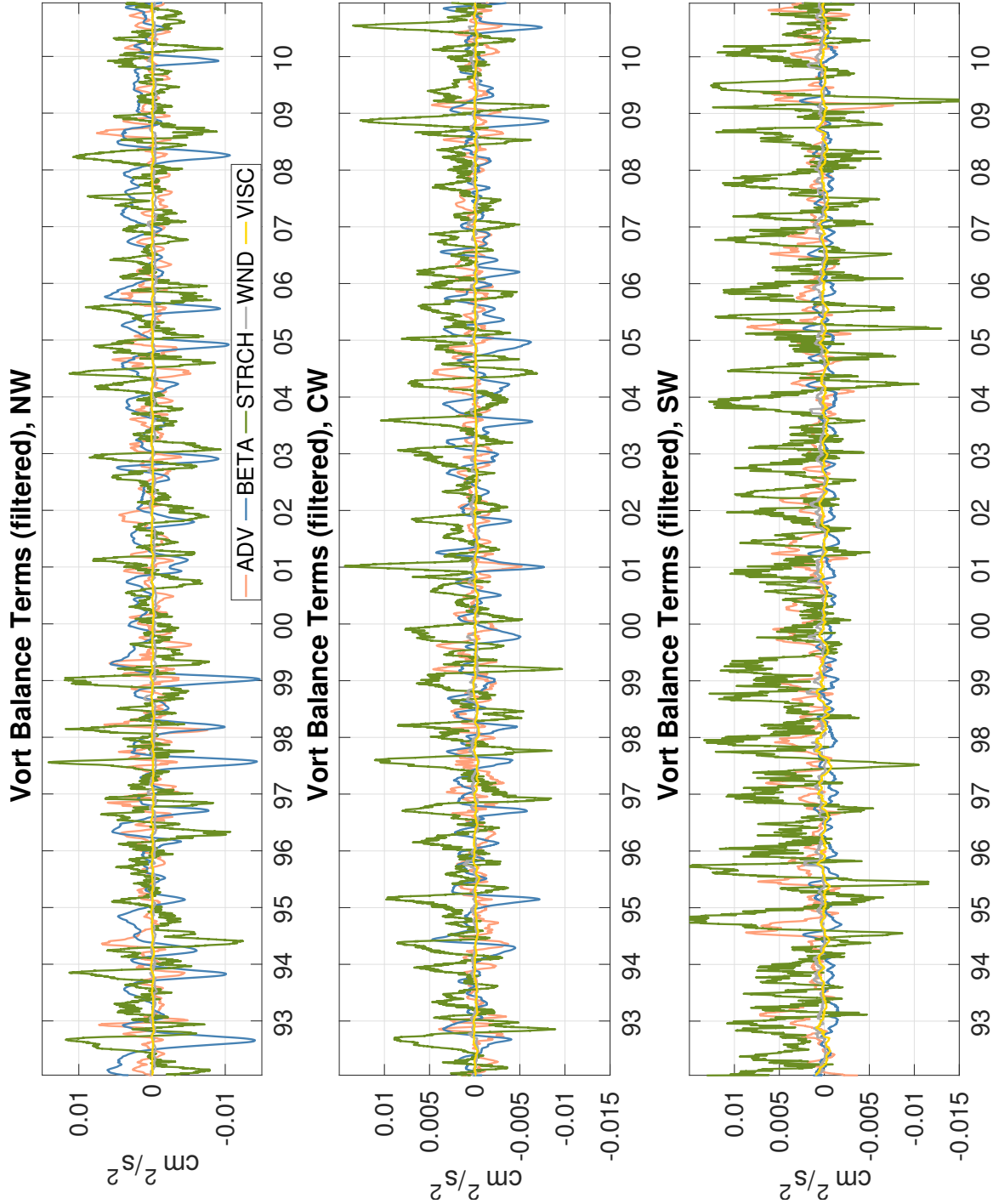
Figure 5.6: 30-day low-pass filtered area-averaged terms for entire simulation, expt OBW-12.
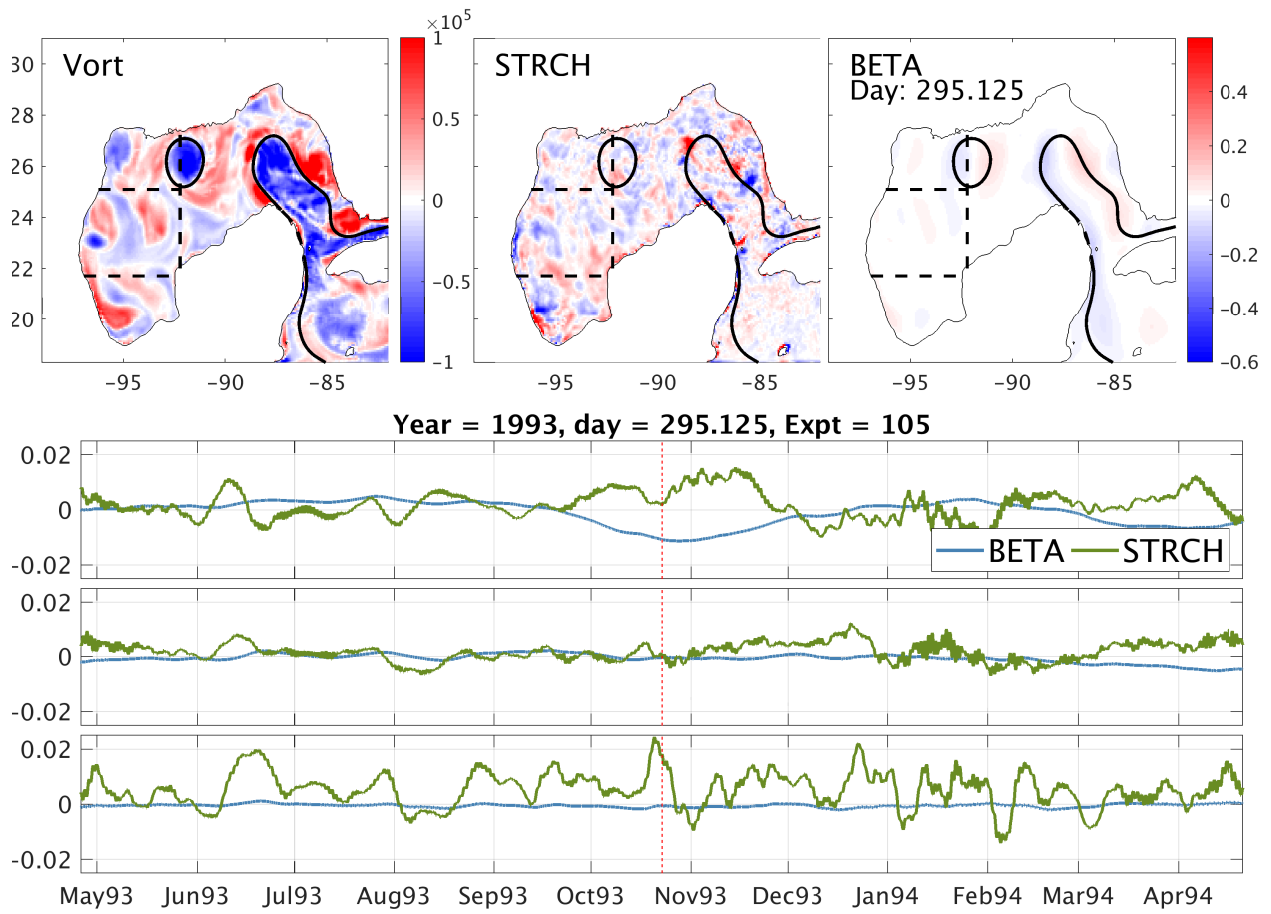
Figure 5.7: Instantaneous fields of vorticity, STRCH and BETA (top three panels) for October 1993; the time series (bottom) are shown for the BETA and STRCH terms, for the NW (top), CW (middle) and SW (bottom panels), and which vertical red line is centered on the day of October.
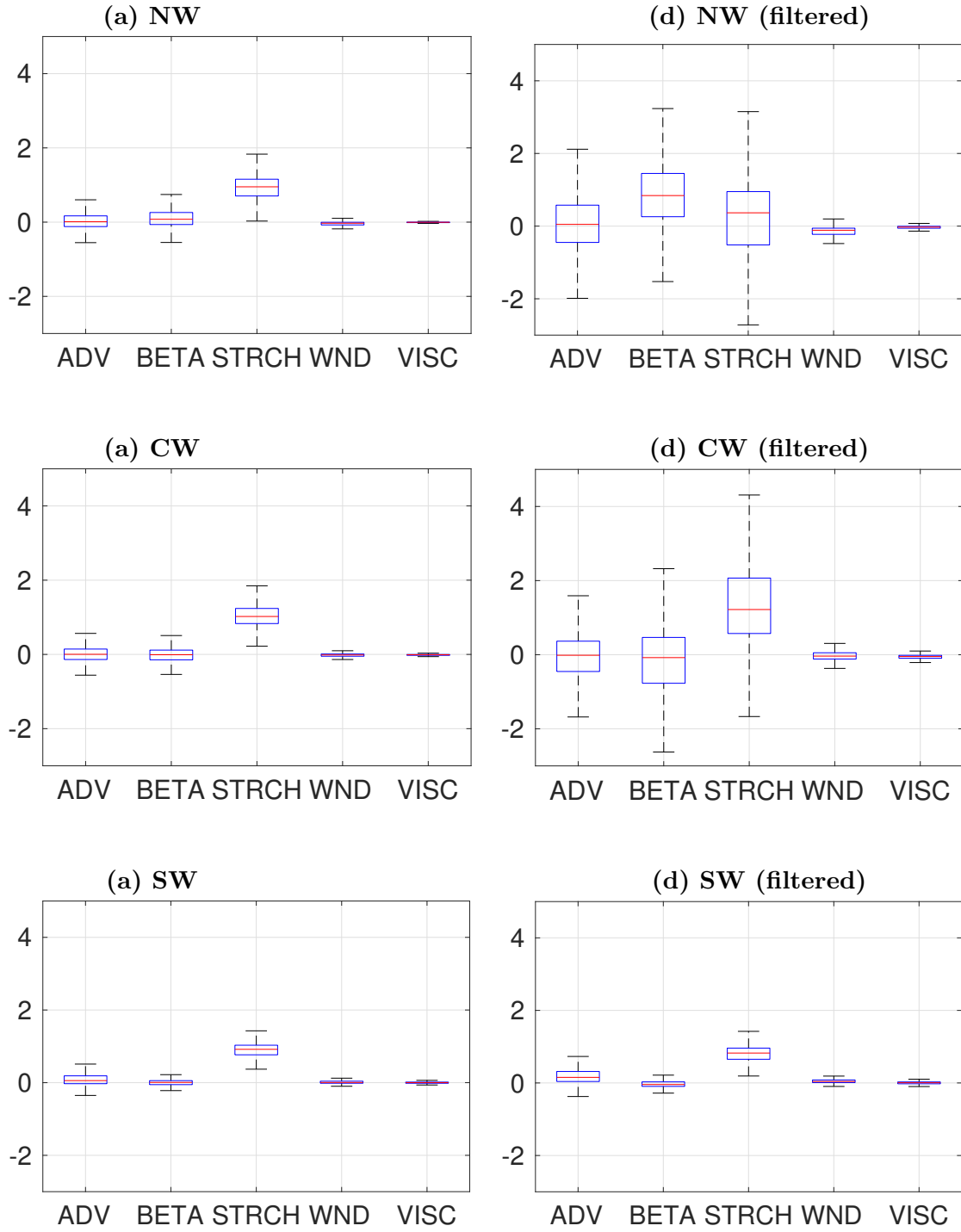
Figure 5.8: Boxplots of the distribution of vorticity balance terms scaled by ς_t. Left panel raw data, right panel 30-day running mean filtered data.

73

advection of planetary vorticity on the mean fields. Meanwhile the rest of the terms are negligible, including wind. On the other hand, the contribution of stretching of the water column to vorticity becomes important to the balance in instantaneous time scales. Also our results show that the central and northwestern regions are more subjected to variability coming from the boundaries, like LCEs, in fact it is shown that BETA and STRCH highly compensate each other when an eddy enters one of these regions, a potential explanation for this is that when the y-component of the velocity becomes stronger, it produces a more negative BETA value, then the water column stretches as a consequence of the convergence in the flow within the LCE. On the other hand, the scale analysis of the vorticity balance terms suggest that the circulation in the southwestern region could be more persistent, since relative contribution of terms do not change at different time scales.

CHAPTER 6

CONCLUSIONS AND FINAL REMARKS

The Gulf of Mexico is one of the most studied regions in the world ocean, even so, there is still a need to better understand the mechanisms that govern the circulation in the region. One example is the less well-known western Gulf, where the circulation over deep waters responds to the large-scale, low-frequency winds and the migration of LCEs in a complex way that, we believe, has been little understood historically. We used a series of multidecadal numerical experiments of increasing complexity configured for the Gulf of Mexico using HYCOM in order to help us better understand the role of the wind, LCEs and another processes in the circulation of the Gulf but in particular the western region. The results show that there is an indirect effect of the wind on the circulation leading to more LCE shedding. Although the scope of the present study is not to understand the physics behind this behaviour, the fact that more LCEs are reaching the western GoM when wind is present means that the region could be leading with more vorticity input through LCEs. Therefore, we can expect that, for instance, the BETA term in the vorticity balance becomes more important more frequently. Another interesting result is that the wind forcing induces a more irregular pathway of the eddies, in fact in the absence of wind, LCEs depict bimodal trajectories with two main locations for detachment from the LC, one north and one south.

The set of idealized wind-driven numerical experiments in the GoM, including a linear configuration of the model, helped us estimate the contribution of different factors to the circulation in the western GOM, through the analysis of time series of the maximum barotropic transport over the western boundary. Firstly, the Sverdrup/linear contribution was found to be responsible of $\sim 40\%$ of the total mean barotropic transport, secondly, non-linearity in the momentum equations could account for another $\sim 40\%$ and the remaining $\sim 20\%$ could be added through variability imposed in the wind forcing.

Through the analysis of the mean barotropic streamfunction over the western boundary current in the Gulf, our results confirm that the western anticyclonic gyre has a seasonal signal consistent with previous studies (Sturges, 1993). On the other hand, in the BOC analysis of the mean

circulation and mean barotropic streamfunction suggests that the cyclonic circulation in the Bay of Campeche has a mean barotropic response to wind, and a partial baroclinic component which could be caused by eddy-topography interactions or topographic confinement via conservation of potential vorticity. Further analysis and numerical studies of the topic are recommended in order to infer the role of the wind on the seasonal variability of the cyclonic circulation in the bay as well as the influence of collapsing LCEs against the western GoM in the BOC gyre.

We used a Circulation Index, which is the depth- and horizontally-averaged relative vorticity for the three sub-regions in the western Gulf, that helped us estimate the average contribution of the wind and LCEs on the circulation of each region. Although the physics of the ocean model is nonlinear, the results show that the effect of these factors is approximately additive as long as the western GoM circulation is thought as an eddy-induced flow superimposed over a wind-driven circulation. We found that, in the NW region the LCEs produce a mean cyclonic flow that strengthen tends to reduce the strong mean anticyclonic flow induced by the wind, therefore producing a relatively weaker anticyclonic circulation, in the CW region mean anticyclonic flow induced by LCEs tend to enhance the comparatively weaker anticyclonic flow induced by wind, and finally in the SW region cyclonic flow induced by LCEs enhance the stronger cyclonic flow generated by the wind, producing the distinctive cyclonic BOC gyre.

The numerical experiment that includes the wind forcing and lateral boundary conditions, namely, OBW-12 is used to analyze the upper (1000 m) ocean vorticity field in order to obtain a description of the contribution of different processes to the circulation in the three western sub-regions described above and at different time scales. The results show that the advection of relative vorticity (ADV) and advection of planetary vorticity (BETA) are the dominant terms transporting or moving around vorticity on average. This can be interpreted as the influence of the mesoscale activity generated by the LCEs and low-frequency wind variability. On shorter time scales, the instantaneous contribution of the stretching of water column term (STRCH) is revealed, we speculate that the high-frequency wind variability is responsible for the inertial currents present in the STRCH field and in the area-averaged time series. We found that there is a primary balance between the low-pass filtered area-averaged time series of BETA and STRCH within the NW and CW regions at irregular intervals. This balance is reached by means of convergence of flow and strengthen of the y-component of the velocity occurring whenever a LCE enters the eastern

boundary of the NW or CW sub-regions, therefore the variability of these terms become a good indicator of LCEs entering the western Gulf. On the other hand, the scaling analysis helped us to confirm the relative importance of the STRCH and BETA terms in short and time scales respectively, as well as the more persistent cyclonic circulation in the BOC compared with the CW and NW regions. Finally, we found that the input of vorticity through wind stress curl (WIND) and viscous stress curl (VISC) are negligible. However, it is important to clarify that this fact does not mean that the contribution of wind to the circulation is null.

Hopefully, the results from this dissertation may lead to future work that will answer some of the remaining open questions, therefore additional steps may be taken to reach the specific goals of 1) breaking up the Bay of Campeche barotropic circulation response into a wind-induced component, which in turn has to be separated into a seasonal and a mean contributions, and a topography-induced component, which is explained by conservation of potential vorticity (Perez-Brunius et al., 2013), and 2) properly deducing the role of the wind in the vorticity balance by estimating its contribution to the rest of the balance terms, this can be achieved by computing the vorticity balance of the numerical experiment without wind forcing and only open lateral boundary conditions (OBNoW-12).

APPENDIX A

DERIVATION OF THE VORTICITY EQUATION

To develop an equation from which the vorticity balance of the model may be analyzed, we first consider the x and y components of the general momentum equation in HYCOM (Wallcraft and Metzger, 2009):

$$\frac{\partial u}{\partial t} + \frac{\partial}{\partial x}\frac{\mathbf{v}^2}{2} - (\zeta + f)v = -\frac{\partial M}{\partial x} + \alpha\frac{\partial \tau_x}{\partial p} + \frac{\partial(\bigtriangledown \cdot (\nu \bigtriangleup p \bigtriangledown \mathbf{v}))}{\partial p} \tag{A.1}$$

$$\frac{\partial v}{\partial t} + \frac{\partial}{\partial y}\frac{\mathbf{v}^2}{2} + (\zeta + f)u = -\frac{\partial M}{\partial y} + \alpha\frac{\partial \tau_y}{\partial p} + \frac{\partial(\bigtriangledown \cdot (\nu \bigtriangleup p \bigtriangledown \mathbf{v}))}{\partial p} \tag{A.2}$$

where:

$\mathbf{v}$	(u, v) horizontal velocity vector
ζ	$(\partial v/\partial x) - (\partial u/\partial y)$ relative vorticity
$\mathbf{k}$	vertical unit vector
M	$z + p\alpha$ Montgomery Potential
τ	wind stress
f	coriolis
ν	horz turbulent viscosity
$\bigtriangleup$ p	layer thickness
α	specific volume

For the purpose of potential vorticity and potential enstrophy conservation, the horizontal advection term in the momentum equation are combined with the Coriolis term as follow:

$$\mathbf{v} \cdot \nabla\mathbf{v} + f\mathbf{k} \times \mathbf{v} = \nabla\frac{\mathbf{v}^2}{2} + (\zeta + f)\mathbf{k} \times \mathbf{v} \tag{A.3}$$

Computing the vertical component of the curl $\dfrac{\partial(A.2)}{\partial x} - \dfrac{\partial(A.1)}{\partial y}$. First $\dfrac{\partial(A.2)}{\partial x}$:

$$\frac{\partial}{\partial t}\frac{\partial v}{\partial x} + \frac{\partial}{\partial x}\frac{\partial}{\partial y}\frac{\mathbf{v}^2}{2} + \frac{\partial}{\partial x}(\zeta + f)u = -\frac{\partial}{\partial x}\frac{\partial M}{\partial y} + \alpha\frac{\partial}{\partial x}\frac{\partial \tau_y}{\partial p} + \frac{\partial}{\partial x}\frac{\partial(\nabla \cdot (\nu \triangle p\nabla\mathbf{v}))}{\partial p} \qquad \text{(A.4)}$$

Expanding terms and rearranging:

$$\frac{\partial}{\partial t}\frac{\partial v}{\partial x} + \frac{\partial}{\partial x}\frac{\partial}{\partial y}\frac{\mathbf{v}^2}{2} + \zeta\frac{\partial u}{\partial x} + u\frac{\partial \zeta}{\partial x} + f\frac{\partial u}{\partial x} = -\frac{\partial}{\partial x}\frac{\partial M}{\partial y} + \alpha\frac{\partial}{\partial x}\frac{\partial \tau_y}{\partial p} + \frac{\partial}{\partial x}\frac{\partial(\nabla \cdot (\nu \triangle p\nabla\mathbf{v}))}{\partial p} \qquad \text{(A.5)}$$

Then, we compute $\dfrac{\partial(A.1)}{\partial y}$:

$$\frac{\partial}{\partial t}\frac{\partial u}{\partial y} + \frac{\partial}{\partial x}\frac{\partial}{\partial y}\frac{\mathbf{v}^2}{2} - \frac{\partial}{\partial y}(\zeta + f)v = -\frac{\partial}{\partial y}\frac{\partial M}{\partial x} + \alpha\frac{\partial}{\partial y}\frac{\partial \tau_x}{\partial p} + \frac{\partial}{\partial y}\frac{\partial(\nabla \cdot (\nu \triangle p\nabla\mathbf{v}))}{\partial p} \qquad \text{(A.6)}$$

Expanding terms and rearranging:

$$\frac{\partial}{\partial t}\frac{\partial u}{\partial y} + \frac{\partial}{\partial x}\frac{\partial}{\partial y}\frac{\mathbf{v}^2}{2} - \zeta\frac{\partial v}{\partial y} - v\frac{\partial \zeta}{\partial y} - f\frac{\partial v}{\partial y} - v\frac{\partial f}{\partial y} = -\frac{\partial}{\partial y}\frac{\partial M}{\partial x} + \alpha\frac{\partial}{\partial y}\frac{\partial \tau_x}{\partial p} + \frac{\partial}{\partial y}\frac{\partial(\nabla \cdot (\nu \triangle p\nabla\mathbf{v}))}{\partial p} \qquad \text{(A.7)}$$

Finally, compute A.5 - A.7 and rearranging terms we lead to the vorticity equation:

$$\frac{\partial \zeta}{\partial t} = -\underbrace{\mathbf{v} \cdot \nabla\zeta}_{\text{Vorticity advection}} - \underbrace{\beta v}_{\text{Plan vort advection}} - \underbrace{(\zeta + f)\nabla \cdot \mathbf{v}}_{\text{Stretching}} +$$

$$\qquad \text{(A.8)}$$

$$\underbrace{\alpha\nabla \times \tau_z}_{\text{Wind stress curl}} + \underbrace{\nabla \times \{(\triangle p)^{-1}\nabla \cdot (\nu \triangle p\nabla\mathbf{v})\}}_{\text{Viscous stress curl}}$$

BIBLIOGRAPHY

Athie, G., Candela, J., Ochoa, J., Sheinbaum, J.,2012. **Impact of Caribbean cyclones on the detachment of Loop Current anticyclones**. J. Geophys. Res., 117, C03018.

Athie, G., J. Sheinbaum, R. Leben, J. Ochoa, M. R. Shannon, and J. Candela, 2015. **Interannual variability in the Yucatan Channel flow**. Geophys. Res. Lett. 42, 1496-1503.

Bleck, R., 2002: **An oceanic general circulation model framed in hybrid isopycnic-cartesian coordinates.** Ocean Modelling, 37, 5588.

Boudra, D.B., and Chassignet, E.P., 1987: **Dynamics of Agulhas retroflection and ring formation in a numerical model. Part 1: The vorticity balance.** J. Phys. Oceanogr. 18, 280-303.

Candela, J., Sheinbaum, J., Ochoa, J.L., Badan, A., and Leben, R., 2002: **The potential vorticity flux through the Yucatan Channel and the Loop Current in the Gulf of Mexico.** Geophys. Res. Lett., 29(22), 2059.

Chang, Y.-L., Oey, L.-Y., 2010. **Why can wind delay the shedding of Loop Current Eddies?**. J. Phys. Oceanogr. 40 (3), 2481-2495.

Chang, Y.-L., Oey, L.-Y., 2012: **Why does the Loop Current tend to shed more eddies in summer and winter?**. Geophys. Res. Lett. 39 (5), L05605.

Chang, Y.-L., Oey, L.-Y., 2013a: **Loop Current growth and eddy shedding using models and observations: numerical process experiments and satellite altimetry data**. J. Phys. Oceanogr. 43 (3), 669-689.

Chang, Y.-L., Oey, L.-Y., 2013b: **Coupled response of the Trade Wind SST gradient, and SST in the Caribbean Sea, and the potential impact on Loop Current's interannual variability**. J. Phys. Oceanogr. 43 (7), 1325-1344.

Chassignet, E.P., Smith, L.T., Halliwell, G.R., Bleck, R., 2003: **North Atlantic simulations with the Hybrid Coordinate Ocean Model (HYCOM): impact of the vertical coordinate choice, reference pressure and thermobaricity.**. J. Phys. Oceanogr. 33 (7), 2504-2526.

Chassignet, E.P., Hurlburt, H.E., Smedstad, O.M., Barron, C.N., Ko, D.S., Rhodes, R.C., Shriver, J.F., Wallcraft, A., Arnone, R.A., 2005: **Assesment of Data Assimilative Ocean Models in the Gulf of Mexico using Ocean Color.**. Circulation in the Gulf of Mexico: Observations and Models, Amer. Geophys. Union, No. 161 in Geophys. Monogr., 87-100.

Chassignet, E.P., Hurlburt, H.E., Smedstad, C.N., Halliwell, G.R., Metzger, E.J., Blanton, B.O., Wallcraft, A., Lozano, C., Rao, D.b., Hogan, P.J., Srinivasan, A., 2006: **Generalized Vertical Coordinates for Eddy-Resolving Global and Coastal Ocean Forecasts.** Oceanography, 19(1), 20-31.

Chassignet, E.P., Hurlburt, H.E., Smedstad, C.N., Hogan, P.J., Halliwell, G.R., Wallcraft, A., R. Baraille, and R. Bleck, 2007: **The HYCOM (HYbrid Coordinate Ocean Model) data assimilative system.** J. Mar. Systems., 65, 6083.

Cushman-Roisin, B., Chassignet, E. P., Tang, B., 1990: **Westward Motion of Mesoscale Eddies.** J. Phys. Oceanogr., 20, 758-768.

Chassignet, E.P., 2011: **Isopycnic and hybrid ocean modeling in the context of GODAE.** Operational Oceanography in the 21st Century, A. Schiller and G. Brassington, Eds., Springer, 263-294.

DeHaan, C. J., Sturges, W., 2005. **Deep Cyclonic Circulation in the Gulf of Mexico**. J. Phys. Oceanogr. 35, 1801-1812.

DiMarco, S.F., Nowlin Jr., W.D., Reid, R.O., 2005. **A statistical description of the velocity fields from upper ocean drifters in the Gulf of Mexico.** In: Sturges, W., Lugo-Fernandez, A. (Eds.), circulation in the Gulf of Mexico: observations and Models. AGU, Washington, DC, pp. 101110.

Donohue, K., Hamilton, P., Leben, R., Watts, R., Waddell, E., 2008. **Survey of Deepwater Currents in the Northwestern Gulf of Mexico, vol. II: Technical Report.** OCS Study MMS 2008-031. U.S. Department of the Interior, Minerals Management Service, Gulf of Mexico OCS Region, New Orleans, 364 pp.

Dukhovskoy, D.S., Leben, R.R., Chassignet, E.P., Hall, C.A., Morey, S.L., Nedbor-Gross, R., 2015: **Characterization of the uncertainty of loop current metrics using a multidecadal numerical simulation and altimeter observations**. Deep-Sea Research I 100 (2015) 140-158.

Elliot, B.A., 1982: **Anticyclonic rings in the Gulf of Mexico**. J. Phys. Oceanogr. 12 (7), 1292-1309.

Frolov, S.A., Sutyrin, G.G., Rowe, G.D., Rothstein, L.M., 2004: **Loop Current eddy interaction with the western boundary in the Gulf of Mexico**. J. Phys. Oceanogr. 34 (7), 2223-2237.

Garcia-Jove, M., Sheinbaum, J., Jouanno J., 2016: **Sensitivity of Loop Current metrics and eddy detachments to different model configurations: The impact of topography and Caribbean perturbations**. Atmosfera, 29(3), 235-265.

Hamilton, P. and Lugo-Fernandez, A., 2001. **Observations of high speed deep currents in the northern Gulf of Mexico.** Geophys. Res. Lett. 28:2867-2870.

Hamilton, P., K. Donohue, C. Hall, R.R. Leben, H. Quian, J. Sheinbaum, and D.R. Watts, 2014. **Observations and dynamics of the Loop Current.** US Dept. of the interior, Bureau of Ocean Energy Management, Gulf of Mexico OCS Region, New Orleans, LA. OCS Study BOEM 2015-006. 417 pp.

Hall, C.A., and Leben, R.R., 2016: **Observational evidence of seasonality in the timing of loop current eddy separation**. Dyn. Atm. Ocean 76, 240-267.

Hurlburt, H.E., and Thompson, J.D., 1980: **A numerical study of Loop Current Intrusions and Eddy Shedding**. J. Phys. Oceanogr. 10 (7), 1611-1651.

Jaimes B., 2005: **Energetics of the wind and Loop Current-driven circulation in the Gulf of Mexico**. Master Thesis.

Lee, H.C., and Mellor, G.L., 2003: **Numerical simulation of the gulf stream system: the loop current and the deep circulation**. J. Geophys. Res., 108 (C10), 2501-2216.

Leben, R.R., 2005. **Altimeter-derived Loop Current metrics.** Circulation in the Gulf of Mexico: Observations and Models. Amer. Geophys. Union, No. 161 in Geophys. Monogr., 181-201.

Maul, G. A. y A. Herman, 1985: **Mean dynamic topography of the Gulf of Mexico with application to satellite altimetry**. Marine Geodesy., 9, 27-44.

Merrell, W.J., and Morrison, J.M., 1981: **On the circulation of the Western Gulf of Mexico with observations from April 1978**. J. Geophys. Res., 86 (C10), 4181-4185.

Morey, S., J. Zavala-Hidalgo, and O'Brien, J., 2005: **The seasonal variability of continental shelf circulation in the northern and western Gulf of Mexico from a high-resolution numerical model**. Circulation in the Gulf of Mexico: Observations and Models, Amer. Geophys. Union, No. 161 in Geophys. Monogr., 203-218.

Morey, S., and Dukhovskoy, D.S., 2012: **Analysis methods for characterizing salinity variability from multivariate time series applied to the Apalachicola Bay estuary.** J. Atmospheric Ocean. Technol. 29 (7), 613-628.

Morey, S., and Dukhovskoy, D.S., 2013: **A downscaling method for simulating deep current interactions with topography Application to the Sigsbee Escarpment.** Ocean Modelling, 69, 50-63.

Murray, C.P., Morey, S., and O'Brien, J., 2001: **Interannual variability of upper ocean vorticity balances in the Gulf of Alaska**. J. Geophys. Res., 106 (C3), 4479-4491.

Nedbor-Gross, R., Dukhovskoy, D., Bourassa, M.A., Morey, S.L., and Chassignet, E. P., 2014: **Investigation of the relationship between the Yucatan Channel transport and the Loop Current area in a multidecadal numerical simulation.** MTSJ. 48(4), 15-26.

Nof, D., 1981 **On the beta-induced movement of isolated baroclinic eddies.** J. Phys. Oceanogr. 11(12):1662-1672

Oey, L.Y. and Lee, H.C. 2003: **Effect of winds and Caribbean eddies on the frequency of Loop Current eddy shedding: A numerical model study**. J. Geophys. Res., 108 (C10), 2201-2225.

Oey and Lee., Ezer, T., Lee, H.C., 2005: **Loop Current, Rings and related circulation in the Gulf of Mexico: a review of numerical models and future challenges**. Circulation in the Gulf of Mexico: Observations and Models, Amer. Geophys. Union, No. 161 in Geophys. Monogr., 31-56.

Perez-Brunius, P., P. Garcia Carrillo, J. Dubranna, J. Sheinbaum, and J. Candela, 2013: **Direct observations of the upper layer circulation in the southern Gulf of Mexico**. Deep-Sea Res. II, 85, 182-194.

Perez-Brunius, P., Furey, H., Bower, A., Hamilton, P., J. Candela, P. Garcia Carrillo, Leben, R., 2018: **Dominant circulation patterns of the deep Gulf of Mexico**. J. Phys. Oceanogr., 48, 511-529.

Romanou, A., Chassignet, E.P., Sturges, W., 2004: **Gulf of Mexico Circulation within a high-resolution numerical simulation of the North Atlantic Ocean**. J. Geophys. Res., 109, C01003, doi:10.1029/2003JC001770.

Sheinbaum, J., Candela, J., Badan, A., Ochoa, J., 2002: **Flow structure and transports in the Yucatan Channel.**. Geophys. Res. Lett. 29 (3), 1040.

Schmitz, Jr. W. J., McCartney, M.S., 1993: **On the North Atlantic circulation**. Reviews of Geophysics, 31, 1, 29-49.

Schmitz Jr. W. J., Biggs, D.C., Lugo-Fernandez, A., Oey, L.Y., Sturges, W., 2005: **A synopsis of the circulation in the Gulf of Mexico and on its continental margins**. Circulation in the Gulf of Mexico: Observations and Models, Amer. Geophys. Union, No. 161 in Geophys. Monogr., 11-30.

Schoonover, J., Dewar, W., Wienders, N., Gula, J., McWilliams, C., Molemaker, M.J., Bates, S.C., Danabasoglu, G., and Yeager, S., 2016: **North Atlantic barotropic vorticity balances in numerical models.** J. Phys. Oceanogr., 46, 289303.

Smith, D.C. and O'Brien, J.J., 1983: **The interaction of a two-layer isolated mesoscale eddy with bottom topography**. J. Phys. Oceanogr. 13, 1681-1697.

Souza, J. M. A. C., Powell, B., Castillo-Trujillo, A. C., and Flament,P., 2015: **The Vorticity Balance of the Ocean Surface in Hawaii from a Regional Reanalysis**. J. Phys. Oceanogr. 45, 424440

Sturges, W., and J.P. Blaha, 1976: **A western boundary current in the Gulf of Mexico**. Science, 192, 367-369, 1976.

Sturges, W., and Evans, J.C., 1983: **On the variability of the Loop Current in the Gulf of Mexico**. J. Geophys. Res., 98 (C10), 18053-18068.

Sturges, W., 1993: **The annual cycle of the WBC in the Gulf of Mexico**. J. Marine Res., 41, 639-653.

Sturges W., and Leben, R., 2000: **Frequency of ring separations from the loop current in the Gulf of Mexico: a revised estimate**. J. Phys. Oceanogr. 30 (7), 1814-1819.

Sturges W., and Kenyon, 2008: **Mean flow in the Gulf of Mexico**. J. Phys. Oceanogr. 38 (7), 1501-1514.

Vazquez de la Cerda, Reid, R.O., DiMarco,S.F., Jochens, A.E., 2005: **Bay of Campeche circulation: an update**. Circulation in the Gulf of Mexico: Observations and Models, Amer. Geophys. Union, No. 161 in Geophys. Monogr., 279-294.

Vidal, V. M. V., F. V. Vidal, A. F. Hernndez, A. Meza y J. M. Prez-Molero, 1994: **Baroclinic flows, transports, and kinematic properties in a cyclonic-anticyclonic-cyclonic ring triad in the Gulf of Mexico** J. Geophys. Res., 99, C4, 7571-7597.

Vidal, V.M.V, Vidal, F.V., Mesa, E., Portilla, J, Zambrano, L., Jaimes, B., 1999: **Ring-slope interactions and the formation of the western boundary current in the Gulf of Mexico.**. J. Geophys. Res., 104 (C9), 20523-20550.

Vukovich, F.M., 1995. **An updated evaluation of the Loop Currents eddy shedding frequency.** J. Geophys. Res. 100 (C5), 86558659.

Vukovich, F.M., 2007: **Climatology of ocean features in the Gulf of Mexico using satellite remote sensing data**. J. Phys. Oceanogr., 37 (7), 689-707.

Vukovich, F.M., 2012: **Changes in the loop current's eddy shedding in the period 2001-2010**. International Journal of Ocenaography, (2012).

Zamudio, L., Hogan, P.J., 2008. **Nesting the Gulf of Mexico in Atlantic HYCOM: oceanographic processes generated by Hurricane Ivan.** Ocean. Model. 21, 106125.

Zavala-Hidalgo, J., 1997: **Numerical study of the seasonal dynamics and thermodynamics in the Gulf of Mexico.** PhD Thesis.

Zavala-Hidalgo, J.,Morey, S. L., and OBrien, J. J., 2003: **Cyclonic eddies northeast of the Campeche Bank from altimetry data**. J. Phys. Oceanogr., 33, 623-629.

Zavala-Hidalgo, J., Morey, S. L., O'Brien, J. J., and Zamudio, L., 2006: **On the Loop Current eddy shedding variability**. Atmósfera, 19(1), 41-48.

Zavala-Hidalgo, J., Romero-Centeno, R., Mateos-Jasso, A., Morey, S. L., O'Brien, J. J., and Martinez-Lopez, B., 2014: **The response of the Gulf of Mexico to wind and heat flux forcing: What has been learned in recent years?**. Atmósfera, 27(3), 317-334.

BIOGRAPHICAL SKETCH

Erick was born in Mexico City where he became interested in earth sciences at a young age. He eventually completed his Bachelors degree in hydrological engineering at the Metropolitan Autonomous University in 2010. Then, he obtained a Master's degree in Earth Sciences focusing in estuarine processes at the National Autonomous University of Mexico in 2014. Then he enrolled in the doctoral program in Physical Oceanography at FSU in Fall 2014. Erick's research interests include coastal ocean processes, numerical modeling and ocean general circulation.